Centre of Excellence for Sustainable Mining and Exploration (CESME)

Annual Report to the Office of Research Services

August 2024

Executive Summary

In the past year CESME has achieved the following:

- Co-hosted a successful in-person event associated with the PDAC meeting
- Co-hosted a successful International Conference
- Supported the creation of a NOHFC Industrial Research Chair partnering with Kinross Gold
- Supported an application to the Ontario Centre of Innovation to promote Critical Minerals Outreach in Northern Ontario
- Provided scholarships to support graduate research
- Sponsored in-person workshops
- Facilitated new research initiatives between local industry and LU researchers

CESME goals & objectives

As outlined in the original proposal to the Senate Research Committee the purpose, rationale, mission and goals of the Centre of Excellence in Sustainable Mining and Exploration (CESME) are as follows:

Purpose

CESME will encourage and support research, education and outreach activities regarding the nature and impacts of mineral resource exploration and extraction particularly in Northern Ontario.

Rationale

Northern Ontario's dynamic mining sector is booming, creating challenges regarding how best to undertake sustainable economic development while ensuring environmental protection and respecting constitutionally protected Aboriginal and Treaty rights. CESME will help address these challenges by linking Lakehead University researchers with partners from First Nation, Métis and local communities, government, and industry. This collaborative approach recognizes that Canadian natural resource development requires sophisticated planning, collaboration, assessment, implementation, and remediation strategies that are calculated to minimize negative environmental, socio-economic, and cultural impacts. CESME uses the term "sustainable" to imply reconciliation of the three pillars of environmental, social equity, and economic demands (2005 World Summit on Social Development) that is now widely recognized by the mining industry. To this end, CESME is structured under three pillars: 1) Mining, Exploration and Mineral Processing; 2) Environmental Impacts; and 3) First Nation, Métis and Local Community Engagement.

Through the Centre academic, community, government, and industry partners will carry out cutting-edge research in discovery, advanced exploration, and development, and address the environmental, social and cultural aspects of mineral extraction.

Mission

CESME will:

- Support the development of community-based research and outreach activities in both the Lakehead University community and the region as a whole;
- Generate research projects that facilitate sustainable resource development in Northern Ontario and evaluate the current and future ecological, social, cultural and economic impacts of development; and
- Apply research outcomes from Northern Ontario projects to broader sustainable development issues in other northern Canadian and international jurisdictions and apply the lessons learned in other jurisdictions to Northern Ontario.

Goals

CESME will:

- Increase the capacity for mineral deposit research at Lakehead University and enhance the reputation of the institution in the region, nationally and internationally;
- Increase the capacity for research into the environmental impacts of mining and the sustainability of this activity in Northern Ontario;
- Increase the capacity for research into the social and cultural impacts of mining, especially the involvement of local and First Nation and Métis communities and the recognition of Aboriginal and treaty rights;
- Increase the capacity for research into mining and mineral processing;
- Initiate interdisciplinary research into these fields and develop multidisciplinary research proposals for funding agencies and research partners;
- Bring together a diverse range of researchers at Lakehead University working in fields related to mining exploration, sustainable mining, and environmental and community impacts; and
- Make Lakehead University the hub for sustainable resource extraction research in Northern Ontario.

Progress towards the Centre's goals

In our original proposal to the Senate Research Committee we indicated that we would achieve the goals of the Centre by undertaking a number of activities. This section lists those activities and highlights progress made.

1. *Initiate discussions with the wider community to shape the research activities of the Centre.*

   We have continued discussions with a diverse group of research partners including First Nations educational organisations. We continue to work with Mining Matters to facilitate their engagement with schools and communities in Northern Ontario, including engaging them to partner in our successful application to the Onatrio Centre of Innovation.

2. *Generate multidisciplinary research proposals and apply for external funding*

   CESME worked with Indigenous Initiative and Dr Michel Beaulieu to successfully apply for the Onatrio Centre for Innovation for $100,000 to promote Critical Minerals Outreach in Northern Ontario - A Pilot Program, Regional Future Workforce Program. In addition, CESME initiated the conversation and worked with Kinross Gold to establish an NOHFC Industrial Research Chair in Mineral Exploration. This has secured $500,000 in funding from Kinross and resulted in applications to NSERC, FedNor and NOHFC to fully support the Chair.

3. *Invite and fund proposals for research and outreach activities*

   We continue to solicit proposals from the University community

4. *Recruit and foster faculty, postdoctoral fellows, postgraduate, graduate, and undergraduate student participation*

   CESME is supporting the MSc research of Luis Zappa and Adrian Perez, both MSc students in the Department of Geology through the Dr. Melville Bartley Memorial CESME award. Luis is working to better understand the paragenesis of the Saddle North porphyry deposit in BC and Adrian is investigating the formation of the hots rocks to the Moss Lake gold deposit.

5. *Establish working relationships with similar national and international centres (e.g., Mineral Deposit Research Unit (MDRU) at the University of British Columbia, Mineral Exploration Research Centre (MERC) at Laurentian, CODES – ARC Centre of Excellence in Ore Deposits at the University of Tasmania, Centre for Exploration Targeting (CET) at the University of Western Australia)*

   We have a very successful collaboration with CODES and continue our partnership with the Mineral Deposit Research Unit at UBC through an ongoing NSERC Alliance grant

6. *Develop and maintain a website for the Centre*

   We have established a website that highlights CESME activities and acts as a repository for our publications and videos of our guest speakers.

Members of CESME

The Advisory Board for CESME continues to operate efficiently having met a number of times by teleconference in the past year. Unfortunately, one of the founding Board Members, Dr. Jim Franklin, passed away this year and we are currently seeking a replacement. The membership comprises:

- Ms. Sue Craig, Consultant - Chair
- Mr. John Mason, CEDC
- Mr. Glenn Nolan, Noront
- Dr. Scott Jobin-Bevans, Consultant
- Mr. Gord Maxwell, Consultant

The following faculty members have agreed to lead the three research pillars of CESME:

- Dr. Pedram Fatehi continues as the leader of the Mining, Exploration and Mineral Processing pillar

- Dr. Michael Rennie, continues as the leader of the Environmental pillar
- We are currently seeking a leader for the Indigenous pillar.

The following faculty members have signed up as CESME members:

Dr.	Matthew	Boyd	Anthropology
Dr.	Andrew	Conly	Geology
Dr.	Jian	Deng	Civil Engineering
Dr.	Amanda	Diochon	Geology
Dr.	Martha	Dowsley	Anthropology
Dr.	A. Ernest	Epp	History
Dr.	Pedram	Fatehi	Chemical Engineering
Dr.	Philip	Fralick	Geology (emeritus)
Dr.	Scott	Hamilton	Anthropology
Dr.	Rachel	Jekanowski	English, Memorial University
Dr.	Peter	Lee	Biology (emeritus)
Dr.	Kam	Leung	Biology
Dr.	Zhiquan	Li	Geology
Dr.	Baoqiang	Liao	Chemical Engineering
Dr.	Nancy	Luckai	Natural Resources Management (emeritus)
Dr	Rob	Petrunia	Economics
Dr.	Mike	Rennie	Biology
Dr.	Karl	Skogstad	Economics
Dr.	Robert	Stewart	Geography
Dr.	Shannon	Zurevinski	Geology

The following adjunct faculty are also members of CESME:

Dr.	Greg	Ross	NOSM
Dr.	Robert	Mackereth	Centre for Northern Forest Ecosystem Research

In addition, three Postdoctoral Fellows (Moses Angombe, James Tolley and Tobias Stephan) are affiliated with CESME.

Research Projects & Scholarly Activities

Other activities

CESME is continuing to engage with local mining companies by hosting “Discovery Days” when researchers at Lakehead present their work to company representatives in order to develop new partnerships. This year we ran a day for Kinross which ultimately led to the establishment of an NOHFC Industrial Research Chair.

CESME participated in the Cen Can Expo in Thunder Bay where we co-hosted a booth with the Economic Development team.

Educational Activities

CESME hosted the 15th International Ni-Cu Symposium at Lakehead University from August 5-9. The conference brought together 140 participants from industry, academia and government for three days of technical sessions a series of well-attended pre- and post-meeting field trips. Thanks to the generous support of our sponsors we were able to significantly subsidise the cost for students to attend the meeting. The meeting was a financial success and allowed us to set up a scholarship to support graduate students at Lakehead Univiversity.

CESME sponsored three short courses organized by the Lakehead University SEG student chapter. The first short course was on “Ancient and modern volcani-hosted massive sulphide deposits” by Dr. Bruce Gemmel. The workshop took place on September 30th, 2023 with ~35 attendees. The second course on “Structural geology and it's application in mining and mineral exploration” was taught on August 30, 2024 with around 25 participants.

Undergraduate and graduate training

We have supported two graduate students through the Dr. Melville Bartley Memorial CESME Award as discussed above.

Dr. Matthew Brzozowski completed his Postdoctoral Fellowship with CESME in mide 2023 but continues to publish the research that resulted from that. This includes two papers “Brzozowski, M., Hollings, P., Hamilton, M., Heggie, G., Caglioti, C., Yahia, K., and Bravo, A., 2024. Petrogenetic relationship of the variably Ni–Cu–platinum-group element (PGE)-mineralized intrusions of the Thunder Bay North Intrusive Complex, Midcontinent Rift, Canada: Implications for mineral exploration in mafic–ultramafic complexes. GSA Bulletin, https://doi.org/10.1130/B37736.1” and Brzozowski, M., Hollings, P., Heggie, G., MacTavish, A., Wilton, D., Evans-Lamswood, D., 2023. Characterizing the supra- and subsolidus processes that generated the Current PGE–Cu–Ni deposit, Thunder Bay North Intrusive Complex, Canada: insights from trace elements and multiple S isotopes of sulfides. Mineralium Deposita, https://doi.org/10.1007/s00126-023-01193-9.”

The three current Post Doctoral Fellows associated with CESME are Drs. **Moses Angombe, James Tolley and Tobias Stephan**. All three are actively engaged in research and the mentoring of MSc students.

Financial statement

The main CESME account has been relying on residual funds left from running our conference and occasional donations. These funds have been expended meaning that the only funds available to directly support CESME activities come from the Research Support Fund. While this support is appreciated there are limits to how those funds can be used which may impact future activities.

The statement provided below covers the 2023-2024 financial year.

Item	Credit	Debit
Carry Forward	$00.00	
Transfer from Research Support Fund	$18,0000	
Donations		
Travel & Conferences (*this includes cost for Hollings to attend Roundup in Jan 24, and Hollings and Phillips to attend PDAC in March 24*)		$ 10,513.29
Sponsorship (*SEG Workshop & C2U Expo*)		$1600.00
Printing		$54.50
Catering for Kinross Research Day		$148.74
Booth at Cen Can expo		$1266.77
PDAC booth		$3231.26
Promotional materials		$680.44
Returned to Research Support Fund		$287.68
Subtotal	$18,000.00	$18,000.00
Balance	**$0.00**	

One-year and five-year plans

The immediate goals of CESME are as follows:

- Work with the Advisory Board to implement the new Strategic Plan for CESME and the Action Items within it
- Replace Dr. Franklin on the Board and recruit new members
- We continue to seek funding both from research councils and donors to support graduate and undergraduate research.
- We are still considering the possibility of hosting another conference at Lakehead or alternatively providing support to other related events on campus.
- We continue to engage with faculty across campus to encourage them to participate in and identify CESME activities.

Having met one of our medium-term goals of establishing a research Chair under the Mining and Exploration Pillar we are still seeking to establish two research chairs, one related to each of the remaining CESME pillars (Environmental Impacts and First Nation, Métis and Local Community Engagement). These chairs are critical to the long-term success of CESME as they will provide the core researchers around which Centre activities can be developed. In addition to funding the Chair we are seeking ways to support graduate students and Post-Graduate Fellows who will undertake much of the research. We are investigating a number of mechanisms to fund these chairs, including:

- Corporate donations;
- Philanthropy

We are working closely with the Office of Research Services and External Relations to achieve this goal.

2024-2025 Budget*

Item	Cost
Attend PDAC meeting to promote CESME (booth costs and travel)	$7,500
Attend Roundup meeting to promote CESME (2 x$2,000 people)	$4,000
Conferences for CESME members	$4,000
Promotional materials	$1,000
Invited speakers	$3,500

* Scholarships provided by CESME are not included here.

Emerging Trends

CESME activities are more important than ever in the face of changing developments and conditions in the mining sector in northern Ontario. The mining industry is very active in Northern Ontario which has led to high employment rates and a number of funding opportunities for research, however, it has also highlighted the need for a greater number of graduates from the geoscience programs at Lakehead. Enrolments are down across Canada and we are working to expose school age students to geology and mining through collaborations with organisations like Mining Matters and working directly with local schoolboards and the Faculty of Education. The need for increased training to meet the growing economic development needs in Northern Ontario means that this will continue to be a priority for the Centre.

Appendix 1

Media reports, posters and publications

CENTRE OF EXCELLENCE FOR
SUSTAINABLE MINING
& EXPLORATION

J. Bruce Gemmell (PhD)

Presented by the Lakehead University Society of Economical Geology student chapter

short course:

Ancient and Modern Volcanic-hosted Massive Sulfide Deposits

Saturday September 30 2023 | Venue T.B.A | Thunder Bay

This short course will include an overview of the geology, genesis, and exploration for volcanic-hosted massive sulfide (VHMS) deposits. Both ancient and modern examples will be examined. Topics include general features, classification schemes, tectonic setting, mineralogy and textures, metal zoning, and ore equivalent horizons. The characteristics and diagnostic features of seafloor and sub-seafloor genetic models will be discussed. The mineralogy, assemblages, zoning, and geochemistry of hydrothermal alteration will be emphasized, as well as exploration techniques/ strategies for VHMS deposits. The short course will end with examining modern, seafloor, mineralizing hydrothermal systems and comparing these to ancient VHMS deposits.

Bruce Gemmell obtained his B.Sc. in 1979 from UBC, Canada and his M.A. (1982) and Ph.D. (1987) from Dartmouth College, USA. Bruce worked at the Centre of Excellence in Ore Deposits and Exploration Science (CODES) at the University of Tasmania, Australia for 30 years, where he served as Head of the School of Earth Sciences and Director of CODES.

At CODES, Bruce researched a wide range of ore deposit types, including VHMS deposits, LS-IS-HS epithermal deposits, structurally controlled copper deposits, and modern seafloor hydrothermal systems. He specializes in mineralogy and geochemistry of hydrothermal alteration and its application to exploration. He and collaborators also developed process-based exploration models focusing on mineral chemistry zoning in porphyry-epithermal deposit environments.

Bruce has published over 100 papers in international peer-reviewed journals, was a past President of the Society of Economic Geologists (SEG - 2018) and is currently the technical editor for the SEG's newsletter, SEG Discovery.

Since leaving CODES in 2017, Bruce has become a consultant to the minerals industry, where he has undertaken consulting in Australia, Canada, USA, Mexico, Turkey, Argentina, Peru, Sweden, Fiji, Indonesia, Kazakhstan and Mongolia.

short course registration

September 30, 2023 9:00 AM - Thunder Bay - Venue T.B.A

Professional Rate - $250

Student Rate $50

Please complete the registration form below and return it with a cheque (payable to Lakehead University SEG student Chapter) or cash to:

Lakehead University SEG Student chapter

c/o Department of Geology

Lakehead University

CB4064 955 Oliver Rd

Thunder Bay, ON. Canada P7B 5E1

Please send an email to Jordon Peterzon (jpeterzo@lakeheadu.ca) to express interest in attending the course.

Registration Form

Name ____

Affilation/Address________________________________

Phone:____

Email____

Lakehead University Student Chapter SEG and Brett Davis (PhD) short course: Structural geology and it's application in mining and mineral exploration

Friday August 30th @ Lakehead University

Brett Davis - PhD

Brett is widely regarded in the international exploration and mining industry for his application of applied structural geology to numerous commodity types and mineral deposit styles. The approach Brett has brought to understanding mineralising environments globally is a product of the integration of modern structural geology and techniques married with several decades of applied research. Brett has held various technical and senior managerial roles at consultancy groups and in mining and exploration companies prior to running his own international geology consultancy, Olinda Gold Pty Ltd. In addition to consultancy assignments, Brett runs a modular structural geology training course that can be tailored to individual sites/companies or presented in a multi-client environment. Brett currently holds an Adjunct Senior Research Fellow position at James Cook University. He is a Member of the Australian Institute of Geoscientists and a Fellow of the Society of Economic Geologists. He is also the geological content editor for Coring Magazine, the world's largest drilling magazine.

Fill out the google form to register, or email seg.geology@lakeheadu.ca
https://forms.gle/EaqvcEFgvAtAmBFS9

Professional fee: $250
Student Fee: $50
Lunch and refreshments provided!

Centre of Excellence for Sustainable Mining & Exploration

Lakehead UNIVERSITY

Questions?
Email: seg.geology@lakeheadu.ca

SEG LAKEHEAD UNIVERSITY STUDENT CHAPTER

15th International Ni-Cu Symposium
Thunder Bay 2024

SAVE THE DATE!

The **15TH International Ni-Cu Symposium** will be held August 05-09, 2024 at Lakehead University in Thunder Bay, Ontario, Canada.

We look forward to seeing you here!

Potential field trips:

- Lac des Iles Mine
- Marathon deposit
- Current Lake and Escape Lake deposits
- Eagle Mine
- Tamarack deposit
- Midcontinent Rift System near Lake Superior in Canada and USA
- Archean greenstone belts with Ni-Cu-PGE mineralization

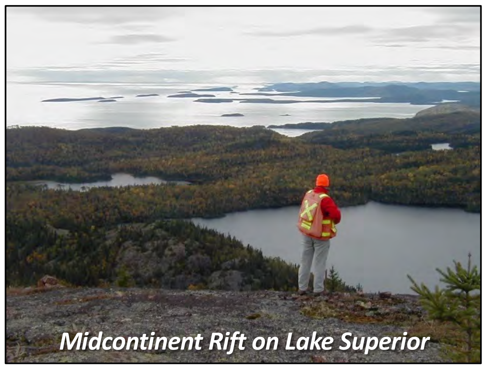

Midcontinent Rift on Lake Superior

For more information:

Contact: Dr. Peter Hollings, Chair, 15TH INCS

Email: incstbay2024@lakeheadu.ca

Visit: https://ec.lakeheadu.ca/ni-cu/welcome

Lac des Iles Mine, (Impala Canada)

MAGSUL

Lakehead University

15th International Ni-Cu Symposium
Thunder Bay 2024

SAVE THE DATE!

The 15TH International Ni-Cu Symposium will be held August 05-09, 2024 at Lakehead University in Thunder Bay, Ontario, Canada.

We look forward to seeing you here!

Potential field trips:

- Lac des Iles Mine
- Marathon deposit
- Current Lake and Escape Lake deposits
- Eagle Mine
- Tamarack deposit
- Midcontinent Rift System near Lake Superior in Canada and USA
- Archean greenstone belts with Ni-Cu-PGE mineralization

Midcontinent Rift on Lake Superior

For more information:

Contact: Dr. Peter Hollings, Chair, 15TH INCS

Email: incstbay2024@lakeheadu.ca

Visit: https://ec.lakeheadu.ca/ni-cu/welcome

Lac des Iles Mine, (Impala Canada)

MAGSUL

Lakehead University

Mineralium Deposita
https://doi.org/10.1007/s00126-023-01193-9

ARTICLE

Characterizing the supra- and subsolidus processes that generated the Current PGE–Cu–Ni deposit, Thunder Bay North Intrusive Complex, Canada: insights from trace elements and multiple S isotopes of sulfides

M. Brzozowski[1,2] · P. Hollings[2] · G. Heggie[3] · A. MacTavish[4] · D. Wilton[5] · D. Evans-Lamswood[6]

Received: 26 September 2022 / Accepted: 6 July 2023

Abstract
The Current deposit is hosted by serpentinized peridotite that intruded rocks of the Quetico Subprovince in the Midcontinent Rift, and is subdivided into three morphologically distinct regions — the shallow and thin Current–Bridge Zone in the northwest, the deep and thick 437–Southeast Anomaly (SEA) Zone in the southeast, and the thick Beaver–Cloud Zone in the middle. The magma parental to the Current deposit became saturated in sulfide as a result of the addition of external S from at least two sources — a deep source characterized by high $\Delta^{33}S$ (< 3‰) values, and a shallow source, potentially the Archean metasedimentary country rocks, characterized by low $\Delta^{33}S$ (< 0.3‰). Variations in $\Delta^{33}S$–S/Se–Cu/Pd values indicate that the contamination signatures were largely destroyed by interaction of the sulfide liquid with large volumes of uncontaminated silicate melt. The intrusion crystallized sequentially, with the Current–Bridge Zone crystallizing first, followed by the Beaver–Cloud Zone, and lastly by the 437–SEA Zone. This, along with the elevated Cu/Pd ratios in the 437–SEA Zone, which formed as a result of sulfide segregation during an earlier saturation event, and development of igneous layering in this zone, suggests that it represents the feeder channel to the Current deposit. After the intrusion crystallized, the base-metal sulfide mineralogy was modified by circulation of late-stage hydrothermal fluids, with pyrrhotite and pentlandite being replaced by pyrite and millerite, respectively. This fluid activity mobilized metals and semi-metals, including Fe, Ni, S, Se, Co, Cu, Ag, and As, but did not affect the PGE. This contribution highlights the importance of the interplay between magma dynamics and magmatic–hydrothermal processes in the formation of Ni–Cu–PGE-mineralized deposits.

Keywords Current deposit · Ni–Cu–PGE · Base-metal sulfide chemistry · S isotopes

Editorial handling: W. D. Maier

✉ M. Brzozowski
matt.brzozow@gmail.com

1 British Columbia Geological Survey, 1810 Blanshard Street, Victoria, BC V8T 4J1, Canada

2 Department of Geology, Lakehead University, 955 Oliver Road, Thunder Bay, ON P7B 5E1, Canada

3 Clean Air Metals, 1004 Alloy Drive, Thunder Bay, ON P7B 6A5, Canada

4 AGC GeoConsulting, 777 Red River Road, Thunder Bay, ON P7B 1J9, Canada

5 Earth Sciences, Memorial University, 230 Elizabeth Avenue, St. John's, NL A1C 5S7, Canada

6 DEL Exploration, Paradise, Paradise, NL A1L 1V6, Canada

Introduction

Magmatic Ni–Cu–platinum-group element (PGE) sulfide deposits form through a series of suprasolidus processes that have been relatively well constrained and which can largely be summarized by four major events — i) generation of a mafic–ultramafic magma via partial melting of the mantle, ii) saturation of a mantle-derived magma in sulfide and segregation of an immiscible sulfide liquid, iii) interaction of the sulfide liquid with the silicate melt and enrichment of metals in the former based, and iv) concentration of the metal-enriched sulfide liquid to form an ore body (Naldrett 2010). While these fundamental processes are commonplace in magmatic Ni–Cu–PGE deposit, the mechanism by which sulfide saturation occurs varies between deposits. Although several mechanisms have been proposed,

Published online: 29 July 2023

including closed-system fractional crystallization, magma mixing, increasing magma fO_2, and addition of externally derived Si or S (Robertson et al. 2015b), most of these, apart from direct addition of S, were deemed incapable of generating economic concentrations of Ni–Cu–PGE mineralization (Ripley and Li 2013). Notable examples of conduit-type Ni–Cu–PGE sulfide deposits that formed via assimilation of distinct contaminants include Norilsk, which was contaminated by anhydrite (e.g., Ripley et al. 2010), Voisey's Bay, which was contaminated by paragneiss (e.g., Ripley et al. 2002), and Jinchuan, which was contaminated by carbonate rock (e.g., Lehmann et al. 2007). Additionally, contamination by geochemically distinct assimilants within a single conduit system has been described in the Eastern Gabbro of the Coldwell Complex (Midcontinent Rift System), in which the Marathon deposit assimilated Archean sedimentary rock and the northern deposits likely assimilated metamorphosed igneous rock (Shahabi Far et al. 2018; Brzozowski et al. 2020). Regardless of how these fundamental processes operate, the sulfide liquid that results eventually crystallizes to the commonly observed assemblage of pyrrhotite–pentlandite–chalcopyrite (Craig and Kullerud 1969; Kullerud et al. 1969).

It is well understood, however, that subsolidus processes have the potential to modify the mineralogy of the base-metal sulfide (BMS) assemblage, as well as the grade and tonnage of the mineralized system (Prichard et al. 2013; Holwell et al. 2017; Brzozowski et al. 2020; Lawley et al. 2020; Wang et al. 2021). These processes, therefore, have the potential to affect the economic value of a mineralized system (Holwell et al. 2017). An example of a mineralized system whose economic potential is believed to have been improved via subsolidus processes is the Roby Zone of the Lac des Iles deposit in northern Ontario, Canada. Although the mineralization at Lac des Iles is unequivocally magmatic (Barnes and Gomwe 2011; Djon and Barnes 2012; Duran et al. 2016), it has been demonstrated that the Pd enrichment in the Roby Zone was the result of upgrading by magmatic–hydrothermal fluids (Watkinson and Dunning 1979; Hinchey and Hattori 2005). Accordingly, the success of mineral exploration and eventual metal extraction depends on having a strong understanding of these supra- and subsolidus processes and a robust mineral deposit model.

The Thunder Bay North Intrusive Complex (TBNIC) of the Midcontinent Rift System contains a series of mafic–ultramafic intrusions, including the 1,106.6 ± 1.6 Ma Ni–Cu–PGE-mineralized Current and Escape intrusions (Fig. 1B) (Bleeker et al. 2020; Kuntz et al. 2022). Although exploration of these two systems has been ongoing since 2005, limited work has been done to characterize the suprasolidus processes that generated the base- and precious-metal mineralization or the subsolidus processes that modified the mineralization. Accordingly, this contribution focuses on characterizing the suprasolidus processes that generated the BMS mineralization along the length of the Current conduit, as well as the subsolidus processes that modified the initial mineralization, with the ultimate goal of developing a robust mineral deposit model. This is accomplished by integrating detailed petrography, whole-rock and BMS chemistry, and multiple S isotopes (^{32}S, ^{33}S, ^{34}S, ^{36}S). This contribution represents one of the first studies to develop a holistic model for a BMS deposit in the Thunder Bay–Nipigon Embayment region. It, therefore, not only has broad implications for the formation of, and exploration for, Ni–Cu–PGE deposits globally, but also lays the foundation for our understanding of deposits in this portion of the Midcontinent Rift System.

Geological setting of the Thunder Bay North Intrusive Complex

The TBNIC is located in the Quetico Subprovice of the Superior Province in northern Ontario, Canada and represents one of several magmatic Ni–Cu–PGE-mineralized complexes that formed as part of the North American Midcontinent rifting event ca. 1.1 Ga (Fig. 1A) (Bleeker et al. 2020; Kuntz et al. 2022). It comprises several mafic–ultramafic chonoliths that straddle the east–west trending Quetico Fault System (Fig. 1B) (Bleeker et al. 2020). From east to west, these intrusions are the Current, 025, Steepledge, and Lone Island intrusions that are connected by dykes–sills of the East–West Corridor (Fig. 1B) (Kuntz et al. 2022).

The 1,106.6 ± 1.6 Ma Current intrusion has been drilled extensively since 2006 (730 drill holes totaling 162,997 m as of 2020) (Kuntz et al. 2022). It defines a ~ 3.4-km-long northwest–southeast-trending chonolith (Figs. 1B and 2) with a "tadpole-shaped" aeromagnetic anomaly that suggests it extends for up to 6 km towards the southeast (Bleeker et al. 2020); this has been verified by drilling. The chonolith comprises undeformed and unmetamorphosed olivine melagabbro, feldspathic lherzolite, and lherzolite, as well as quartz-bearing gabbro/monzonite (Chaffee 2015; Kuntz et al. 2022).

The Current chonolith has been subdivided into i) the Current–Bridge Zone to the north, ii) the 437 Zone–Southeast Anomaly (SEA) to the south, and iii) the Beaver–Cloud Zone in between (Fig. 2a). The Current–Bridge Zone is hosted by granite, whereas the Beaver–Cloud and 437–SEA zones are hosted by metasedimentary country rock (Fig. 2) (Kuntz et al. 2022). The lithology of the Current–Bridge and Beaver–Cloud zones largely comprises peridotite (Fig. 3A–C), whereas the 437–SEA Zone is layered from a lower peridotite to melagabbro to an upper oxide gabbro and capped with a quartz-bearing gabbro/monzonite (Figs. 3D, ESM 1 S1) (Heggie et al. 2015). Northwest of the Quetico Fault in the Current Zone, the chonolith is thin (< 70 m), sinuous, tubular, shallow (< 60 m to its

Fig. 1 (**A**) Simplified geologic map of the North American Midcontinent Rift illustrating the distribution of rock types and highlighting the location of several Ni–Cu–PGE-mineralized intrusions and complexes, including the Thunder Bay North Intrusive Complex (modified from Good et al. 2015). (**B**) Simplified geologic map showing the locations of mafic–ultramafic intrusions of the Thunder Bay North Intrusive Complex, including the Ni–Cu–PGE-mineralized Current and Escape intrusions (modified from Thomas et al. 2011)

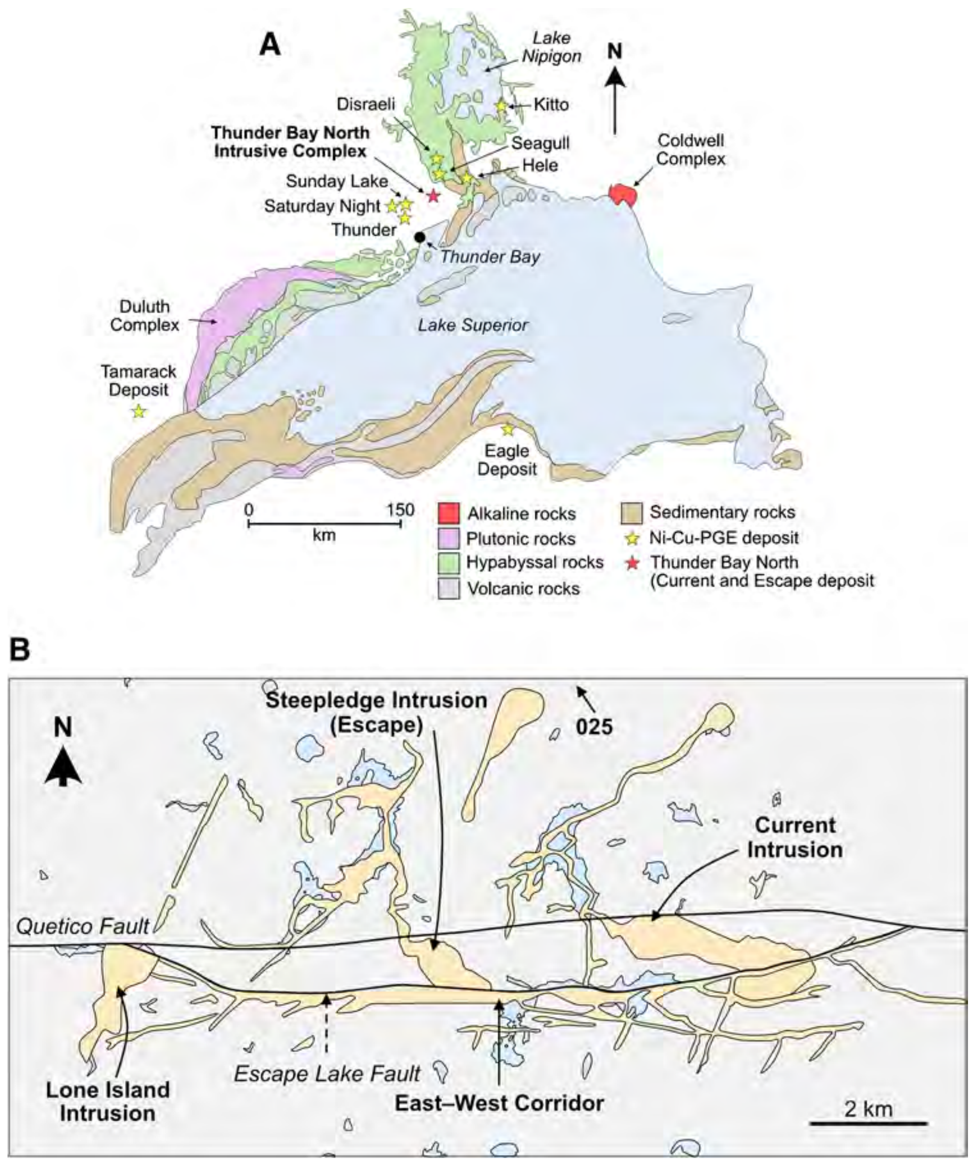

base), and relatively flat lying (Figs. 2B and 3A) (Kuntz et al. 2022). Straddling the Quetico Fault in the Bridge Zone, the chonolith changes to a more stubby, tabular morphology with a gentle southeast plunge to a depth of < 150 m (Figs. 2B and 3B). From the Beaver Zone to the SEA, the chonolith progressively thickens from ~ 150–500 m, is tabular in shape, and extends to progressively greater depths of up to ~ 1,000 m at the base of the SEA (Figs. 2B and 3C, D).

The BMS mineralization in the Current deposit is hosted within the lherzolite and olivine melagabbro (Fig. 3) (Kuntz et al. 2022). This mineralization largely occurs as disseminated pyrrhotite, pentlandite, chalcopyrite, pyrite, and cubanite, with overall abundances ranging from a few percent to > 25%; small bodies of semi-massive to massive sulfide occur at the base of the Bridge and Beaver zones (Fig. 3B, C) (Bleeker et al. 2020; Kuntz et al. 2022). Base-metal sulfides are distributed throughout the chonolith in the Current Zone and the northwest portion of the Bridge Zone, but become bottom loaded in the southeast portion of the Bridge Zone where it meets the Beaver Zone (Fig. 3A–C). Southeast of the Beaver Zone, the majority of BMSs are bottom loaded. The SEA and Cloud Zone are exceptions to these general characteristics, the former containing only minor BMS, and the latter comprising < 1% finely disseminated and irregularly dispersed chalcopyrite ± pyrrhotite at the roof of the chonolith (Fig. 2B).

Samples and methods

The mineralogy and texture of BMS were characterized in 284 thin sections collected along the length of 36 drill holes that intersected the Current, Bridge, Beaver, Cloud, and 437

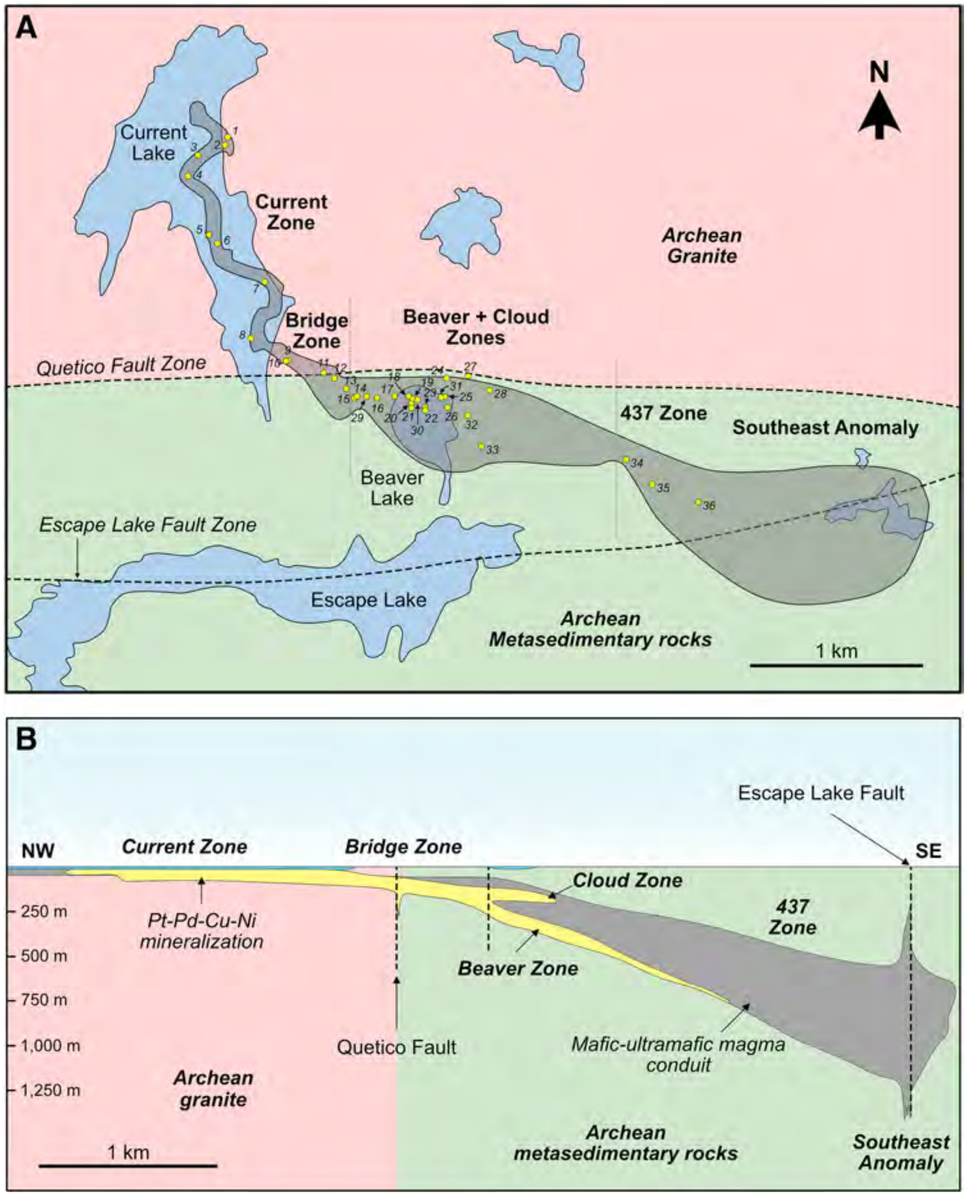

Fig. 2 (**A**) Simplified geologic map illustrating the morphology of the Current intrusion (grey) crosscutting the Archean metasedimentary rocks of the Quetico Subprovince (south of Quetico Fault Zone) and Archean granite (north of the Quetico Fault Zone) in plan view, highlighting the relative locations of the five mineralized zones and the Southeast Anomaly (modified from Chaffee 2015). The yellow circles represent the locations of drill holes from which samples were characterized in this study. The grey dashed lines are the UTM locations where the intrusion has been subdivided into the Current–Bridge, Beaver–Cloud, and 437–SEA zones. (**B**) Schematic cross section of the Current intrusion illustrating the change in morphology of the conduit with depth and the relative location of sulfide mineralization in the five zones (modified from Thomas et al. 2011)

zones, as well as the SEA (Fig. 2A). Five samples of the granite country rock and two samples of the metasedimentary country rock were also characterized (Fig. 2A). Mineral Liberation Analysis (MLA) was conducted on ten thin sections at the CREAIT facility at Memorial University of Newfoundland using an FEI Quanta 400 scanning electron microscope (SEM) equipped with a Bruker XFlash energy dispersive X-ray (EDX) detector and mineral liberation analysis software. Operation conditions of the instrument are provided in the Electronic Supplementary Material (ESM 1).

Bulk-rock geochemical data comprise assays for base metals (Cu), precious metals (Pd, Pt, Ir), and S that were used by Clean Air Metals to define the Current deposit. The vast majority of the assay data were determined at ALS (~98% of the database), with the remaining ~2% determined at Accurassay Laboratories. Quality assurance and control for these analyses were performed throughout the exploration process to meet the requirements of the National Instrument 43–101. All bulk-rock data utilized herein represent rocks with Pd > 0.01 ppm. Details regarding the analytical methods used to collect the bulk-rock data are provided in the Electronic Supplementary Material (ESM 1)

The trace-element contents of BMS from 65 polished thin sections and pucks from 31 drill holes were determined at the Element and Heavy Isotope Analytical Laboratory at the University of Windsor using an Agilent 7900 ICP–MS coupled with a 193-nm excimer laser. The accuracy of the measured concentrations was assessed by comparing the measured values of sulfide reference UQAC FeS-1 (University du Québec à Chicoutimi, Canada) and MASS-1 to the working values; the measured values are in good agreement with the working values (ESM 2

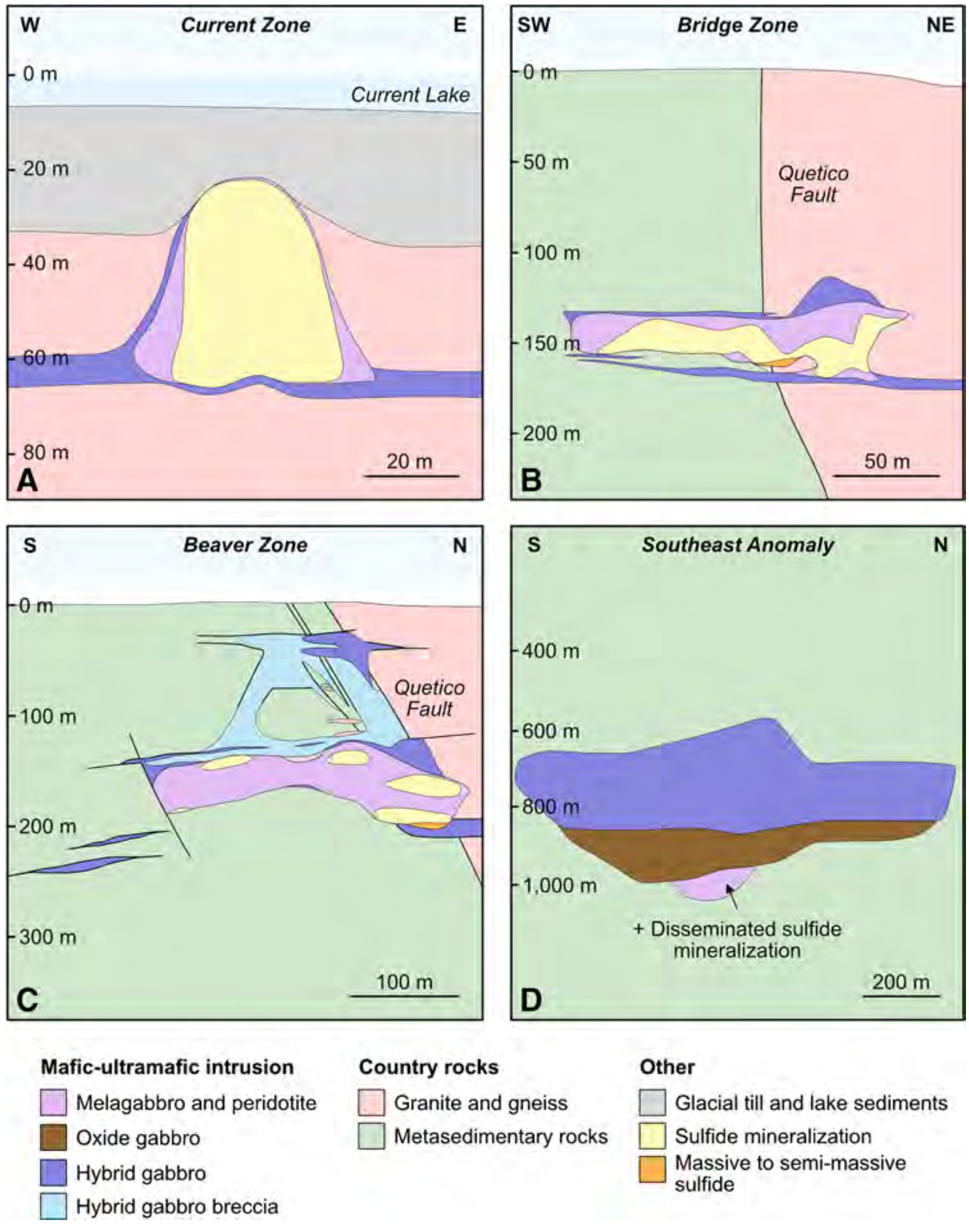

Fig. 3 Schematic cross sections of the (**A**) Current Zone, (**B**) Bridge Zone, (**C**) Beaver Zone, and (**D**) Southeast Anomaly illustrating the relationships of the main rock units in the conduit, the change in conduit morphology from northwest to southeast along the intrusion, and the change in location of mineralization that accompanies this change in morphology (modified from Thomas et al. 2011; Bleeker et al. 2020)

Table S1). Details regarding instrument operating conditions, standardization, correction of metal argide interferences, and signal processing are provided in ESM 1.

The S isotope composition (^{32}S, ^{33}S, ^{34}S, ^{36}S) of BMS was determined in situ using a CAMECA IMS 1280 secondary ion mass spectrometer at the Centre for Microscopy, Characterisation and Analysis, University of Western Australia. Details regarding instrument operating conditions, standardization, and data processing are provided in ESM 1. Sulfur isotope values are reported in delta notation as permil deviations from Vienna Canyon Diablo troilite. Mass-independent fractionation was assessed by calculating the deviation of the measured values from mass-dependant fractionation ($\Delta^{33}S = \delta^{33}S - 1{,}000 \times [(1 - \delta^{34}S)^{0.515} - 1]$, $\Delta^{36}S = \delta^{36}S - 1{,}000 \times [(1 - \delta^{34}S)^{1.91} - 1]$). Accuracy of the sample measurements was assessed by measuring the isotopic composition of the Nifty-b chalcopyrite, VMSO pentlandite, Alexo pyrrhotite, and Sierra pyrite standards. Their measured compositions are in excellent agreement with the reference values provided by LaFlamme et al. (2016) (ESM 2 Table S2).

Results

Bulk-rock geochemistry

In metal–S space, Cu and PGE generally correlate positively with S concentrations, but there is a subgroup within which chalcophile elements exhibit no discernable correlation with S (Fig. 4A, B). Similarly, when comparing the Pt-group PGE (PPGE) and Ir-group PGE (IPGE), Pd correlates positively with both Pt (Pd/Pt = 0.9 ± 0.4, average ± 2SD; Fig. 4C) and Ir (Pd/Ir = 21 ± 131; Fig. 4D).

Base-metal sulfide mineralogy

The samples that were characterized for this study comprise variably mineralized mafic–ultramafic rocks from the chonolith, granitic country rocks, and samples where the two have mingled (Fig. 5A). Base-metal sulfides are largely disseminated (Fig. 5B), but can be net-textured (Fig. 5C) and blebby (Fig. 5D). The latter sulfide variety can be mineralogically segregated, with a portion comprising pyrrhotite–pentlandite and portion comprising chalcopyrite (Fig. 5D); a fine-grained assemblage of silicate minerals commonly surrounds the chalcopyrite (Fig. 5D).

The BMS assemblages throughout the Current intrusion comprise variable proportions of pyrrhotite, pentlandite, chalcopyrite, and pyrite, with lesser cubanite, millerite, violarite, and rare troilite and gersdorffite. Chalcopyrite, pyrrhotite, and pentlandite largely occur as equilibrium assemblages with sharp, curved contacts (Fig. 5E). Pyrrhotite can occur as single large (mm-sized) crystals (Fig. 5E, F) or as aggregates of numerous fine-grained (tens of microns) crystals that share ~ 120° angles; these textural varieties of pyrrhotite can occur within the same thin section (Fig. 5F). Troilite occurs as wavy intergrowths in pyrrhotite. Pentlandite can occur as large (hundreds of microns) crystals associated with chalcopyrite–pyrrhotite assemblages (sometimes at the contact between the two), as flames within pyrrhotite (Fig. 5E), and in veinlets that crosscut pyrite (similar to pyrrhotite in Fig. 5G). Cubanite occurs as laths within chalcopyrite (Fig. 5E, F).

Pyrite generally occurs in disequilibrium with pyrrhotite (Fig. 5H), as large (mm-sized) crystals either associated with chalcopyrite–pentlandite–cubanite or isolated from other BMS, and as wormy intergrowths in chalcopyrite (Fig. 5I). Rarely, chalcopyrite associated with pyrite can occur isolated within alteration patches (Fig. 5J). Locally, pyrite can occur as blocky intergrowths with pentlandite (Fig. 5K). Millerite occurs as aggregates of irregular crystals in chalcopyrite; it is most common in samples that contain pyrite (Fig. 5L). Violarite occurs along fractures in pentlandite (Fig. 5M). Gersdorffite occurs as anhedral–euhedral grains within chalcopyrite, pyrite, and silicates (Fig. 5N).

The visual proportion of pyrite to other BMS varies significantly within the sample population, with some samples having no pyrite, others being composed entirely of chalcopyrite–pyrite, and no pyrrhotite, and others comprising pyrrhotite–pentlandite–chalcopyrite–pyrite–millerite. Mineral abundance data obtained via MLA on ten samples confirm this thin section-scale variability in sulfide mineralogy (Fig. 6). Of note is that the abundances of pyrrhotite and pyrite exhibit a clear negative and non-linear correlation (Fig. 6D). This mineralogical variability matches that

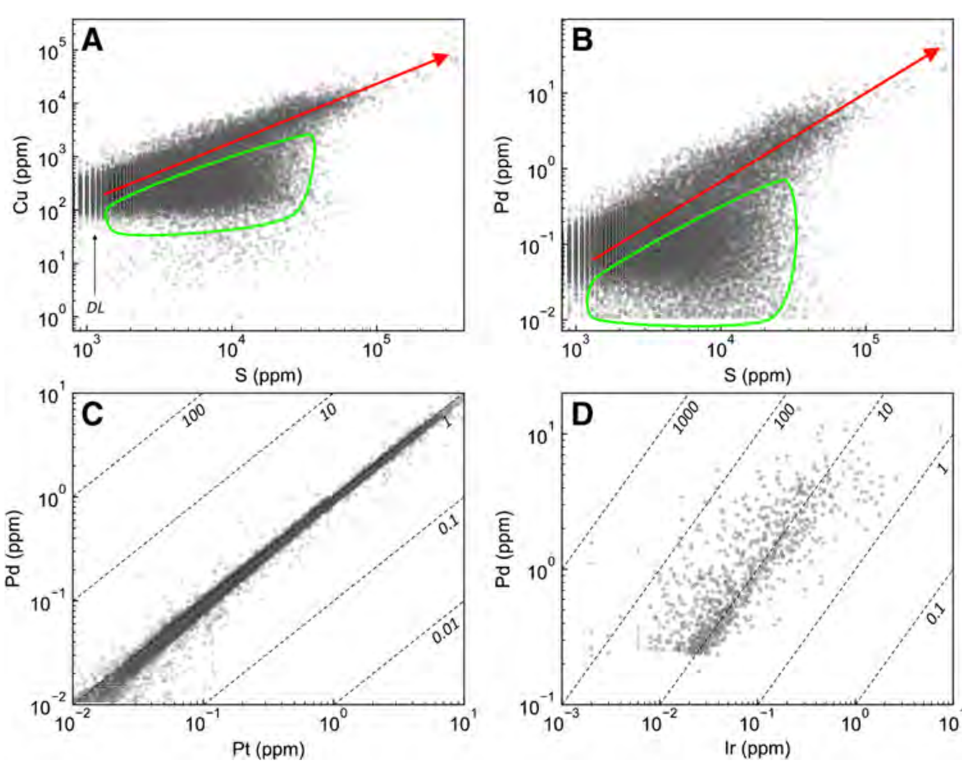

Fig. 4 Binary diagrams illustrating the variation in bulk-rock (**A**) Cu–S, (**B**) Pd–S, (**C**) Pd–Pt, and (**D**) Pd–Ir. The red arrow highlights data that exhibits a positive trend on these diagrams, whereas the green field highlights data that falls off this trend. Dashed lines represent constant Pd/Pt and Pd/Ir ratios. DL = detection limits

obtained on a larger sample population by Clean Air Metals (grey squares in Fig. 6). Within this larger sample set, it is also evident that a similar negative and non-linear correlation exists between pentlandite and millerite (Fig. 6E).

Base-metal sulfide trace-element chemistry

Distribution among BMS

The trace-element chemistry of the six most common BMS throughout the Current deposit is provided in ESM 2 Table S3 and illustrated in Fig. 7. In the Current deposit, the order of decreasing Co contents is pentlandite = millerite > pyrite > pyrrhotite > chalcopyrite–cubanite (Fig. 7A). Iron-rich BMS consistently have lower Zn concentrations than Cu-rich BMS (Fig. 7A). Palladium, Pt, and Au exhibit similar ranges of concentration (up to three orders of magnitude) that are generally indistinguishable among the BMS, apart from pentlandite, which has consistently elevated Pd contents (up to 208 ppm), and some pyrite that extend to elevated Pd values similar to pentlandite (Fig. 7B–D). The concentrations of the IPGE (Os, Ir, Ru) among the BMS are indistinguishable and exhibit similar ranges (e.g., four orders of magnitude for Ir; Fig. 7E–G). Silver and Sn exhibit similar distributions among the BMS, with their concentrations generally decreasing in the order chalcopyrite > pyrrhotite–pentlandite–millerite > pyrite (Fig. 7H, I). The concentration of As typically extends to higher values in pyrite compared to chalcopyrite–pyrrhotite–pentlandite; Bi exhibits a mirrored distribution (Fig. 7J, K). The concentration of Se in chalcopyrite, pyrrhotite, pentlandite, and millerite is similar and exhibits relatively limited variability, whereas its concentration in pyrite extends to notably lower values than in the other BMS (Fig. 7L).

Cu/Pd and S/Se values

Bulk-rock Cu/Pd ratios of samples from the Current–Bridge (1,892–3,275) and Beaver–Cloud (1,902–4,100) zones are largely indistinguishable, exhibit limited variability, and fall entirely within the range of mantle values (Fig. 8). The 437–SEA Zone has consistently higher and more variable Cu/Pd ratios (3,166–42,444, Fig. 8).

The S/Se values of chalcopyrite (942–8,480), pyrrhotite (1,731–7,158), and pentlandite (1,597–4,076) are indistinguishable and will be considered together (Fig. 8A). Pyrite and millerite are considered separately as they are secondary BMS. Based on the primary BMS assemblage, the S/Se values of the Current–Bridge (942–5,880), Beaver–Cloud (1,706–15,023), and 437–SEA (1,597–6,180) zones overlap and are generally indistinguishable (Fig. 8A). These S/Se values extend to lower and higher values than those of the mantle (Fig. 8A). Pyrite and millerite in the Current deposit are characterized by S/Se values that are notably more variable than the primary BMS assemblage, ranging from 979 to 23,091, and extend to values notably lower and higher than the mantle range (Fig. 8B). Pyrite from a granite country rock sample with Cu/Pd of 4,500 has S/Se values of 30,066–64,426 (Fig. 8). Pyrite from two metasedimentary country rock samples with Cu/Pd of 34,000–59,000 have S/Se values of 12,848–82,249 (Fig. 8).

Multiple sulfur isotopes

The overall S isotope composition of the Current deposit (-0.06‰ to 0.36‰ $\Delta^{33}S$ and -2.4‰ to 2.30‰ $\delta^{34}S$, ESM 2 Table S4) largely falls within the range of mantle values, although several samples have $\Delta^{33}S$ values that are distinctly higher than mantle (Fig. 9A). The overall S isotope compositions of the BMS, both primary and secondary, are indistinguishable (Fig. 9A, B). Similarly, the S isotope compositions of BMS in the Current–Bridge and Beaver–Cloud zones are also largely indistinguishable (Fig. 9A, B). Notably, there is no significantdifference in the S isotope composition of texturally distinct BMS (Fig. 5B–D) or those associated with mafic magma–granite magma mingling (Fig. 5A) (ESM 2 Table S4). In $\Delta^{33}S$–Cu/Pd–S/Se space, BMS generally exhibit horizontal trends, with large variability in isotope composition and limited variability in Cu/Pd and S/Se values, apart from a few samples from the 437–SEA Zone with elevated Cu/Pd, and pyrite with elevated S/Se values (ESM 1 Figs. S3A, B).

Discussion

Origin of the pyrite–millerite assemblage in the Current deposit

Although pyrite and millerite can form via magmatic processes by recrystallization from monosulfide solid solution (MSS), this only occurs in sulfide liquids characterized by elevated S/metal ratios (approximately 40 wt. % S at 600 °C) (Naldrett et al. 1967; Kullerud et al. 1969; Craig 1973). Most sulfide liquids, however, do not achieve such high S/metal ratios, and so primary pyrite in magmatic sulfide deposits is quite rare (Piña et al. 2016). Formation of magmatic millerite is largely restricted to Ni-rich komatiitic ores, whereas those that occur in mafic–ultramafic systems are largely the result of low-temperature alteration of pentlandite (Barnes et al. 2011; Duran et al. 2015). Given these physicochemical constraints, the occurrence of pyrite as anhedral, pitted grains (Fig. 5H–L) rather than the euhedral grains expected for primary pyrite (e.g., Dare et al. 2011; Duran et al. 2015; Piña et al. 2016), the disequilibrium textures exhibited in pyrite–pyrrhotite (Fig. 5H) and pentlandite–millerite assemblages, the patchy chemical zonation in pyrite (ESM 1 Fig. S2E), and the

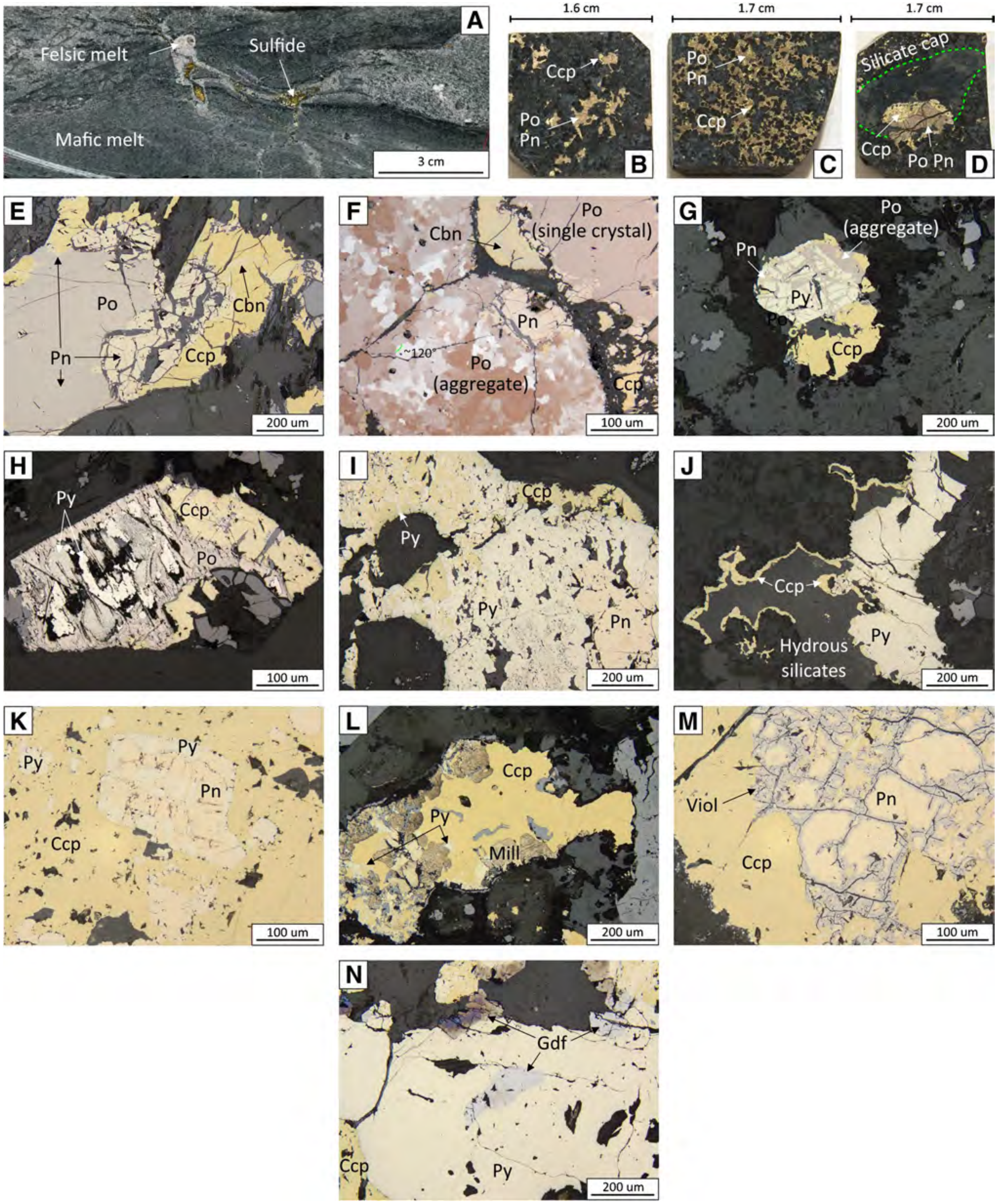

inverse correlation between the abundance of pyrrhotite–pyrite and pentlandite–millerite (Fig. 6D, E), it is likely that the pyrite and millerite in the Current deposit are not magmatic in origin, but rather formed by the low-temperature (<230 °C; Naldrett and Kellurud 1967; Naldrett et al. 1967; Craig 1973; Misra and Fleet 1974) alteration of pyrrhotite and pentlandite, respectively. This characterization will be used throughout the discussion when characterizing magmatic and hydrothermal processes.

◂**Fig. 5** Images of drill core samples (**A–D**) and reflected-light photomicrographs (**E–N**) illustrating representative examples of base-metal sulfides and textures in the Current deposit. (**A**) Mingling between the mafic Current magma and a felsic melt. Note the occurrence of base-metal sulfides where the two magmas mingled. (**B**) Disseminated, (**C**) net-textured, and (**D**) blebby base-metal sulfide mineralization. (**E**) An equilibrium (magmatic) assemblage comprising pyrrhotite–pentlandite–chalcopyrite–cubanite. (**F**) Cross-polarized, reflected-light photomicrograph illustrating pyrrhotite occurring as a single crystal and as an aggregate of multiple crystals. Note the 120° dihedral angles between crystals in the latter. (**G**) Pyrite partially replaced by pyrrhotite. (**H**) Pyrrhotite partially replaced by pyrite. (**I**) An assemblage comprising chalcopyrite–pentlandite–pyrite. (**J**) Chalcopyrite restricted to an alteration patch and physically associated with pyrite. (**K**) An assemblage of chalcopyrite–pentlandite–pyrite in which the pyrite was partially replaced by pentlandite. (**L**) An assemblage of chalcopyrite–millerite–pyrite. (**M**) An assemblage comprising largely chalcopyrite–pentlandite, with violarite occurring along fractures in pentlandite. (**N**) An assemblage of chalcopyrite–pyrite–gersdorffite. Po = pyrrhotite, Pn = pentlandite, Ccp = chalcopyrite, Cbn = cubanite, Py = pyrite, Mill = millerite, Viol = violarite, Gdf = gersdorffite

Sulfide saturation and metal enrichment–depletion

Many primary BMS in the Current deposit are characterized by mantle S/Se values (2850–4350; Eckstrand and Hulbert 1987; Palme and O'Neil 2014), but significant variability towards values greater and lower than mantle is also observed (Fig. 8A). Likewise, although BMS at Current are characterized by Δ^{33}S–δ^{34}S values that are largely within range of mantle values ($\Delta^{33}S = 0 \pm 0.1‰$, $\delta^{34}S = 0 \pm 2‰$; Lesher and Burnham 2001; Farquhar 2002; Ripley and Li 2003; Bekker et al. 2009), several BMS have Δ^{33}S that are distinctly higher than the mantle (Fig. 9A, D, F). Although variations in R factor alone can explain the lower-than-mantle S/Se and mantle-like Δ^{33}S values (ESM 1 Fig. S4), it cannot explain the elevated S/Se and Δ^{33}S values. These elevated values must, therefore, represent the addition of S from an external source. Given the mantle-like δ^{34}S for all of the BMS and elevated Δ^{33}S (Fig. 9), it seems likely that the contaminant was Archean in age as these isotopic signatures are diagnostic of Archean sedimentary reservoirs (Farquhar and Wing 2003, 2005).

The country rocks provide a potential local source of S as they comprise Archean metasedimentary, and granitic rocks of the Quetico Subprovince (Hart and MacDonald 2007). Although there is limited S isotopic data on these country rocks, the data that are available for the Archean Quetico metasedimentary rocks demonstrate that it is heterogeneous, with δ^{34}S values in the range of -3.03‰ to 0.61‰ and Δ^{33}S values in the range of 0.01‰ to 0.29‰ (Caglioti 2023). Considering this heterogeneity, the fact that the Quetico Subprovince represents a mixture of crustal sources (Williams 1991), and the significant variability of Δ^{33}S during the Archean (Farquhar et al. 2010), it is possible that the Quetico metasedimentary rocks contain S with highly variable and positive Δ^{33}S values. Similarly, there is no isotopic data available for the Archean granitic country rocks into which the northern portion of the Current intrusion intruded, but the lack of deviation of δ^{34}S–Δ^{33}S from mantle values of sulfides hosted within a mixture of mafic magma and felsic country rock melt (Fig. 5A, ESM 2 Table S3) suggests that the granitic country rocks do not contain a significant mass independent fractionation (MIF) signal. Lastly, it is also possible that S was sourced from Archean rocks at depth, which has been suggested for other Ni–Cu–PGE-mineralized intrusions in the Midcontinent Rift System, including the Marathon deposit (Shahabi Far et al. 2018; Brzozowski et al. 2020, 2021) and Duluth Complex (Ripley et al. 2007).

It has been well documented that contamination signatures recorded by S isotopes and S/Se values can be diluted by interaction of the contaminated sulfide liquid with uncontaminated pulses of silicate melt (Lesher and Burnham 2001; Ripley and Li 2003; Hiebert et al. 2013, 2016; Queffurus and Barnes 2015; Smith et al. 2016, 2021; Shahabi Far et al. 2018; Brzozowski et al. 2020, 2021), with complete destruction of the geochemical–isotopic signatures at R factors > 1,000 (ESM 1 Fig. S4). Considering the importance of R factor to the enrichment of sulfide liquids in metals in Ni–Cu–PGE deposits, particularly volumetrically small, conduit-type, PGE-rich systems like Current (Figs. 2 and 3), it is possible that the largely mantle-like S isotope and S/Se values of BMS that extend towards non-mantle values may be the product of dilution caused by variably high R factors of < 10,000. To assess this, the S isotope and S/Se values of BMS, and bulk-rock Cu/Pd values are compared to compositions modeled using the R factor equations of Ripley and Li (2003).

Copper, Pd, and Se concentrations are modelled following the closed-system R factor equation of Ripley and Li (2003) and employing sequential steps of batch equilibration:

$$C^{metal}_{sul_f} = \frac{C^{metal}_{sul_i} + (R * C^{metal}_{sil_i})}{1 + \frac{R}{D^{metal}_{sul-sil}}} \tag{1}$$

The parameters $C^{metal}_{sul_i}$ and $C^{metal}_{sul_f}$ are the initial and final concentrations of a metal in the sulfide liquid, respectively, $C^{metal}_{sil_i}$ is the initial concentration of a metal in the silicate melt, R is the incremental R factor (i.e., the R factor of each individual pulse of magma), and $D^{metal}_{sul-sil}$ is the sulfide liquid–silicate melt partition coefficient for a given metal. Sulfur isotopes are modeled using the open-system R factor equation (Ripley and Li 2003):

$$dS_{sul_f} = \frac{dS_{sul_i} + R^o\left(dS_{sil_i} + \Delta S_{sul-sil}\right)}{1 + R^o}, where\ R^o = \frac{C^S_{sil}}{C^S_{sul}} * R \tag{2}$$

Fig. 6 Binary diagrams illustrating the variation in abundances of (**A**) chalcopyrite–pyrrhotite, (**B**) pentlandite–pyrrhotite, (**C**) chalcopyrite–pyrite, (**D**) pyrrhotite–pyrite, (**E**) pentlandite–millerite obtained by mineral liberation analysis. Note the strong negative, non-linear correlation between the abundances of pyrrhotite–pyrite and pentlandite–millerite. The grey squares are data from an unpublished metallurgical study by Clean Air Metals Inc

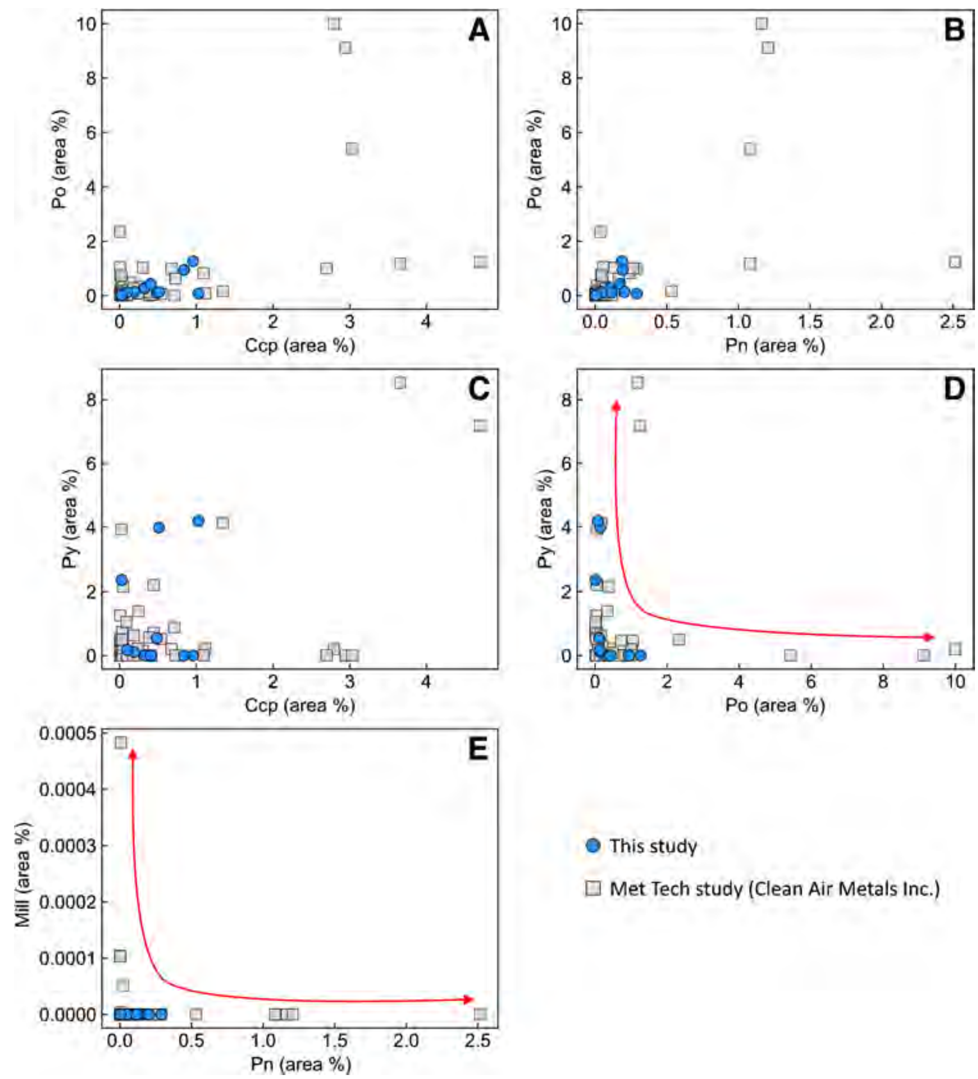

The parameters dS_{sul_i} and dS_{sul_f} correspond to the initial and final (after sulfide liquid–silicate melt interaction) S isotope compositions of the sulfide liquid, respectively, dS_{sil_i} is the initial S isotope composition of the incoming silicate melt, $\Delta S_{sul-sil}$ is the S isotope fractionation factor between sulfide liquid and silicate melt, and C^S_{sil} and C^S_{sul} are the concentrations of S in the silicate melt and sulfide liquid, respectively. Values used for the model parameters are provided in Table 1, along with an explanation of why the values were chosen. Given the likelihood that the contaminant was Archean in age and the overall mantle-like δ^{34}S values of the samples (Fig. 9), modeling focused on Δ^{33}S–S/Se–Cu/Pd. Because the nature of the Archean contaminant is not known, modeling was done using several contaminant starting compositions representing assimilation of S with a range of Δ^{33}S values from mantle-like (0.1‰), to those similar to metasedimentary pyrite in the Quetico Subprovince (up to 0.3‰; Caglioti 2023), to those notably higher than mantle (1‰, 3‰, and 10‰); these values are within the range of Δ^{33}S values of Archean sedimentary reservoirs (Farquhar and Wing 2003, 2005; Farquhar et al. 2010).

According to the model, as R factor increases from 100 to ~10,000, the S/Se value of the sulfide liquid decreases more rapidly than the Cu/Pd ratio, whereas at R factors > 10,000, the opposite is observed, with S/Se being essentially invariable and Cu/Pd decreasing significantly (Fig. 10A). The Cu/Pd–S/Se data from the Current deposit generally follows the model trend at R factors < 10,000, exhibiting limited variability in Cu/Pd values, but significant variability in S/Se values (Fig. 10A). This suggests that i) the sulfide liquid at Current experienced R factors < 10,000, consistent with R factors estimated from bulk-rock Cu and Pd (Fig. 11), and ii) the silicate melt assimilated material that was characterized by elevated S/Se values. Based on the modeling, the minimum S/Se value of the contaminant was likely in the range of 36,000, which is within the

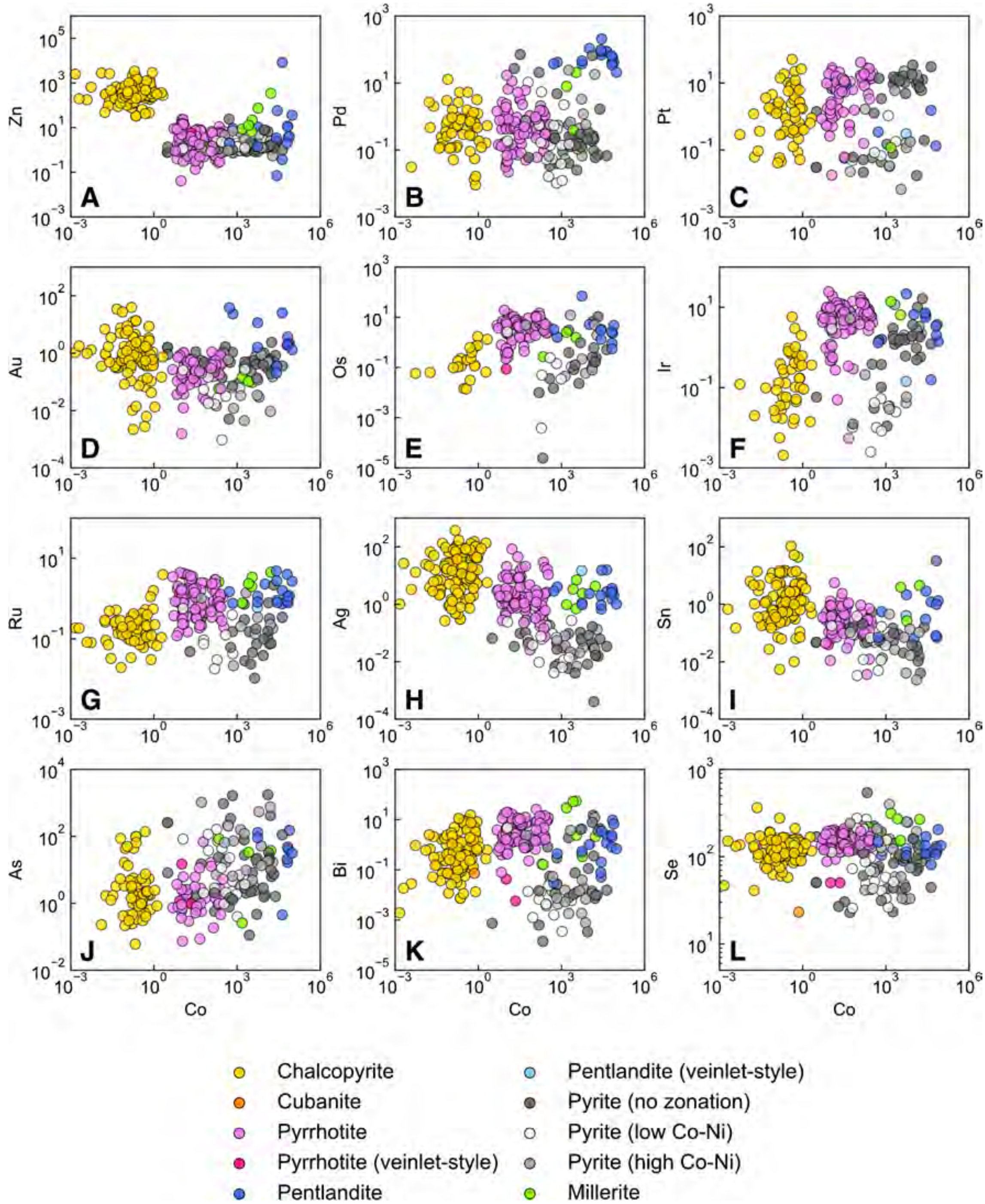

Fig. 7 Binary diagrams illustrating the variation in metal (**A–H**) and semi-metal (**I–L**) concentrations in base-metal sulfides as a function of Co concentration. All concentrations are in ppm

range of values of pyrite in the Archean Quetico granitic (30,066–64,426, ESM 2 Table S3) and metasedimentary country rocks (12,848–82,249; Caglioti 2023).

The modeled variations in Cu/Pd–$\Delta^{33}S$ exhibit similar trends for all of the hypothetical contaminants, with significant variability in $\Delta^{33}S$ at R factors < 10,000, and essentially no variability in $\Delta^{33}S$ at R factors > 10,000 (Fig. 10B), similar to S/Se. The model curves for the various contaminants in S/Se–$\Delta^{33}S$ space exhibit distinct trends based on how positive the $\Delta^{33}S$ value of the contaminant is, with the overall slope of the curves increasing with isotopically lighter contaminants (Fig. 10C). Two things are evident

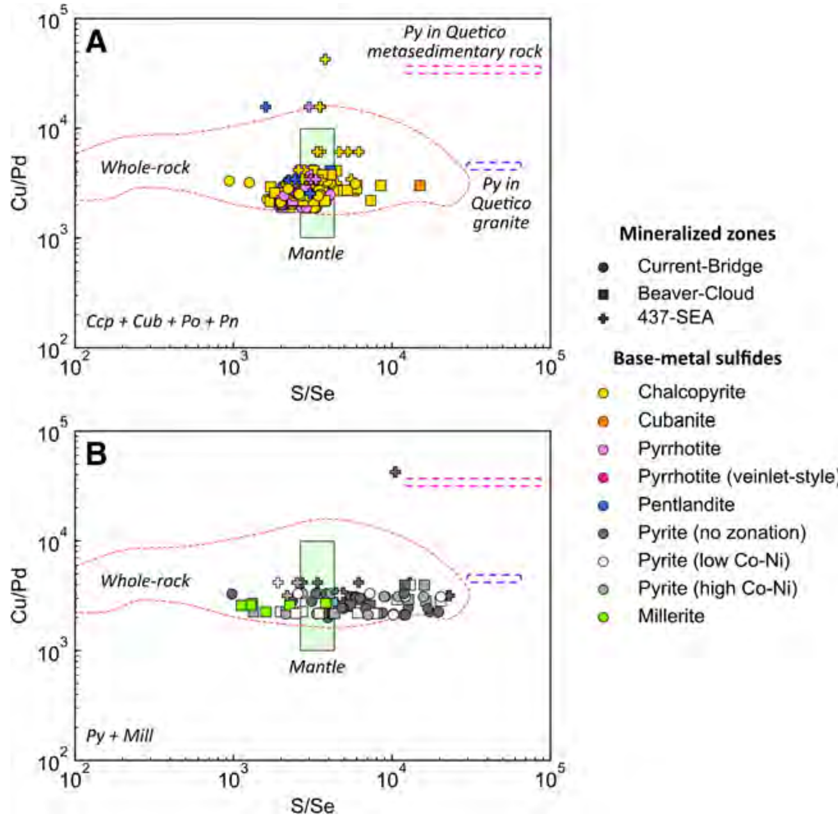

Fig. 8 Binary diagrams illustrating the variation in bulk-rock Cu/Pd and sulfide S/Se in (**A**) the primary chalcopyrite–cubanite–pyrrhotite–pentlandite assemblage and (**B**) the secondary pyrite–millerite assemblage. The red, dashed field outlines the range of bulk-rock Cu/Pd and S/Se values. The purple and pink dashed fields represents the bulk-rock Cu/Pd ratio of Archean granitic and metasedimentary country rock and S/Se of its pyrite ($n_{Py}=2$ and $n_{Py}=4$, respectively); data for metasedimentary pyrite is from Caglioti (2023). The mantle ranges for Cu/Pd (1,000–10,000) and S/Se (2,632–4,350) are from Barnes et al. (1993, 2015b), and Eckstrand and Hulbert (1987) and Palme and O'Neil (2014), respectively

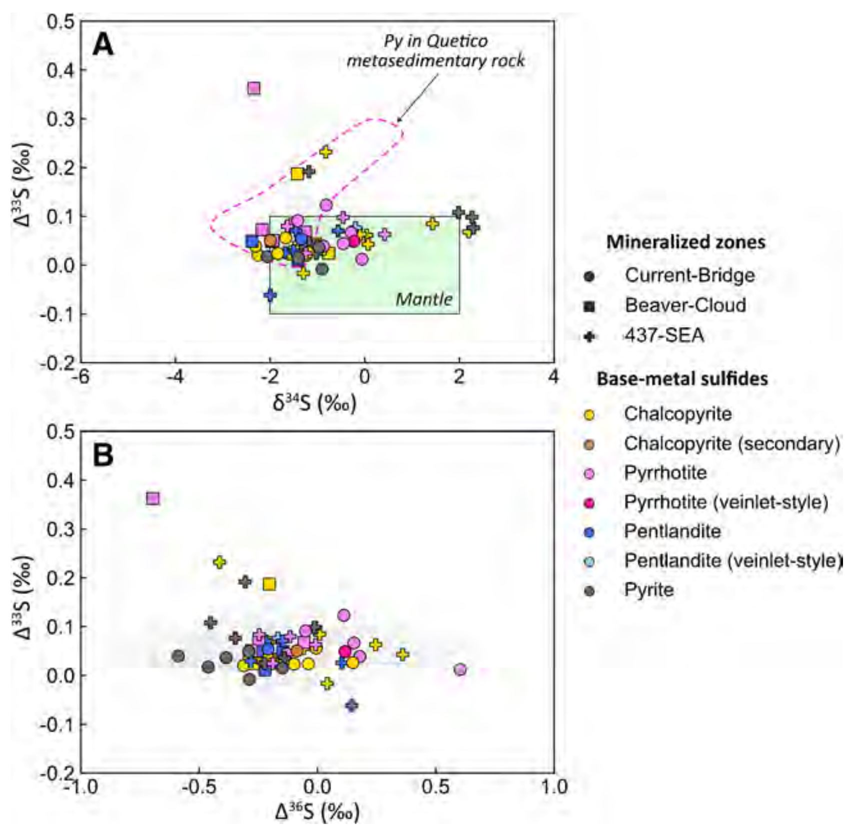

Fig. 9 Binary diagrams illustrating the variation in (**A**) $\Delta^{33}S$–$\delta^{34}S$ and (**B**) $\Delta^{33}S$–$\Delta^{36}S$ of base-metal sulfides. The mantle range for $\Delta^{33}S$ is from Farquhar (2002) and Bekker et al. (2009), and for $\delta^{34}S$ is from Lesher and Burnham (2001) and Ripley and Li (2003). The mantle ranges for Cu/Pd (1,000–10,000) and S/Se (2,632–4,350) are the same as in Fig. 8. The pink, dashed field highlights the composition of pyrite from Quetico metasedimentary rocks from Caglioti (2023). Error bars for S isotopes are 2σ

Table 1 Parameters for numerical modeling

	Value	Note	Reference
Silicate melt			
$Cu_{sil.i}$	100	Similar to the values of the theoretical parental melt to the Current deposit.	Heggie (2012)
$Pd_{sil.i}$	0.01		
$Cu/Pd_{sil.i}$	10000		
S_{sil}	400	Similar to the median S content of unmineralized dikes and volcanic rocks in the Midcontinent Rift north of Lake Superior.	Cundari et al. (2021)
$Se_{sil.i}$	0.10	Calculated by maintaining a mantle S/Se ratio of 4,000.	Brzozowski et al. (2021)
$S/Se_{sil.i}$	4000	Within the range of mantle values (2,632-4,350).	Eckstrand and Hulbert (1987), Palme and O'Neil (2014)
$\Delta^{33}S_{sil.i}$	0	Within the range of mantle S isotope values.	
Sulfide liquid			
$Cu_{sul.i}$	80000	Within the range of metal tenors in the Current deposit. Calculated using assay data and the method of Kerr (2003).	Kerr (2003)
$Pd_{sul.i}$	25		
S_{sul}	360000	Sulfur content similar to pyrrhotite-pentlandite-chalcopyrite.	
$Se_{sul.i}$	10	Within the range of bulk-rock values of other Ni–Cu–PGE deposits globally. Minimum value required to generate the high S/Se ratios observed in the Current sulfides. Does not significantly affect the model at high R factors (>1,000).	Queffurus and Barnes (2015)
$S/Se_{sul.i}$	36000	Serves as the starting contaminated composition.	
$\Delta^{33}S_{sul.i}$ (Model 1)	0.1	Model in which the contaminant has a mantle-like $\Delta^{33}S$ value.	
$\Delta^{33}S_{sul.i}$ (Model 2)	0.3	Model in which the contaminant has a $\Delta^{33}S$ value similar to sedimentary pyrite of the Archean Quetico Subprovince.	Caglioti, unpublished MSc thesis
$\Delta^{33}S_{sul.i}$ (Model 3)	1	Models in which the contaminant has $\Delta^{33}S$ values heavier than mantle.	Farquhar and Wing (2003, 2005), Farquhar et al. (2010)
$\Delta^{33}S_{sul.i}$ (Model 4)	3		
$\Delta^{33}S_{sul.i}$ (Model 5)	10		
Other parameters			
R	100		
R^o	0.11		
$\Delta S_{sul\text{-}sil}$	0.00		Ripley and Li (2003)
$D^{Cu}{}_{sul\text{-}sil}$	2130	Maximum sulfide liquid-silicate melt partition coefficients.	Barnes and Ripley (2016)
$D^{Pd}{}_{sul\text{-}sil}$	536000		
$D^{Se}{}_{sul\text{-}sil}$	2339		

All concentrations are in ppm. S isotopes are in permille

from the model curves and distribution of Current data. First, it seems unlikely that the contaminant(s) had $\Delta^{33}S$ values greater than 3‰ as the Current data have S/Se values notably higher than those predicted by models using such contaminants (Fig. 10C). Second, none of the contaminant models individually can explain the distribution of BMS compositions at Current, with some BMS having mantle-like $\Delta^{33}S$, but elevated S/Se values, and others having high $\Delta^{33}S$, but mantle-like S/Se values (Fig. 10C). The elevated Cu/Pd values of the 437–SEA Zone (Fig. 10A, B) indicate that the silicate melt(s) from which they crystallized must have lost < 0.1% of their sulfide liquid prior to or during intrusion (Fig. 10A, B). It is possible that the elevated S/Se values in this zone are also the result of sulfide removal rather than contamination. This scenario seems unlikely, however, as generating S/Se values in the range of 6,000 would require removal of > 10% sulfide liquid from the melt, which would have severely depleted the melt in Pd (Fig. 10). Rather, the distribution of data suggests that the Current magma(s) assimilated externally derived S from isotopically distinct reservoirs, some of which had mantle-like $\Delta^{33}S$ and others that had high $\Delta^{33}S$ values of up to 3‰ (Fig. 10C).

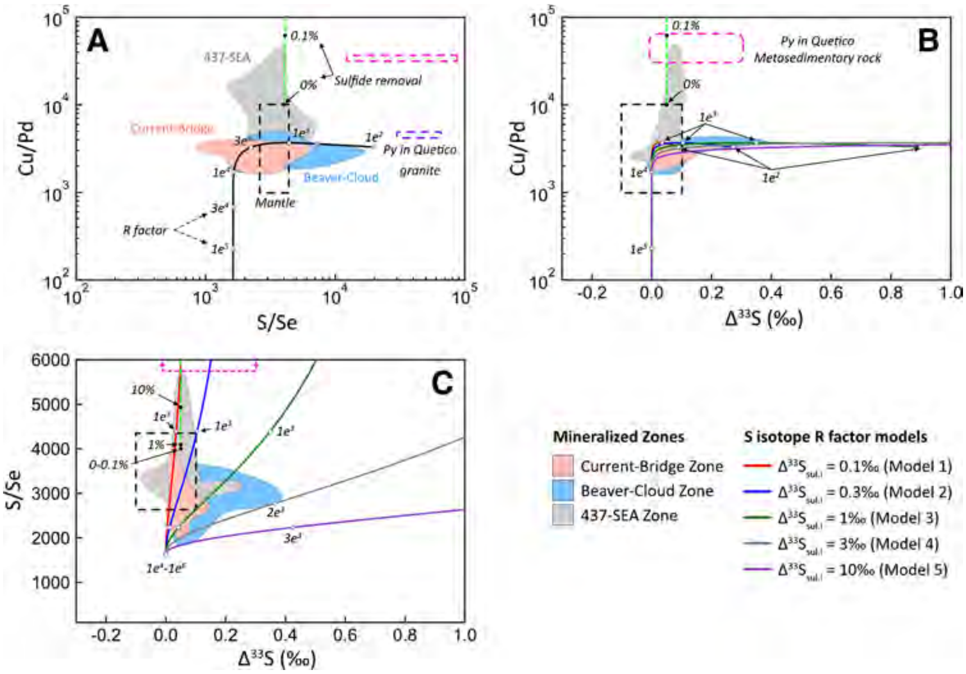

Fig. 10 Binary diagrams illustrating the modeled variations in (**A**) S/Se–bulk-rock Cu/Pd, (**B**) Δ^{33}S–bulk-rock Cu/Pd, and (**C**) Δ^{33}S–S/Se as a function of variable R factor and contamination by rocks with different Δ^{33}S values (colored, solid lines). The green, dashed line represents modeled compositional variations as a function of sulfide liquid removal. The colored fields represent the S/Se ratio of primary chalcopyrite–cubanite–pyrrhotite–pentlandite in the different mineralized zones and bulk-rock Cu/Pd. References for the mantle ranges are the same as those in Fig. 9. The purple and pink dashed fields represents the bulk-rock Cu/Pd ratio of Archean granitic and metasedimentary country rock and S/Se of its pyrite; data for metasedimentary pyrite is from Caglioti (2023). The numbers on the model curves represent R factor and the degree of sulfide liquid removal

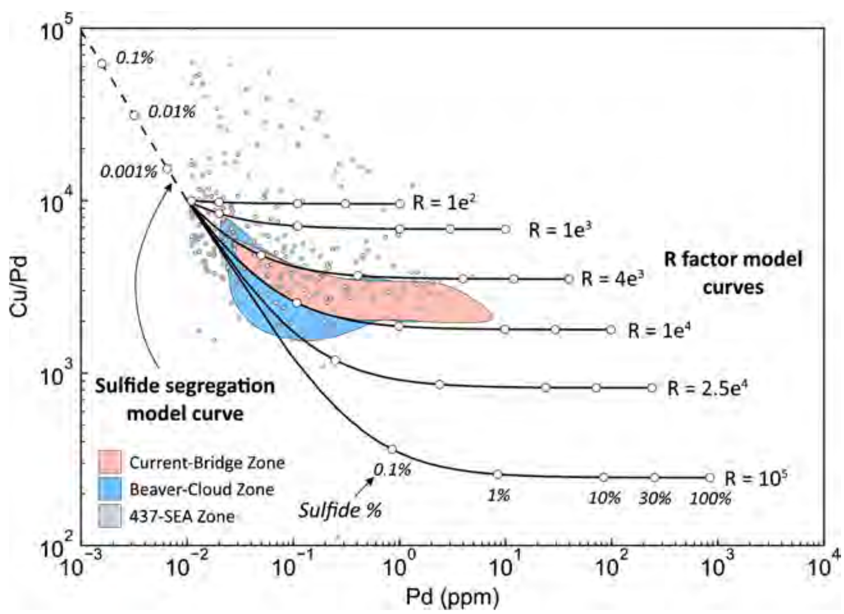

Fig. 11 Binary diagram illustrating the variation in bulk-rock Cu/Pd and Pd in the Current deposit. The colored fields represent the distribution of data for the Current–Bridge and Beaver–Cloud zones, whereas the data points represent the 437–SEA Zone. The solid curves represent modeled variations as a function of R factor and sulfide abundance. The dashed curve represents modeled variations as a function of sulfide liquid removal. The Cu–Pd contents of the starting melt and the sulfide liquid–silicate melt partition coefficients are provided in Table 1. The numbers on the curve represent sulfide percent, either as the amount present in the rock (in the case of the R factor models) or the amount of sulfide liquid removed (in the case of the sulfide segregation model)

The MIF signal recorded by some BMS in the Current–Bridge and Beaver–Cloud zones (Fig. 10C), therefore, likely originated from the addition of S with elevated $\Delta^{33}S$ from Archean rocks at depth. In contrast, the mantle-like $\Delta^{33}S$ and elevated S/Se values that largely characterize BMS in the 437–SEA Zone likely record assimilation of S from the local metasedimentary country rocks, which exhibit similar geochemical–isotopic signatures (Fig. 10C). This is consistent with the fact that the 437–SEA Zone was one of the final zones to have remained magmatically active in the Current intrusion, as evidenced by the lithologic layering in this zone that could only have been developed as a result of relatively closed-system fractional crystallization when the magmatic system was waning (ESM 1 Fig. S1) (Heggie et al. 2015). This portion of the conduit would, therefore, have experienced the greatest contact time with the metasedimentary country rocks, increasing the amount of metasedimentary S that was added to the magma.

An implication of this interpretation is that the sulfide liquid formed at depth and was carried upwards, the possibility of which has long been questioned (Lesher 2019). Recent numerical simulations and textural evidence, however, demonstrate that dense sulfide liquids may be transported upwards by attachment to vapor bubbles in shallow, degassing magmas (Yao et al. 2019; Yao and Mungall 2020). Barnes et al. (2019) demonstrated this concept for the Norilsk ores, where they identified segregated sulfide globules capped by highly fractionated, residual silicate melt (i.e., sulfide liquid + vapor bubble). A similar textural variety of sulfide occurs at Current (Fig. 5D), suggesting that the Current magma(s) were degassing during transport, which may have supported the upward movement of sulfide liquid.

Remobilization of metals

The peridotite host rocks of the Current deposit are pervasively serpentinized. This, along with several lines of mineralogical and geochemical evidence, support the idea that late-stage hydrothermal fluids circulated through the host rocks of the deposit. This evidence includes i) the ubiquity of secondary pyrite and millerite after pyrrhotite and pentlandite, respectively (Fig. 5H–J, L), ii) the occurrence of pyrrhotite and pentlandite veinlets that crosscut secondary pyrite (Fig. 5G), iii) the presence of chalcopyrite restricted to patches of late-stage hydrous minerals (Fig. 5J), iv) the lack of correlation between bulk-rock S and base–precious metals (e.g., Cu and Pd) for a subpopulation of samples from the deposit (Fig. 4A, B), and v) the occurrence of gersdorffite with pyrite (Fig. 5N). Although gersdorffite can crystallize from sulfide liquids (Hem and Makovicky 2004), the generally low As content of the primary BMS at Current (Fig. 7J, ESM 2 Table S3) suggests that the As content of the original sulfide liquid was low, precluding the possibility of gersdorffite being a magmatic phase. Such a low As content in BMS is consistent with the fact that As is often undersaturated in sulfide liquid unless it was added to the silicate magma via assimilation of an As-rich contaminant (Smith et al. 2021).

Given the presence of pyrite after pyrrhotite (Fig. 5H) and millerite after pentlandite (Fig. 5L), it is clear that at least some amount of Fe and Ni must have been remobilized since pyrrhotite has a higher Fe content than pyrite (~ 62 wt. % vs. ~ 47 wt. %), and pentlandite has a lower Ni and higher Fe content than millerite (~ 34 wt. % vs. ~ 65 wt. % Ni and ~ 33 wt. % vs. 0 wt. % Fe). The replacement of pyrrhotite by pyrite and pentlandite by millerite would, therefore, release Fe to the fluid, whereas the latter reaction would sequester Ni from the fluid; although the source of this additional Ni is uncertain, it could have originated from the olivine that was pervasively serpentinized, as has been demonstrated in the serpentinized Huangshandong Ni–Cu sulfide deposit in northwestern China (Wang et al. 2021). Mobilization of Fe and Ni is also consistent with the occurrence of pyrrhotite and pentlandite veinlets that crosscut pyrite (Fig. 5G), implying that this textural variety of pyrrhotite and pentlandite must have crystallized from fluids that circulated after the replacement of primary pyrrhotite by pyrite, as well as the occurrence of gersdorffite (Fig. 5N). Although removal of Fe can sufficiently explain the replacement of pyrrhotite by pyrite, it is likely that S was also added during this reaction. This is evident by the lack of correlation between bulk-rock S and metals in some samples from the Current deposit (Fig. 4A, B), indicating that S was likely mobile.

Considering that pyrite has a relatively invariable S content of ~ 53 wt. % and the Se content of pyrrhotite exhibits relatively limited variability (50–223 ppm), the large range in S/Se values exhibited by pyrite (Fig. 8B) cannot be entirely the result of S addition during pyrrhotite replacement as this would result in a maximum S/Se value in pyrite of 10,600 (530,000 ppm S / 50 ppm Se), whereas pyrite in the Current deposit exhibits values as high as 64,000 (Fig. 8B). Accordingly, some Se must have been released from pyrrhotite to the fluid as it was replaced by pyrite; this is consistent with the greater range in Se content of pyrite that extends to notably lower values (as low as 23 ppm) than the majority of pyrrhotite (Fig. 7L). Given that Se is thought to be most mobile in acidic, saline, and oxidizing fluids (Prichard et al. 2013), this implies that the fluids that reacted with and replaced pyrrhotite and pentlandite by pyrite and millerite, respectively, had low pH, high salinity, and high fO_2. Importantly, these are also conditions under which several metals may be mobilized, including some of the PGE (Mountain and Wood 1988; Pan and Wood 1994; Wood 2002; Hanley et al. 2005; Liu and McPhail 2005), although recent studies suggest these strict conditions may not be a requirement for metal mobilization (Sullivan et al. 2022).

Despite favorable fluid conditions for the mobility of the PPGE, the range of concentrations of Pd and Pt, as well as Au, in pyrrhotite and pyrite are largely indistinguishable, implying that the replacement reaction did not add or remobilize these metals (Fig. 7B–D). This is consistent with the positive correlations between bulk-rock Pd–Pt (Fig. 4C) and Pd–Ir (Fig. 4D). The IPGE (Ir, Os, and Ru) extend to lower concentrations in pyrite compared to pyrrhotite (Fig. 7E–G). Although these lower concentrations may result from IPGE remobilization by a hydrothermal fluid, large-scale remobilization seems unlikely given that the IPGE are generally considered immobile relative to, for example, Pd (Xiong and Wood 2000; Wood 2002; Sullivan et al. 2022). Given the lower concentrations of Sn and Bi in pyrite compared to pyrrhotite, it is likely that the lower IPGE content in pyrite relates to the formation of IPGE–Sn–Bi–Pb-bearing PGM, which are heterogeneously distributed throughout pyrite, as well as other BMS (ESM 1 Fig. S2) and were excluded from integration regions when processing laser ablation spectra. The higher As content of pyrite relative to pyrrhotite (Fig. 7J) suggests that As was added to the system by the hydrothermal fluid that replaced pyrrhotite by pyrite. This is consistent with the presence of gersdorffite (Fig. 5N) and the mobility of As in Ni–Cu–PGE deposits (Gervilla and Kojonen 2002; Le Vaillant et al. 2015, 2016). Similarly, the concentration of Co extends to notably higher values in pyrite relative to pyrrhotite, suggesting that it was also added to the mineralizing system (Fig. 7A). Given that Ag does not generally occur as an independent mineral (apart from electrum), its lower concentration in pyrite relative to pyrrhotite (Fig. 7H) suggests that it was remobilized from the BMS assemblage during replacement of pyrrhotite by pyrite.

Although not related to the replacement of pyrrhotite by pyrite, Cu was also likely remobilized given i) the occurrence of some chalcopyrite within hydrous mineral assemblages (Fig. 5J) (cf. Brzozowski et al. 2020) and ii) the lack of correlation between bulk-rock Cu and S in a subpopulation of samples from the Current deposit (Fig. 4A). This Cu could not have been added to the system, however, as such a process would generate a vertical trend in bulk-rock Cu/Pd vs. Pd space, which is not observed (Fig. 11). Rather, it must have been remobilized within the system.

These results have important implications for the Current deposit because they demonstrate that metals were variably mobilized by late-stage hydrothermal processes. At the deposit scale, the tenors of Cu and Pd were not affected by this event, as is evident by their coherent behavior in Cu/Pd vs. Pd space (Fig. 11). The IPGE tenors were also unaffected by this event, but their hosts were modified, with As-bearing IPGM becoming a host as a result late-stage As addition. The Ni and Co tenors of the deposit were likely improved during hydrothermal circulation given the presence of millerite after pentlandite, the latter of which has a higher Ni content, and the higher concentration of Co in pyrite after pyrrhotite. In contrast, the Ag tenor of the deposit was likely reduced by removal from the mineralizing system as evidenced by its lower concentration in pyrite after pyrrhotite.

Feeder zone and direction of magma flow

The direction of magma flow, and hence the location of the magma feeder zone, remain topics of contention in the Current deposit, with both SE to NW magma flow and NW to SE magma flow both being suggested (Bleeker et al. 2020). Three physicochemically distinct features of the SEA point towards a model whereby magma flow in the Current intrusion was from SE to NW, suggesting that the SEA could have been the feeder zone to the intrusion.

Loss of sulfide liquid

The SEA is the only zone in the Current intrusion to be characterized by Cu/Pd values that are elevated relative to mantle values (Fig. 10A, B), indicating that it is the only zone to have crystallized from Pd-depleted magma that lost sulfide liquid after it had equilibrated with the silicate magma and scavenged metals (Figs. 10 and 11). Given this, and the fact that bulk-rock Cu/Pd ratios throughout the Current deposit show relatively limited variability (Fig. 11), this loss of sulfide liquid was likely a local event, which we suggest is the removal of sulfide liquid via drainage down towards deeper portions of the intrusive system below the SEA. This suggestion is consistent with the lower Pd contents of pentlandite in this zone compared to pentlandite in the other zones of the deposit (ESM 2 Table S3). Such backflow of sulfide liquid towards deeper portions of an intrusive system has been described by Barnes et al. (2015a). Additionally, Pd depletion is also a feature of the feeder zone to the Marathon conduit-type magmatic sulfide deposit (Good et al. 2015). Loss of sulfide liquid requires this region of the deposit to have experienced a period of decreased magmatic activity, otherwise the sulfide liquid would likely have remained in suspension, resulting in mineralization that was similar to the other portions of the Current deposit, with no Pd depletion, but this is not observed. A decrease in magmatic activity would have allowed for more efficient settling of sulfide liquid droplets or percolation of sulfide liquid through pore spaces between silicate minerals, promoting the removal of sulfide liquid from the SEA. In the case of percolation, it was demonstrated by Mungall and Su (2005) that a sulfide liquid would not be capable of percolating through a cumulate pile by capillary forces, but could be forced through pore spaces by the flow of the enclosing silicate melt. Accordingly, if magmatic activity in the SEA decreased, backflow of the magma could have forced the sulfide liquid through grain boundaries, allowing it to percolate through the cumulate pile and to be removed from the SEA. Additionally, maintaining this Pd-depleted signature in the magma from which the SEA crystallized suggests that, after sulfide loss, the metal content of the mineralizing system was not replenished by significant influx of more primitive magma. Together, these metal characteristics require that the Current deposit crystallized in stages, with the SEA crystallizing last. In such a scenario, the SEA would have acted as a relatively independent system in its final stages prior to crystallization, allowing the magma and sulfide liquid in this zone to acquire distinct geochemical signatures resulting from loss of sulfide liquid via gravity drainage, potentially down the feeder zone. An alternative possibility to explain the Pd depletion in the SEA is retention of sulfide liquid in traps at depth. This scenario seems unlikely, however, because these traps would have been upstream of the deposit, resulting in Pd depletion in all of the zones of the Current deposit, which is not observed (Figs. 10 and 11).

Progressive crystallization from northwest to southeast could explain the recrystallized pyrrhotite observed throughout the Current intrusion (Fig. 5F). Deformation could not have caused this recrystallization because the intrusion is undeformed (Kuntz et al. 2022). An alternative explanation for the recrystallization is thermal metamorphism (Good et al. 2015). This would have required two features — i) some portions of the Current intrusion would need to have been significantly crystallized as pyrrhotite must have already been present and it recrystallizes from MSS at temperatures of < 650 °C (Kullerud et al. 1969; Kelly and Vaughan 1983; Ebel and Naldrett 1996; Lusk and Bray 2002), and ii) there must have been a sustained source of heat. Both of these requirements would have been satisfied in the progressive crystallization scenario, with the still magmatically active 437–SEA Zone providing the necessary heat. This direction of progressive crystallization is also consistent with changes in the morphology of the intrusion, with the shallower and thinner Current–Bridge Zone likely having begun crystallizing prior to the deeper and thicker Beaver–Cloud and 437–SEA zones (Figs. 2 and 3).

An alternative possibility to explain the Pd-depleted nature of the SEA is equilibration of the Current magma, flowing from northwest to southeast, with sulfide liquid. If such a scenario were true, then one would expect a systematic depletion in Pd from Current–Bridge to Beaver–Cloud to SEA, but this is not observed (Figs. 10 and 11). Additionally, it is difficult to conceive of a scenario whereby the Current pluton would have intruded from shallower depths (in the northwest) to greater depths (in the southeast). Although magma may migrate along weaknesses in the crust and be emplaced laterally, magma flow is principally upwards, driven by buoyancy and pressure forces (Longo et al. 2023). Given that the Southeast Anomaly occurs at a depth of ~ 1000 m and the Current–Bridge Zone occurs at a depth of ~ 50 m (Fig. 2b), it seems more likely for magma to have flowed from southeast upwards towards the northwest.

Local source of S

Base-metal sulfides in the SEA record distinct S isotope signatures compared to BMS in the other zones of the deposit, having $\Delta^{33}S$ values that are largely within the range of mantle values compared to the $\Delta^{33}S$ values that are higher than mantle in the other zones (Fig. 10). This indicates that the sources of S that contributed to sulfide saturation in the SEA were different than those which contributed to saturation in the Current–Bridge and Beaver–Cloud zones. Specifically, the magmas from which the latter zones crystallized likely became sulfide saturated by addition of S from a source at depth, whereas S from the local metasedimentary country rocks was also added to the magma from which the SEA crystallized (Fig. 10c). Addition of local S to the magma from which the SEA crystallized, and the lack of evidence for this addition elsewhere in the Current intrusion, can be explained by increased contact time between the SEA magma and the country rock, which would have allowed for greater diffusive transfer of S into the SEA magma (Robertson et al. 2015a; Barnes and Robertson 2019). Although local S addition could also have occurred via bulk assimilation as a result of, for example, erosion of the conduit floor, this seems unlikely as there is no evidence of bulk-rock contamination: i) partially assimilated xenoliths of country rock material are not observed in the SEA, ii) addition of significant amounts of siliceous country rock material would have resulted in the crystallization of orthopyroxene, but orthopyroxene is rare at Current, and iii) rocks throughout the Current intrusion, including the SEA, have Th/La ratios that are systematically lower than mantle values (0.07–0.1; Chaffee 2015; Yahia et al. 2022). Local addition of S only in the SEA implies that the flow of the SEA magma was restricted to the southeast portion of the Current intrusion, which is hosted by metasedimentary country rock, and/or that the magma was relatively stagnant in this area. It is likely that both scenarios occurred for two reasons. First, sequential crystallization of the Current intrusion from northwest to southeast would have progressively isolated the SEA from the other portions of the conduit, restricting magma flow to portions of the conduit hosted by metasedimentary country rock. Second, the Pd-depleted nature of the SEA (i.e., high Cu/Pd ratios) requires that the magma from which it crystallized lost sulfide liquid, which requires the SEA to have experienced a period of decreased magmatic activity that would have promoted gravitational settling. This decreased magmatic activity would have allowed the SEA magma to stagnate in contact with the metasedimentary country rock. Considering that the Pd content of pentlandite is lower in the SEA compared to the other zones in the Current deposit (ESM 2 Table S3), it is likely that this local addition of S triggered a separate sulfide saturation event in the SEA magma during and/or after the removal of earlier-formed sulfide liquid. The removal of earlier-formed sulfide liquid would have depleted the magma in Pd, as well as other metals, as demonstrated by the Rayleigh fractionation model in Figs. 10 and 11, such that the locally formed sulfide liquid was depleted in Pd, now recorded as Pd-depleted pentlandite.

Lithological layering

The above geochemical–isotopic characteristics that are unique to the SEA (elevated bulk-rock Cu/Pd, elevated S/Se ratios in sulfides, and mantle-like $\Delta^{33}S$ values in sulfides) suggest that this zone was potentially the final portion of the Current conduit to have crystallized. This interpretation is supported by the lithologic layering and accompanied changes in major–minor-element chemistry along drillhole that is observed only in this zone (Heggie et al. 2015). From base to top, this layering comprises peridotite, melagabbro, upper oxide gabbro, and quartz-bearing gabbro/monzonite, and is accompanied by systematic decreases in MgO–Cr and increases in Al_2O_3 up drillhole (ESM 1 Fig. S1). Such layering in the SEA, which is also observed in other conduit-type systems (e.g., Kabanga, Uitkomst, Eastern Gabbro; Gauert et al. 1995; Li et al. 2002; Maier et al. 2011; Cao et al. 2019), could have formed via closed-system fractional crystallization (Heggie et al. 2015) or open-system processes, such as slumping and saltation. Although it is difficult to distinguish between closed- vs. open-system processes with the available data, we suggest that the layering was the result of essentially closed-system processes for three reasons. First, the systematic changes in major–minor-element chemistry from the peridotite to the quartz-bearing gabbro/monzonite mimic the geochemical variation expected during fractionation of a magma. Second, there is a lack of rhythmic layering in the SEA, which may be expected if the layering formed by repeated magma replenishment followed by crystallization on the wall rock and collapse (Shaw 1997). Lastly, there is no evidence in drill core for folding of the lithologic layers, which may be expected if the layering formed as a result of slumping (Shaw 1997). We, therefore, suggest that the series of rock types that make up the SEA were the result of magmatic fractionation. This process occurred once the energy of the magmatic system waned and the conduit was no longer being replenished by magma.

Taken together, i) the Pd-depleted nature of the magma from which the SEA crystallized, ii) the distinct source of S that contributed to sulfide saturation in this zone, and iii) the lithological layering observed in this zone indicate that the SEA was the final zone to have crystallized and is, therefore, the feeder to the Current intrusion. This indicates that magma flow in the Current intrusion was from southeast to northwest.

Deposit model for the Current Ni–Cu–PGE system

We have developed a holistic mineral deposit model for the Current Ni–Cu–PGE deposit that incorporates the mineralogical–geochemical–isotopic features characterized here with the physical features of the intrusion. This model highlights the key mineralizing processes that operated throughout the intrusion to generate the mineralization, as well as how these processes changed as the mineralizing system evolved. Consider a shallow-dipping conduit that was emplaced at shallow levels into Archean metasedimentary and granitic country rocks. During the early, high-energy stage of system development, the conduit was charged with multiple pulses of olivine- and sulfide-laden magma (Fig. 12A). The sulfide liquid carried into the conduit formed at depth by the addition of S from Archean rocks and was entrained upwards, perhaps facilitated by the presence of vapor bubbles (Fig. 5C), and was initially characterized by elevated S/Se and $\Delta^{33}S$ (up to 3‰) values. During intervals of magmatic quiescence, the magma flowed down the conduit, carrying with it some of the olivine and sulfide liquid that it introduced (Fig. 12A). This process of influx and backflow could have generated eddy currents, aiding the entrained sulfide liquid in interacting with silicate melt (Fig. 12A). The high R factors (> 1,000) achieved would have largely diluted the geochemical (S/Se)–isotopic ($\Delta^{33}S$) signatures of the assimilated Archean S, such that most of the sulfide liquid would have been characterized by mantle-like signatures, apart from those that interacted with lower volumes of silicate melt.

During the low-energy stage of conduit development when the magmatic system was beginning to wane, the thinner morphology and/or shallow emplacement of the Current–Bridge and Beaver–Cloud zones promoted their early and rapid crystallization, closing them off to further magmatic activity (Fig. 12B). These regions of the conduit are characterized by high R factor, Pd-rich sulfides. The SEA was still magmatically active during this stage, allowing the composition of the resident magma and sulfide liquid to be further modified by magmatic processes. Restriction of magma flow to the portion of the conduit hosted by metasedimentary country rock, and its eventual stagnation in this area, allowed local S to be added to the magma,

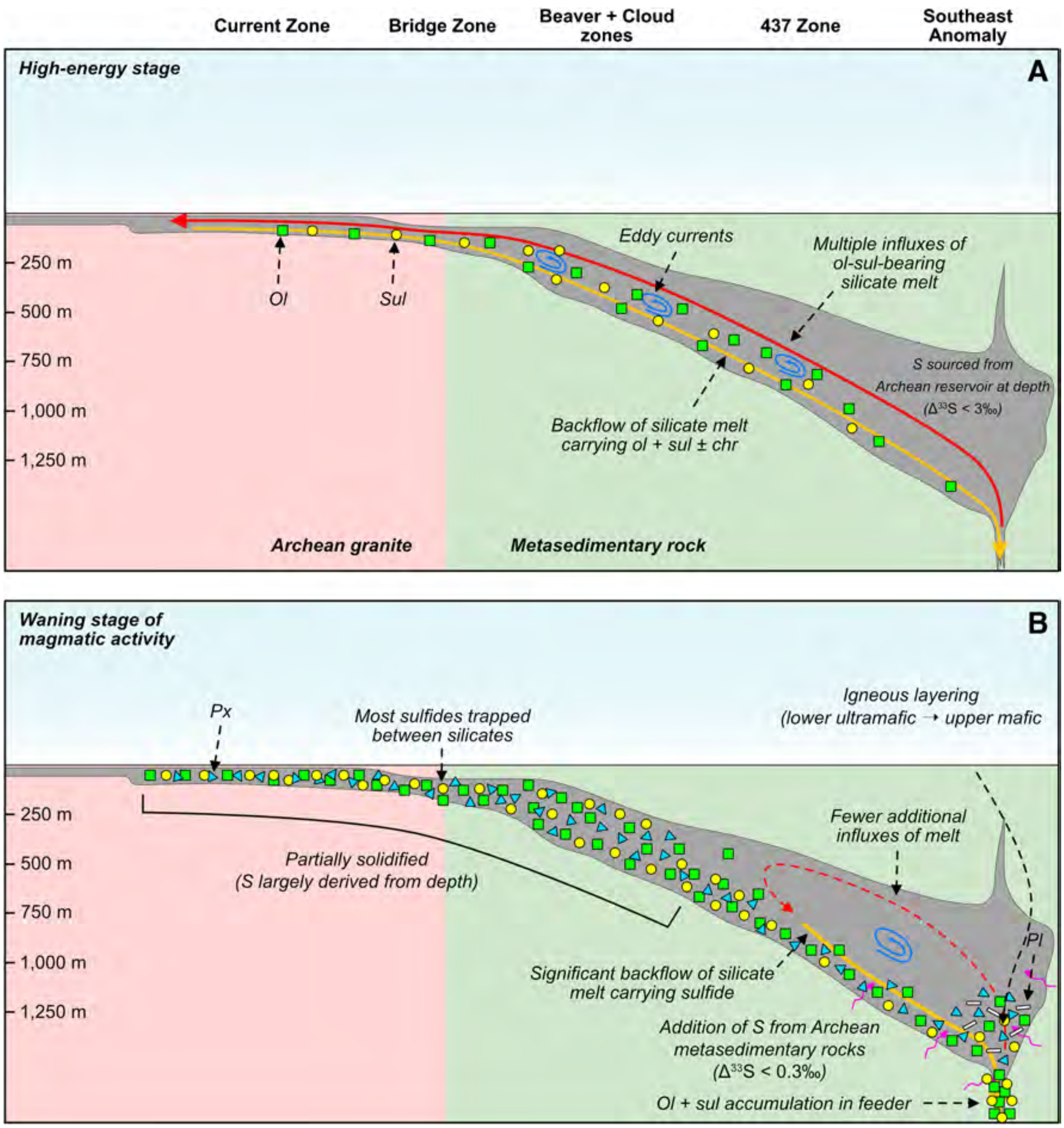

Fig. 12 Two-stage schematic model illustrating the processes that led to the formation of sulfide liquid and its subsequent enrichment in metals in the Current deposit — (**A**) high-energy stage and (**B**) waning stage of magmatic activity

generating additional sulfide liquid with distinct S isotope compositions. During periods of magmatic quiescence, olivine, clinopyroxene, and sulfide liquid drained down the conduit and, potentially, accumulated in the feeder zone, decreasing the sulfide abundance and Pd content of the SEA (Fig. 12B). The eventual cessation of the magmatic system allowed the magma in the SEA to evolve via essentially closed-system fractional crystallization, generating the systematic change in lithology from primitive to more evolved rocks up stratigraphy (Fig. 12B). After crystallization, circulation of hydrothermal fluids altered the host rocks and mineralization, which remobilized some of the metals.

Comparison to the architecture of other Ni–Cu–PGE deposits

Intrusions can exhibit a range of geometries, including channelized subvolcanic sills (e.g., Norilsk, Russia and Uitkomst, South Africa; Gauert et al. 1995; Naldrett and Lightfoot 1999; Maier et al. 2004), tube-like conduits (e.g., Nebo Babel, Australia and Limoiera, Brazil; Seat et al. 2007;

Mota-e-Silva et al. 2013), and feeder dikes that link vertically separated sills (e.g., Voisey's Bay, Canada; Evans-Lamswood et al. 2000). Although the Current deposit is classified as a conduit-type intrusion, its architecture falls into multiple of the aforementioned intrusion geometries depending on the location within the mineralized system. Specifically, the granite-hosted Current–Bridge Zone is characterized by a tube-like geometry similar to Nebo Babel, Limoiera, and Uitkomst, whereas the sedimentary-hosted Beaver–Cloud and 437–SEA zones have more ribbon-like geometries, being notably wider than they are thick, similar to Norilsk (Figs. 2 and 3). This change in geometry occurs abruptly at the contact between the rheologically distinct granite and sedimentary country rocks (Figs. 2 and 3). Although it is known that crustal-scale weaknesses exhibit fundamental controls on magma migration and intrusion geometry, the Current intrusion is one of few magmatic systems in which this is unambiguously demonstrated. This contrasts with Nebo Babel, Limoiera, and Uitkomst, which intruded into either intrusive or sedimentary country rock and exhibit comparatively invariable geometries along their lengths (Maier et al. 2004; Seat et al. 2007; Mota-e-Silva et al. 2013). One peculiarity of the geometry of the Current intrusion is that, unlike most magmatic intrusions, it thickens towards the feeder zone (Fig. 2). Considering that both the Beaver–Cloud Zone and SEA coincide with the Quetico and Escape Lake fault zones, respectively, and both zones are thick relative to the Current–Bridge Zone (Fig. 2), it is suggested that this thickening resulted from exploitation of a crustal weakness. The Current intrusion, therefore, serves as a prime example of how country rock rheology and crustal weakness control intrusion architecture.

Conclusions

The Current deposit represents one of the best examples of a conduit-type Ni–Cu–PGE sulfide deposit. This tube-shaped intrusion was emplaced into Archean metasedimentary and granitic rocks, and records a variety of magmatic and post-magmatic processes in the texture, and trace-element and S isotope composition of its diverse BMS assemblage.

1. Saturation of the Current magmas in sulfide and generation of a sulfide liquid resulted from addition of external S from at least two sources, one located at depth ($\Delta^{33}S < 3‰$) and the other being the local Archean metasedimentary country rocks ($\Delta^{33}S < 0.3‰$).
2. The Current intrusion crystallized sequentially, from the Current–Bridge Zone towards the 437–SEA Zone. This, along with the elevated Cu/Pd ratios, distinct source of S, and igneous layering in the 437–SEA Zone, suggests that it represents the feeder channel to the Current deposit.
3. The BMS mineralogy was modified by the circulation of hydrothermal fluids through the rocks, with pyrrhotite being replaced by pyrite and pentlandite being replaced by millerite. This fluid activity mobilized several metals and semi-metals, including Fe, Ni, S, Se, Co, Cu, As, and Ag, but did not affect the PGE.

Supplementary Information The online version contains supplementary material available at https://doi.org/10.1007/s00126-023-01193-9.

Acknowledgements The authors would like to thank Clean Air Metals Inc. for providing access to their geochemical database and core yard for sampling, and for allowing us to publish this study. The authors would also like to thank Georges Beaudoin, Wolfgang Maier, William Smith, and David Holwell for their constructive comments that helped fine-tune and strengthen the manuscript. We would like to thank J. C. Barrette (University of Windsor), Dr. Guosheng Wu (Lakehead University), and Dr. Laure Martin and Matvei Aleshin (University of Western Australia) for their contributions in obtaining analytical data. Lastly, we would like to acknowledge Connor Caglioti, Khalid Yahia, and Andrea Corredor Bravo (Lakehead University) for their continued discussions on the petrogenesis of the Thunder Bay North Intrusive Complex.

Funding This project was funded by a NSERC Alliance Grant (Grant No. ALLRP 551989—20) to Dr. Peter Hollings, and supported with in-kind contributions from Clean Air Metals Inc.

Declarations

Conflicts of interest There are no conflicts of interest associated with this study.

References

Barnes S-J, Gomwe TS (2011) The Pd deposits of the Lac des Iles Complex, Northwestern Ontario. Econ Geol 17:351–370

Barnes SJ, Robertson JC (2019) Time scales and length scales in magma flow pathways and the origin of magmatic Ni–Cu–PGE ore deposits. Geosci Front 10:77–87

Barnes S-J, Couture J-F, Sawyer EW, Bouchaib C (1993) Nickel-copper occurrences in the belleterre-angliers belt of the pontiac subprovince and the use of Cu-Pd ratios in interpreting platinum-group element distributions. Econ Geol 88:1402–1418

Barnes SJ, Godel BM, Locmelis M, Fiorentini ML, Ryan CG (2011) Extremely Ni-rich Fe–Ni sulfide assemblages in komatiitic dunite at Betheno, Western Australia: results from synchrotron X-ray fluorescence mapping. Aust J Earth Sci 58:691–709

Barnes SJ, Cruden AR, Arndt N, Saumur BM (2015a) The mineral system approach applied to magmatic Ni-Cu-PGE sulphide deposits. Ore Geol Rev 76:296–316

Barnes SJ, Mungall JE, Maier WD (2015b) Platinum group elements in mantle melts and mantle samples. Lithos 232:395–417

Barnes SJ, Ripley EM (2016) Highly siderophile and strongly chalcophile elements in magmatic ore deposits. Rev Mineral Geochem 81:725–774

Barnes SJ, Le Vaillant M, Godel B, Lesher CM (2019) Droplets and bubbles: solidification of sulphide-rich vapour-saturated orthocumulates in the Norilsk-Talnakh Ni–Cu–PGE Ore-bearing intrusions. J Petrol 60:269–300

Bekker A, Barley ME, Fiorentini ML, Rouxel OJ, Rumble D, Beresford SW (2009) Atmospheric sulfur in Archean komatiite-hosted nickel deposits. Science 326:1086–1089

Bleeker W, Smith J, Hamilton M, Kamo S, Liikane M, Hollings P, Cundari R, Easton M, Davis D (2020) The Midcontinent Rift and its mineral systems: overview and temporal constraints of Ni-Cu-PGE mineralized intrusions. Geological Survey of Canada, Canada

Brzozowski MJ, Samson IM, Gagnon JE, Good DJ, Linnen RL (2020) On the mechanisms for low-sulfide, high-platinum group element and high-sulfide, low-platinum group element mineralization in the eastern gabbro, Coldwell complex, Canada: evidence from textural associations, S/Se values, and platinum group element concentrations of base metal sulfides. Econ Geol 115:355–384

Brzozowski MJ, Good DJ, Wu C, Li W (2021) Cu isotope systematics of conduit-type Cu–PGE mineralization in the Eastern Gabbro, Coldwell Complex, Canada. Miner Deposita 56:707–724

Caglioti C (2023) PGE–Cu–Ni Sulfide Mineralization of the Mesoproterozoic Escape intrusion. MSc, Lakehead University, Northwestern Ontario

Cao Y, Good DJ, Linnen RL, Samson IM (2019) The role of magma injection and crystal sorting in the formation of early gabbros at the Coldwell Complex, Ontario. Canada. Can J Earth Sci 56(7):715–737

Chaffee MR (2015) Petrographic and Geochemical Study of the Hybrid Rock Unit Associated with the Current Lake Intrusive Complex. MSc, University of Minnesota

Craig JR (1973) Pyrite-pentlandite assemblages and other low temperature relations in the Fe-Ni-S system. Am J Sci 273-A:496–510

Craig JR, Kellurud G (1969) Phase relations in the Cu-Fe-Ni-S system and their application to magmatic ore deposits. Econ Geol Monogr 4:344–358

Cundari RM, Puumala MA, Smyk MC, Hollings P (2021) New and compiled whole-rock geochemical and isotope data of Midcontinent Rift-related rocks, Thunder Bay Area. Ontario Geological Survey, Canada

Dare SAS, Barnes S-J, Prichard HM, Fisher PC (2011) Chalcophile and platinum-group element (PGE) concentrations in the sulfide minerals from the McCreedy East deposit, Sudbury, Canada, and the origin of PGE in pyrite. Miner Deposita 46:381–407

Djon MLN, Barnes S-J (2012) Changes in sulfides and platinum-group minerals with the degree of alteration in the Roby, Twilight, and High Grade Zones of the Lac des Iles Complex, Ontario, Canada. Miner Deposita 47:875–896

Duran CJ, Barnes S-J, Corkery JT (2015) Chalcophile and platinum-group element distribution in pyrites from the sulfide-rich pods of the Lac des Iles Pd deposits, Western Ontario, Canada: implications for post-cumulus re-equilibration of the ore and the use of pyrite compositions in exploration. J Geochem Explor 158:223–242

Duran CJ, Barnes S-J, Corkery JT (2016) Trace element distribution in primary sulfides and Fe–Ti oxides from the sulfide-rich pods of the Lac des Iles Pd deposits, Western Ontario, Canada: constraints on processes controlling the composition of the ore and the use of pentlandite compositions in exploration. J Geochem Explor 166:45–63

Ebel DS, Naldrett AJ (1996) Fractional crystallization of sulfide ore liquids at high temperature. Econ Geol 91:607–621

Eckstrand OR, Hulbert LJ (1987) Selenium and the source of sulfur in magmatic nickel and platinum deposits. Geol Assoc Can-Mineral Assoc Can Program Abstr 12:40

Evans-Lamswood DM, Butt DP, Jackson RS, Lee DV, Muggridge MG, Wheeler RI (2000) Physical controls associated with the distribution of sulfides in the Voisey's Bay Ni-Cu-Co deposit. Labrador Econ Geol 95:22

Farquhar J (2002) Mass-independent sulfur of inclusions in diamond and sulfur recycling on early earth. Science 298:2369–2372

Farquhar J, Wing BA (2003) Multiple sulfur isotopes and the evolution of the atmosphere. Earth Planet Sci Lett 213:1–13

Farquhar J, Wu N, Canfield DE, Oduro H (2010) Connections between sulfur cycle evolution, sulfur isotopes, sediments, and base metal sulfide deposits. Econ Geol 105:509–533

Farquhar J, Wing BA (2005) The terrestrial record of stable sulphur isotopes: a review of the implications for evolution of Earth's sulphur cycle. In: McDonald I (ed) Mineral Deposits and Earth Evolution. Geological Society of London Special Publication, London, pp 167–177

Gauert CDK, De Waal SA, Wallmach T (1995) Geology of the ultrabasic to basic Uitkomst complex, eastern Transvaal, South Africa: an overview. J Afr Earth Sci 21:553–570

Gervilla F, Kojonen K (2002) The platinum-group minerals in the upper section of the Keivitsansarvi Ni-Cu-PGE deposit, northern Finland. Can Mineral 40:377–394

Good DJ, Epstein R, McLean K, Linnen R, Samson I (2015) Evolution of the main zone at the marathon Cu-PGE sulfide deposit, midcontinent rift, Canada: spatial relationships in a magma conduit setting. Econ Geol 110:983–1008

Hanley JJ, Pettke T, Mungall JE, Spooner ETC (2005) The solubility of platinum and gold in NaCl brines at 1.5 kbar, 600 to 800°C: A laser ablation ICP-MS pilot study of synthetic fluid inclusions. Geochim Cosmochim Acta 69:2593–2611

Hart TR, MacDonald CA (2007) Proterozoic and Archean geology of the Nipigon Embayment: implications for emplacement of the Mesoproterozoic Nipigon diabase sills and mafic to ultramafic intrusions. Can J Earth Sci 44:1021–1040

Heggie G (2012) 2012 Drill results and interpretations: part 2. Lone Island Lake area geochemistry. Thunder Bay, Ontario

Heggie G, Johnson J, MacTavish A (2015) Thunder Bay North Current Chonolith Field Trip. Thunder Bay, Ontario

Hem SR, Makovicky E (2004) The system Fe-Co-Ni-As_S. I. Phase relations in the (Fe Co, Ni)As0.5S1.5 section at 650C and 500C. Can Mineral 42:43–62

Hiebert RS, Bekker A, Wing BA, Rouxel OJ (2013) The Role of paragneiss assimilation in the origin of the Voisey's Bay Ni-Cu sulfide deposit, labrador: multiple S and Fe isotope evidence. Econ Geol 108:1459–1469

Hiebert RS, Bekker A, Houlé MG, Wing BA, Rouxel OJ (2016) Tracing sources of crustal contamination using multiple S and Fe isotopes in the Hart komatiite-associated Ni–Cu–PGE sulfide deposit, Abitibi greenstone belt, Ontario, Canada. Miner Deposita 51:919–935

Hinchey JG, Hattori KH (2005) Magmatic mineralization and hydrothermal enrichment of the High Grade Zone at the Lac des Iles palladium mine, northern Ontario, Canada. Miner Deposita 40:13–23

Holwell DA, Adeyemi Z, Ward LA, Smith DJ, Graham SD, McDonald I, Smith JW (2017) Low temperature alteration of magmatic Ni-Cu-PGE sulfides as a source for hydrothermal Ni and PGE ores: a quantitative approach using automated mineralogy. Ore Geol Rev 91:718–740
Kullerud G, Yund RA, Moh GH (1969) Phase relations in the Cu-Fe-S, Cu-Ni-S, and Fe-Ni-S systems. Econ Geol Monogr 4:323
Kelly DP, Vaughan DJ (1983) Pyrrhotine-pentlandite ore textures: a mechanistic approach. Mineral Mag 47:453–463
Kerr A (2003) Guidelines for the calculation and use of sulphide metal contents in research and mineral exploration. Newfoundland Department of Mines and Energy, Geological Survey. https://eurekamag.com/research/019/115/019115683.php
Kuntz G, Wissent B, Boyko K, Harkonen H, Jones L, Muir W, Buss B, Peacock B (2022) NI 43-101 Technical report and preliminary economic assessment for the Thunder Bay North Project, Thunder Bay, Ontario. Clean Air Metals Inc., Thunder Bay, ON, Canada
LaFlamme C, Martin L, Jeon H, Reddy SM, Selvaraja V, Caruso S, Bui TH, Roberts MP, Voute F, Hagemann S, Wacey D, Littman S, Wing B, Fiorentini M, Kilburn MR (2016) In situ multiple sulfur isotope analysis by SIMS of pyrite, chalcopyrite, pyrrhotite, and pentlandite to refine magmatic ore genetic models. Chem Geol 444:1–15
Lawley CJM, Petts DC, Jackson SE, Zagorevski A, Pearson DG, Kjarsgaard BA, Savard D, Tschirhart V (2020) Precious metal mobility during serpentinization and breakdown of base metal sulphide. Lithos 354–355:105278
Le Vaillant M, Barnes SJ, Fiorentini ML, Miller J, McCuaig TC, Muccilli P (2015) A hydrothermal Ni-As-PGE geochemical halo around the Miitel komatiite-hosted nickel sulfide deposit, Yilgarn Craton, Western Australia. Econ Geol 110:505–530
Le Vaillant M, Barnes SJ, Fiorentini ML, Santaguida F, Törmänen T (2016) Effects of hydrous alteration on the distribution of base metals and platinum group elements within the Kevitsa magmatic nickel sulphide deposit. Ore Geol Rev 72:128–148
Lehmann J, Arndt N, Windley B, Zhou M-F, Wang CY, Harris C (2007) Field relationships and geochemical constraints on the emplacement of the Jinchuan intrusion and its Ni-Cu-PGE sulfide deposit, Gansu, China. Econ Geol 102:75–94
Lesher CM (2019) Up, down, or sideways: emplacement of magmatic Fe–Ni–Cu–PGE sulfide melts in large igneous provinces. Can J Earth Sci 56:756–773
Lesher CM, Burnham OM (2001) Multicomponent elemental and isotopic mixing in Ni–Cu–(PGE) ores at Kambalda, Western Australia. Can Mineral 39:421–446
Li C, Ripley EM, Maier WD, Gomwe TES (2002) Olivine and sulfur isotopic compositions of the Uitkomst Ni–Cu sulfide ore-bearing complex, South Africa: evidence for sulfur contamination and multiple magma emplacements. Chem Geol 188:149–159
Liu W, McPhail DC (2005) Thermodynamic properties of copper chloride complexes and copper transport in magmatic-hydrothermal solutions. Chem Geol 221:21–39
Longo A, Garg D, Papale P, Montagna CP (2023) Dynamics of magma chamber replenishment under buoyancy and pressure forces. J Geophys Res Solid Earth 128:e2022JB025316
Lusk J, Bray DM (2002) Phase relations and the electrochemical determination of sulfur fugacity for selected reactions in the Cu–Fe–S and Fe–S systems at 1 bar and temperatures between 185 and 460 jC. Chem Geol 192:22
Maier WD, Gomwe T, Barnes S-J, Li C, Theart H (2004) Platinum group elements in the Uitkomst Complex, South Africa. Econ Geol 99:499–516
Maier WD, Barnes S-J, Ripley EM (2011) The Kabanga Ni sulfide deposits, Tanzania: a review of ore-forming processes. In: Magmatic Ni-Cu and PGE Deposits: Geology, Geochemistry, and Genesis. Society of Economic Geologists. https://doi.org/10.5382/Rev.17.09
Misra KC, Fleet ME (1974) Chemical composition and stability of violarite. Econ Geol 59:391–403
Mota-e-Silva J, Filho CFF, Giustina MESD (2013) The Limoeiro deposit: Ni-Cu-PGE sulfide mineralization hosted within an ultramafic tubular magma conduit in the Borborema Province, Northeastern Brazil. Econ Geol 108:1753–1771
Mountain BW, Wood SA (1988) Chemical controls on the solubility, transport, and deposition of platinum and palladium in hydrothermal solutions: a thermodynamic approach. Econ Geol 83:492–510
Mungall J, Su S (2005) Interfacial tension between magmatic sulfide and silicate liquids: constraints on kinetics of sulfide liquation and sulfide migration through silicate rocks. Earth Planet Sci Lett 234:135–149
Naldrett AJ (2010) From the mantle to the bank: The life of a Ni-Cu-(PGE) sulfide deposit. South Afr J Geol 113:1–32
Naldrett AJ, Kellurud G (1967) A study of the Strathcona mine and its bearing on the origin of the nickel-copper ores of the Sudbury District, Ontario. J Petrol 8:453–531
Naldrett AJ, Cragi JR, Kellurud G (1967) The central portion of the Fe-Ni-S system and its bearing on pentlandite exsolution in iron-nickel sulfide ores. Econ Geol 62:826–847
Naldrett AJ, Lightfoot PC (1999) Ni-Cu-PGE deposits of the Norilsk Region, Siberia: their formation in conduits for flood basalt volcanism. In: Keays RR, Lesher CM, Lightfoot PC, Farrow CEG (eds) Dynamic processes in magmatic ore deposits and their application in mineral exploration. Geological Association of Canada, Short Course Notes, pp 195–249
Palme H, O'Neil HStC (2014) Cosmochemical estimates of mantle composition. In: Holland HD, Turekian KK (eds) Treatise on Geochemistry, 2nd edn. Elsevier, pp 1–39. https://doi.org/10.1016/B0-08-043751-6/02177-0
Pan P, Wood SA (1994) Solubility of Pt and Pd sulfides and Au metal in aqueous bisulfide solutions. Miner Deposita 29:373–390
Piña R, Gervilla F, Barnes S-J, Oberthür T, Lunar R (2016) Platinum-group element concentrations in pyrite from the Main Sulfide Zone of the Great Dyke of Zimbabwe. Miner Deposita 51:853–872
Prichard HM, Knight RD, Fisher PC, McDonald I, Zhou M-F, Wang CY (2013) Distribution of platinum-group elements in magmatic and altered ores in the Jinchuan intrusion, China: an example of selenium remobilization by postmagmatic fluids. Miner Deposita 48:767–786
Queffurus M, Barnes S-J (2015) A review of sulfur to selenium ratios in magmatic nickel-copper and platinum-group element deposits. Ore Geol Rev 69:301–324
Ripley EM, Li C (2003) Sulfur isotope exchange and metal enrichment in the formation of magmatic Cu-Ni-(PGE) deposits. Econ Geol 98:635–641
Ripley EM, Li C (2013) Sulfide saturation in mafic magmas: is external sulfur required for magmatic Ni-Cu-(PGE) ore genesis? Econ Geol 108:45–58
Ripley EM, Li C, Shin D (2002) Paragneiss assimilation in the genesis of magmatic Ni-Cu-Co sulfide mineralization at Voisey's Bay, Labrador: δ34S, δ13C, and Se/S evidence. Econ Geol 97:1307–1318
Ripley EM, Taib NI, Li C, Moore CH (2007) Chemical and mineralogical heterogeneity in the basal zone of the Partridge River Intrusion: implications for the origin of Cu–Ni sulfide mineralization in the Duluth Complex, midcontinent rift system. Contrib Mineral Petrol 154:35
Ripley EM, Li C, Moore CH, Schmitt AK (2010) Micro-scale S isotope studies of the Kharaelakh intrusion, Noril'sk region, Siberia: Constraints on the genesis of coexisting anhydrite and sulfide minerals. Geochim Cosmochim Acta 74:634–644

Robertson J, Ripley EM, Barnes SJ, Li C (2015a) Sulfur liberation from country rocks and incorporation in mafic magmas. Econ Geol 110:1111–1123

Robertson JC, Barnes SJ, Le Vaillant M (2015b) Dynamics of magmatic sulphide droplets during transport in silicate melts and implications for magmatic sulphide ore formation. J Petrol 56:2445–2472

Seat Z, Beresford SW, Grguric BA, Waugh RS, Hronsky JMA, Gee MAM, Groves DI, Mathison CI (2007) Architecture and emplacement of the Nebo-Babel gabbronorite-hosted magmatic Ni–Cu–PGE sulphide deposit, West Musgrave, Western Australia. Miner Deposita 42:551–581

Shahabi Far M, Samson IM, Gagnon JE, Good DJ, Linnen RL, Layne GD, Wing BA (2018) Identifying externally derived sulfur in conduit-type Cu–platinum-group element deposits: the importance of multiple sulfur isotope studies. Geology 46:235–238

Shaw CSJ (1997) The petrology of the layered gabbro intrusion, eastern gabbro, Coldwell alkaline complex, Northwestern Ontario, Canada: evidence for multiple phases of intrusion in a ring dyke. Lithos 40:243–259

Smith JW, Holwell DA, McDonald I, Boyce AJ (2016) The application of S isotopes and S/Se ratios in determining ore-forming processes of magmatic Ni–Cu–PGE sulfide deposits: a cautionary case study from the northern Bushveld Complex. Ore Geol Rev 73:148–174

Smith WD, Maier WD, Bliss I, Martin L (2021) In situ multiple sulfur isotope and S/Se composition of magmatic sulfide occurrences in the Labrador Trough, Northern Quebec. Econ Geol 116:1669–1686

Sullivan NA, Zajacz Z, Brenan JM, Hinde JC, Tsay A, Yin Y (2022) The solubility of gold and palladium in magmatic brines: implications for PGE enrichment in mafic-ultramafic and porphyry environments. Geochim Cosmochim Acta 316:230–252

Thomas DG, Melnyk J, Gormely L, Searston S, Kulla G (2011) Magma metals limited Thunder Bay north polymetallic project Ontario, Canada. AMEC, Vancouver, BC

Wang S, Wu C, Muhtar MN, Lei R, Brzozowski MJ (2021) Mobilization of ore-forming metals during post-magmatic hydrothermal overprinting of the Huangshandong Ni–Cu sulfide deposit, Eastern Tianshan. NW China Ore Geol Rev 137:104315

Watkinson DH, Dunning G (1979) Geology and platinum-group mineralization, Lac-des-Iles Complex, northwestern Ontario. Can Mineral 17:453–462

Williams HR (1991) Quetico Subprovince. In: Geology of Ontario. Ontario Geological Survey, pp 383–404

Wood SA (2002) The aqueous geochemistry of the platinum-group elements with applications to ore deposits. In: Cabri LJ (ed) The geology, geochemistry, mineralogy and mineral beneficiation of platinum-group elements. Canadian Institute of Mining, Metallurgy and Petroleum, pp 211–249

Xiong Y, Wood SA (2000) Experimental quantification of hydrothermal solubility of platinum-group elements with special reference to porphyry copper environments. Mineral Petrol 68:1–28

Yahia K, Hollings P, Brzozowski MJ, MacTavish A, Heggie G, Drost A (2022) Geochemical and isotopic composition of Midcontinent Rift-related intrusions of the Thunder Bay North Igneous Complex, northwestern Ontario, Canada. In: Institute on Lake Superior Geology Proceedings, 68th Annual Meeting. pp 56–57

Yao Z, Mungall JE (2020) Flotation mechanism of sulphide melt on vapour bubbles in partially molten magmatic systems. Earth Planet Sci Lett 542:116298

Yao Z, Mungall JE, Qin K (2019) A preliminary model for the migration of sulfide droplets in a magmatic conduit and the significance of volatiles. J Petrol 60:2281–2316

Publisher's note Springer Nature remains neutral with regard to jurisdictional claims in published maps and institutional affiliations.

THE GEOLOGICAL SOCIETY OF AMERICA®

Petrogenetic relationship of the variably Ni–Cu–platinum-group element (PGE)-mineralized intrusions of the Thunder Bay North Intrusive Complex, Midcontinent Rift, Canada: Implications for mineral exploration in mafic–ultramafic complexes

Matthew J. Brzozowski[1,2,†], Pete Hollings[2], Mike Hamilton[3], Geoff Heggie[4], Connor Caglioti[2], Khalid Yahia[2], and Andrea Corredor Bravo[2]

[1]*Laboratory of Mineralization and Dynamics, School of Earth Science and Resources, Chang'an University, Xi'an, Shaanxi 710054, China*

[2]*Geology Department, Lakehead University, Thunder Bay, Ontario P7B 5E1, Canada*

[3]*Department of Earth Sciences, University of Toronto, Toronto, Ontario M5S 1A1, Canada*

[4]*Clean Air Metals, 1004 Alloy Drive, Thunder Bay, Ontario P7B 6A5, Canada*

ABSTRACT

The Thunder Bay North Intrusive Complex (TBNIC) of Canada comprises six variably Ni–Cu–platinum-group element (PGE)-mineralized mafic–ultramafic intrusions that intruded the Archean Quetico Subprovince. These are the Current, Escape, Lone Island, Greenwich, and 025 intrusions, with the former three aligned along an east–west-trending intrusion termed the East–West Corridor. These intrusions have a consistent igneous stratigraphy comprising, from bottom to top, peridotite, gabbros, and quartz gabbro. Only the Current and Escape intrusions are known to host sulfide mineralization in the peridotite. Despite the economic significance of the TBNIC, little work has been done to characterize its petrogenetic evolution and the causes of the apparent variable fertility. Our new ages for Escape (1107.6 ± 0.9 Ma) and Greenwich (1105.7 ± 0.9 Ma), combined with previously determined ages for Current (1106.6 ± 1.6 Ma) and Lone Island (1106.3 ± 2.1 Ma), demonstrate that the TBNIC was emplaced as part of the ca. 1.1 Ga Midcontinent Rift event. The similarities in their rare earth element geochemistry and consistently low Th/La–Sr_i values indicate that the intrusions crystallized from genetically related magmas that did not assimilate significant amounts of crustal material. Accordingly, their systematically negative εNd_t values and Nb anomalies likely reflect that their parent magmas were largely sourced from the subdcontinental lithospheric mantle and not the Keweenaw Plume. Given their genetic relationship, the variable fertility of the intrusions cannot be related to processes that occurred in their mantle sources. Since the gabbros have systematically depleted Cu/Zr–Cu/Pd ratios and the peridotites have enriched ratios, the apparent variable fertility is likely related to the timing and location of sulfide segregation and accumulation, with the barren gabbros preserving magmas that lost sulfide liquid during transport to shallow crustal levels, and the mineralized peridotites recording accumulation of sulfide liquid. This interpretation has important implications for exploration as it implies that sulfide mineralization in the apparently barren intrusions may be located at depth in undiscovered ultramafic cumulates.

Matthew J. Brzozowski https://orcid.org/0000-0003-4857-7127
†mjbrzozo@outlook.com

1. INTRODUCTION

The ca. 1.1 Ga North American Midcontinent Rift System (MRS) is a failed intra-cratonic rift that preserves >4,000,000 km^3 of magmatism as basalt sheets and flows (e.g., Coubran basalt, Wolfcamp basalt, and Osler Volcanic Group), mafic sills (e.g., Nipigon, McIntyre, Logan, Inspiration, Shillabeer, and Jackfish sills), mafic–ultramafic chonoliths (e.g., Seagull, Sunday Lake, Thunder, Eagle, Tamarack) and layered intrusions (e.g., Duluth Complex), and alkaline complexes (e.g., Coldwell Complex), all of which were emplaced over ~30 m.y. (Fig. 1) (Hutchinson et al., 1990; Cannon, 1992; Klewin and Shirey, 1992; Davis and Green, 1997; Bleeker et al., 2020; Woodruff et al., 2020). It has long been suggested that the magmas from which these rock suites crystallized originated from the partial melting of the Keweenaw Plume that impinged upon the crust beneath what is now Wisconsin, USA (Hutchinson et al., 1990; Nicholson and Shirey, 1990; Nicholson et al., 1997). Building on the work of Shirey et al. (1994) and Shirey (1997), which demonstrated significant contributions of subcontinental lithospheric mantle (SCLM) material to the basaltic packages of the MRS, Brzozowski et al. (2023b) demonstrated that several of the early mafic–ultramafic intrusions (i.e., Eva Kitto, Thunder, Seagull; Fig. 1) and sills (i.e., Shillabeer, Jackfish; Fig. 1) crystallized from melts that were derived largely from partial melting of an enriched SCLM, with variably minor contributions from the Keweenaw Plume and generally limited contributions from crustal material. Although the mineralogy, lithology, mineralization, and petrogenesis of many of these intrusions has been characterized, the petrogenetic evolution of the variably mineralized Thunder Bay North Intrusive Complex as a whole remains ambiguous (Brzozowski et al., 2023a; Caglioti, 2023), yet is one of only two mineralized systems in the northeast portion of the MRS that is of current economic significance (Ciuculescu

GSA Bulletin;
published online 30 October 2024

https://doi.org/10.1130/B37736.1.

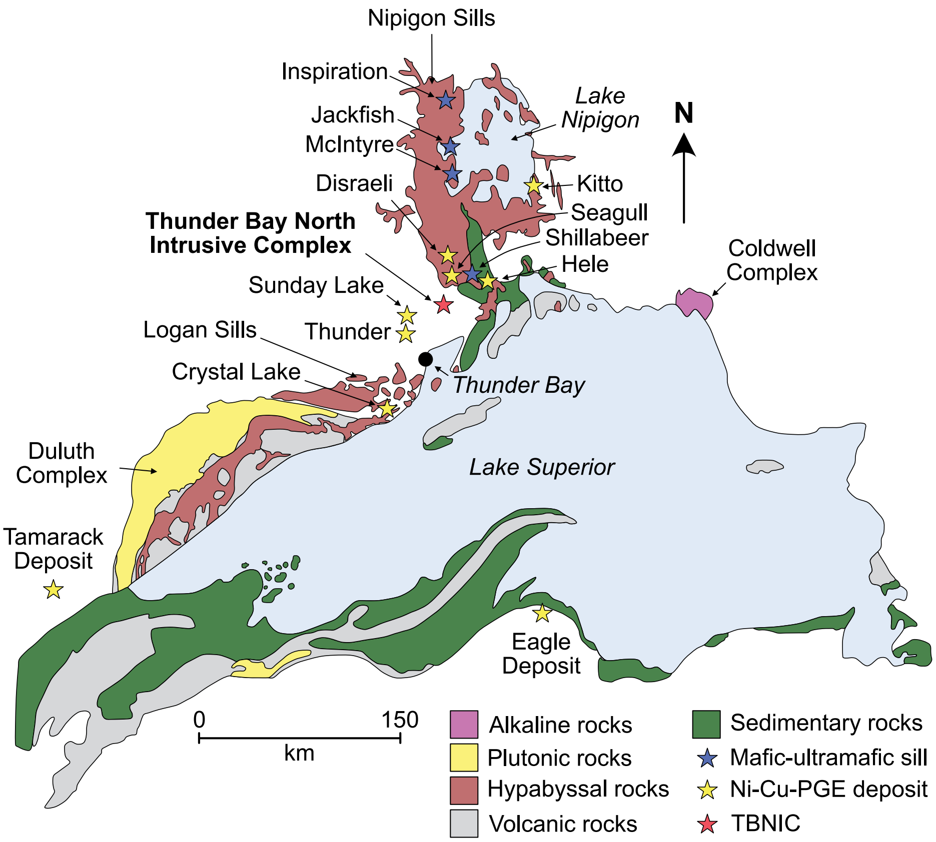

Figure 1. Geologic map of the North American Midcontinent Rift System showing the distribution of rock types and the locations of variably Ni–Cu–platinum-group element (PGE)-mineralized mafic–ultramafic intrusions and sills (modified from Good et al., 2015). TBNIC—Thunder Bay North Intrusive Complex (Canada).

et al., 2023), with the Eastern Gabbro of the Coldwell Complex being the other (Bradfield et al., 2020).

The Thunder Bay North Intrusive Complex (TBNIC) comprises a series of mafic–ultramafic intrusions that, from east to west, are termed Lone Island, Escape, 025, Current, and Greenwich (Fig. 2A) (Yahia, 2024). Some of these intrusions (Current, Escape, and Lone Island) appear to be connected by an east–west-trending structure that parallels the Escape Lake Fault and that contains thin mafic dikes that are here termed the East–West Corridor (Fig. 2A). Of the intrusions that comprise the TBNIC, only the Current and Escape host economic Ni–Cu–platinum-group element (PGE) sulfide mineralization in their ultramafic portions. In the MRS, there is an apparent relationship between SCLM-derived magmas and PGE-rich sulfide mineralization (Good et al., 2021; Brzozowski et al., 2022, 2023b). Additionally, the evolution of several mineralized and barren MRS-related rock suites was modified by assimilation of variable amounts of crustal material (e.g., Nipigon sills; Hollings et al., 2007a, 2007b; Brzozowski et al., 2023b). Considering the importance of source characteristics to the formation of economically significant magmatic sulfide deposits (Zhang et al., 2008; Richardson and Shirey, 2008; Maier and Groves, 2011; Zhao et al., 2024; Ezad et al., 2024a, 2024b), as well as derivation of externally derived S to achieving sulfide saturation (Ripley and Li, 2013), the occurrence of variably mineralized, spatiotemporally associated intrusions in the TBNIC raises several questions about its petrogenetic evolution. (1) Are the six intrusions genetically related? (2) Were the magmas from which these intrusions crystallized sourced from the Keweenaw Plume or the SCLM? (3) Were the magmas contaminated during transport and emplacement in the crust? (4) Why do only two of the six intrusions contain significant sulfide mineralization? (5) What is the relationship of the barren gabbroic rocks to the variably mineralized peridotites? To address these questions, we integrate field relationships with high-precision bulk-rock geochemical data, Rb–Sr and Sm–Nd isotopes, and geochronology of these intrusions. Clarifying these fundamental questions will not only help to develop robust exploration strategies in the TBNIC, but also advance our understanding of the evolution of the MRS and the formation of Ni–Cu–PGE-mineralized systems, and provide pathways to explore for additional mineralization in seemingly variably mineralized intrusive complexes.

2. GEOLOGY OF THE THUNDER BAY NORTH INTRUSIVE COMPLEX

The TBNIC comprises a total of six mafic–ultramafic intrusions that were emplaced into metasedimentary and granitic country rocks of the Quetico Subprovince (Fig. 2A) (Yahia, 2024). The Current, Escape, and Lone Island intrusions straddle the east–west-trending Quetico Fault and appear to be connected by the east–west-trending dikes-sills of the East–West Corridor, whereas the 025 and Greenwich intrusions occur to the northwest and northeast of the Current intrusion, respectively (Fig. 2A). To date, exploration efforts have focused on the Current and Escape intrusions as they host economically significant Ni–Cu–PGE sulfide mineralization in the form of the Current and Escape deposits. The morphology, lithology, and stratigraphy of these intrusions have, therefore, been characterized to a greater degree than the other intrusions.

The 1106.6 ± 1.6 Ma Current intrusion is an ∼5-km-long intrusion that trends in a northwest direction and dips shallowly from near surface in the northwest to a depth of >1000 m at the drill defined southeastern extent (Fig. 2B) (Chaffee, 2015; Bleeker et al., 2020). The morphology of the intrusion changes along its strike and is best described as a chonolith that progressively increases in cross-sectional area from NW to SE. The portion north of the Quetico Fault is tubular and relatively flat lying, whereas the portion south of the fault system is thicker, tabular, and dips toward the southeast at an angle of 10°–15° (Fig. 2B) (Brzozowski et al., 2023a). The chonolith has been broadly subdivided into three zones based on location: (1) the Current–Bridge Zone to the north (i.e., everything west of 357,900 m E), (2) the 437 Zone–Southeast Anomaly (SEA) to the south (i.e., everything east of 359,500 m E), and (3) the Beaver–Cloud Zone in between, the latter two being hosted by Quetico metasedimentary rock and the former being hosted by Quetico granitic rock (Fig. 2B). The 437 Zone–SEA portion of the chonolith contains the thickest package of rock, with in excess of 600 m of igneous stratigraphy comprising, from bottom to top, peridotite, feldspathic peridotite, olivine gabbro, oxide gabbro, gabbro, and quartz gab-

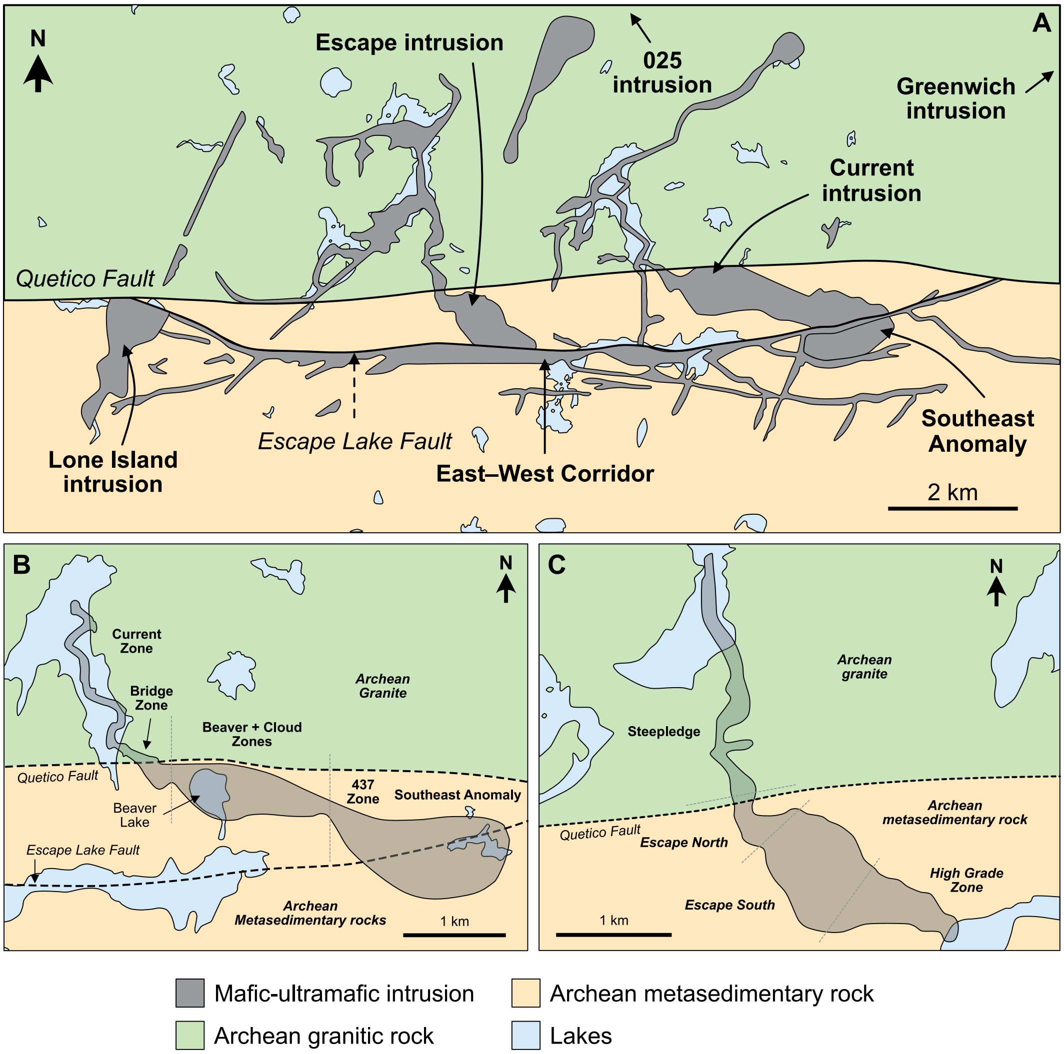

Figure 2. (A) Geologic map showing the locations of the mafic–ultramafic intrusions of the Thunder Bay North Intrusive Complex, Canada (modified from Thomas et al., 2011). The arrows for the 025 and Greenwich intrusions are pointing to the locations of these intrusions off the geological map. (B) Geologic map illustrating, in plan view, the shape of the Current intrusion and the locations of the various zones of mineralization (modified from Chaffee, 2015). (C) Geologic map illustrating, in plan view, the shape of the Escape intrusion and the locations of the various zones of mineralization (modified from Caglioti, 2023; Ciuculescu et al., 2023).

bro (Fig. S1[1]) (Heggie et al., 2015; Brzozowski et al., 2023a). The Beaver–Cloud and Current–Bridge zones that occur to the NW of the SEA comprise a stratigraphic profile dominated by the basal peridotite and feldspathic peridotite, with a gradual transition to overlying gabbro. The gabbro and quartz gabbro are volumetrically minor components of the stratigraphy of these zones of the chonolith. Xenoliths are common within the upper gabbro and quartz gabbro. Although some of these xenoliths are reflective of the Quetico granite and metasedimentary country rocks (Fig. S1), the most abundant are xenoliths of quartz, interpreted to be restites from quartz veins based on the occurrence of molybdenite along fractures (Heggie et al., 2015). Given their xenolith-rich nature, the upper gabbro and quartz gabbro are excluded from petrogenetic interpretations as their bulk-rock geochemical compositions are not representative of the magma from which they crystallized.

The Escape intrusion, which is located 3 km to the west of and runs parallels to the Current chonolith (Fig. 2A), has a down plunge extent of ~6.5 km long as defined by drilling and magnetic interpretation. Similarly, the intrusion has a chonolithic morphology, dips shallowly, and increases in cross-sectional profile to the southeast (Fig. 2C) (Caglioti, 2023). The chonolith has been subdivided into four mineralized domains, which, from north to south, are Steepledge, Escape North, Escape South, and the High Grade Zone (Fig. 2C) (Ciuculescu et al., 2023). The Steepledge Zone occurs north of the Quetico Fault in Quetico granitic rock, whereas the Escape North, South, and High Grade Zone occur south of the fault system in Quetico metasedimentary rock (Fig. 2C) (Caglioti, 2023). The Steepledge Zone is characterized by a tall, hourglass morphology. The Escape North Zone trends E–W (Fig. 2C) and is characterized as a narrow dike shape. The volumetrically larger Escape South and High Grade zones (Fig. 2C) have a more lopolithic morphology described as a mushroom, with an upper cap and a lower stem. The lithologies and stratigraphy observed within the Escape chonolith are similar to those

[1]Supplemental Material. Text S1: Analytical methods and assessment of mineral fractionation on lambda values. Figure S1: Downhole variation diagram through the Southeast Anomaly illustrating the variation in MgO, Al_2O_3, TiO_2, and Cr (from Brzozowski et al., 2023a), plus images of representative samples of mafic and ultramafic rocks from the Current intrusion. Figure S2: Chondrite-normalized REE profiles for the mafic–ultramafic rocks of the TBNIC and the country rocks. Figure S3: Binary diagrams illustrating the variations in εNd_t and $^{87}Sr/^{86}Sr_i$ as a function of Th/La for the mafic–ultramafic rocks of the TBNIC and a metasedimentary country rock sample. Figure S4: Binary diagrams illustrating the variations in λ_1–λ_2 of the mafic–ultramafic rocks of the TBNIC with MgO and λ_0. Table S1: Bulk-rock geochemical data (raw) of mafic–ultramafic rocks of the TBNIC and associated country rocks. Please visit https://doi.org/10.1130/GSAB.S.27237060 to access the supplemental material; contact editing@geosociety.org with any questions.

observed at Current, with lower olivine cumulates transitioning up stratigraphy to olivine gabbro, with more evolved ferro-gabbro, gabbro, and quartz gabbro occurring in the upper portion of the chonolith. Similar to Current, the upper gabbro and quartz gabbro typically contain xenoliths of quartz.

Lone Island is an elliptical intrusion ~900 m wide and up to 400 m thick emplaced into the metasedimentary rock of the Quetico Subprovince ~2 km west of the Escape intrusion (Fig. 2A) (Heggie, 2010; Yahia, 2024). Gabbroic rocks are volumetrically dominant, with a weakly defined stratigraphy displaying some cryptic geochemical cycles that laterally correlate to adjacent drill holes. The morphology of the intrusion has been interpreted as a sill or lopolith.

The East–West Corridor is a linear magnetic high feature that visually links the SE portions of the Lone Island, Escape, and Current intrusions. Exploration drilling completed on multiple sections along the strike of the magnetic lineament identified thin (<5 m), sheeted mafic intrusions emplaced into fractured and brecciated metasedimentary rock interpreted to be the Escape Fault, a splay off of the Quetico Fault (Fig. 2A) (Heggie, 2010; Yahia, 2024). The mafic intrusions display well developed chill margins that are typically spherultic, and coarsen slightly toward the centers, with phenocrysts of feldspar present.

The 025 intrusion occurs ~3 km northwest of Current (Fig. 2A) and is the only intrusion within the TBNIC that has olivine cumulate exposed at surface (Yahia, 2024). The intrusion is small, with a circular magnetic expression of ~200 m in diameter. Based on the surface exposure and the one drill hole through the intrusion, the main lithology is fine-grained peridotite grading upward into gabbro.

The Greenwich intrusion occurs ~4 km northeast of the Current intrusion (Dumas and Heggie, 2012; Yahia, 2024). It was identified as an elliptical isolated magnetic high, with a diameter of 300–400 m. Two exploration diamond drill holes tested the feature, and identified gabbro and melagabbro rocks, with a total thickness of ~184 m (Fig. 2A).

3. RESULTS

Details of the analytical methods are provided in the Supplemental Material, with the locations of samples provided in Table S1 alongside bulk-rock major- and trace-element geochemical data.

3.1. Zircon U–Pb Geochronology

Abundant skeletal zircon was recovered from the quartz gabbro sample from the Escape intrusion. Clear apatite and fine-grained, pale brown baddeleyite are also present, but rare, and were not selected for analysis. Although the zircons are coarse grained (reaching lengths of >300 μm), they contain inclusions of oxide minerals and are typically stained a reddish-brown color. U–Pb isotope results for four fractions of chemically abraded, elongate skeletal zircon (typically 2–3 grains each per fraction) are presented in Table 1 and Figure 3A. These zircon grains are characterized by moderately high U concentrations (459–773 ppm) and relatively high Th/U ratios (0.72–0.84). Model $^{207}Pb/^{206}Pb$ ages calculated for all four fractions fall consistently within the narrow range of 1107.7–1107.4 Ma, despite showing variable discordance from perfectly concordant to 2.7% reversely discordant (Fig. 3A; Table 1). The co-linearity of the isotope results for all four zircon fractions allows for a precise calculated weighted average $^{207}Pb/^{206}Pb$ age of 1107.6 ± 0.9 Ma with a high probability of fit (Fig. 3A).

The quartz gabbro sample from the East–West Corridor intrusion yielded only a sparse number of zircons of mostly irregular morphology and low quality. The few zircon grains of acceptable quality occur as anhedral, clear to slightly clouded, colorless to pale brown crystals. Three fractions of zircon were analyzed from this sample (Z1–Z3; Table 1; Figs. 3B and 3C). These zircon grains contain U contents of 146–222 ppm and Th/U ratios of 0.48–0.99, with Z1 having the highest ratios (Table 1). The U–Pb isotope results for fraction Z1, a single, clear, colorless and cracked fragment, partly overlaps the concordia with a $^{206}Pb/^{238}U$ age of 1070.5 ± 2.3 Ma and a $^{207}Pb/^{206}Pb$ age of 1076.4 ± 5.2 Ma (Fig. 3B); the distinctly elevated Th/U ratio for this analysis (0.99) is consistent with precipitation from a mantle-derived basic magma. The U–Pb isotope results of fractions Z2 and Z3, each comprising two grains or grain fragments, have concordant $^{207}Pb/^{206}Pb$ ages of 2699.0 Ma and 2772.8 Ma, respectively (Fig. 3C).

Only a meager population of zircon grains was obtained from olivine gabbro in the SEA body, consisting of small, irregular, altered, highly turbid, and generally poor quality crystals that were not suitable for U–Pb geochronology. Accordingly, no age dates were obtained for the SEA. Although no zircon grains were obtained from the quartz gabbro sample from the Greenwich intrusion, a robust population of fine-grained (20–100 μm long), fresh, bladed and blocky grains and grain fragments of baddeleyite was recovered (Fig. 3D). Three analyzed fractions of baddeleyite, each comprising 10–12 grains, all have high U (747–1177 ppm) and low Th/U ratios of 0.07–0.09, consistent with relatively pristine magmatic baddeleyite with little to no magmatic zircon overgrowth (Table 1). U–Pb isotope results for two fractions (Bd2, Bd3) fall within the concordia curve (0.1% and 0.2% discordant, respectively), whereas data for the third fraction (Bd1) partly overlaps the concordia and is 0.6% discordant (Fig. 3D). All three fractions have nearly identical model $^{207}Pb/^{206}Pb$ ages of 1105.8–1105.7 Ma, and collectively give a weighted average age of 1105.7 ± 0.9 Ma with a high degree of fit (Table 1; Fig. 3D).

3.2. Bulk-Rock Geochemistry

3.2.1. Major-Element Chemistry

Bulk-rock major- and trace-element compositions of the peridotites and gabbros that comprise the various intrusions of the TBNIC, as well as the country rocks into which the intrusions were emplaced, are presented in Table S1. All diagrams and discussions in the text refer to concentrations that have been recalculated to be 100% anhydrous. The major-element compositions of these rocks are illustrated in binary diagrams of MgO–CaO, MgO–Al_2O_3, and MgO–P_2O_5 (Fig. 4), alongside stoichiometric mineral compositions to allow for assessment of the main minerals present in the rocks.

The mafic–ultramafic rocks at Current, Escape, and 025 are compositionally similar, and can be subdivided into two broad groups, one at MgO >15 wt% (i.e., peridotite) and the other at MgO <15 wt% (i.e., gabbros) (Figs. 4A and 4B). The peridotites of the Current, Escape, and 025 intrusions exhibit positive correlations between MgO–CaO and MgO–Al_2O_3, and fall within the triangular area formed by connecting the forsteritic olivine, clinopyroxene, and plagioclase mineral nodes (Figs. 4A and 4B). It should be noted that, for Escape, two trends are evident in MgO–Al_2O_3 space, one overlapping the Current data and the other occurring at a shallower slope trending toward slightly more diopsidic clinopyroxene (Fig. 4B). The gabbros exhibit a positive correlation between MgO–CaO and a negative correlation between MgO–Al_2O_3 that has a steeper slope than the peridotites; this group of rocks plot along a trend between the clinopyroxene and plagioclase mineral nodes (Figs. 4A and 4B). Both the gabbros and peridotites exhibit negative correlations between MgO–P_2O_5, with the former exhibiting a steeper slope toward apatite (Fig. 4C). This, along with the low P_2O_5 contents (<1 wt%), are indicative of the presence of minor abundances of apatite.

3.2.2. Trace-Element Chemistry

The rare earth element (REE) chemistry of the peridotites and gabbros in the TBNIC are presented as lambda values, which are orthogonal polynomial coefficients that describe the shape of normalized REE profiles (chondrite-normalized REE profiles are provided in Fig. S2) (O'Neill,

TABLE 1. ZIRCON AND BADDELEYITE U–Pb ISOTOPE DATA AND AGE DATES OF QUARTZ GABBRO FROM INTRUSIONS OF THE THUNDER BAY NORTH INTRUSIVE COMPLEX, CANADA

Fraction	U (ppm)	Th/U	Pb^T (pg)	Pb_C (pg)	$^{206}Pb/^{204}Pb$	$^{207}Pb/^{235}U$	±2σ	$^{206}Pb/^{238}U$	±2σ	$^{207}Pb/^{206}Pb$	±2σ	Ages: $^{207}Pb/^{235}U$ (Ma)	±2σ (Ma)	$^{206}Pb/^{238}U$ (Ma)	±2σ (Ma)	$^{207}Pb/^{206}Pb$ (Ma)	±2σ (Ma)	Discordance (%)
18-DL-039: Quartz gabbro, Escape intrusion																		
Z1	459	0.838	149.64	2.15	3913	2.03108	0.00673	0.192605	0.00041	0.076482	0.000166	1126	2.3	1135.5	2.2	1107.7	4.3	−2.7
Z2	485	0.806	104.22	0.72	8241	1.99583	0.00534	0.189291	0.00039	0.07647	0.0001	1114.1	1.8	1117.5	2.1	1107.4	2.6	−1
Z3*	765	0.812	163.17	0.4	23240	1.97916	0.00386	0.187689	0.0003	0.076479	0.000053	1108.4	1.3	1108.8	1.6	1107.6	1.4	−0.1
Z4*	773	0.724	161.39	0.66	14140	1.97693	0.00337	0.187483	0.00025	0.076476	0.000059	1107.7	1.1	1107.7	1.3	1107.6	1.5	0
CAM-021-KY-061: Quartz gabbro, East–West Corridor																		
Z1	146	0.99	31.15	0.47	3632	1.8754	0.00668	0.180639	0.00041	0.075297	0.000194	1072.4	2.4	1070.5	2.2	1076.4	5.2	0.6
Z2	222	0.541	66.25	0.94	3953	13.27362	0.03935	0.520134	0.00131	0.185086	0.000205	2699.3	2.8	2699.7	5.5	2699	1.8	0
Z3	171	0.479	52.75	0.51	5812	14.40912	0.03894	0.539857	0.00124	0.193579	0.000178	2777	2.6	2782.8	5.2	2772.8	1.5	−0.4
CAM-021-KY-081: Quartz gabbro, Greenwich intrusion																		
Bd1	747	0.071	104.83	3.81	1895	1.95931	0.00437	0.185978	0.00023	0.076408	0.000126	1101.6	1.5	1099.5	1.3	1105.8	3.3	0.6
Bd2	1177	0.086	166.73	1.78	6391	1.96859	0.00301	0.186869	0.00018	0.076404	0.000059	1104.8	1	1104.4	1	1105.7	1.5	0.1
Bd3	958	0.084	146.48	1.8	5757	1.96738	0.00283	0.18675	0.00019	0.076405	0.00005	1104.4	1	1103.7	1	1105.7	1.3	0.2

Note: All analyzed zircon fractions represent best optical quality (crack, inclusion, and core-free), fresh (least altered) grains. All zircons were chemically abraded. Pb^T is total amount of Pb. Pb_C is total measured common Pb assuming the isotopic composition of laboratory blank: 206/204—18.49 ± 0.4%; 207/204—15.59 ± 0.4%; 208/204—39.36 ± 0.4%. Pb/U atomic ratios are corrected for spike, fractionation, blank, and where necessary, initial common Pb; $^{206}Pb/^{204}Pb$ is corrected for spike and fractionation. Th/U is model value calculated from radiogenic $^{208}Pb/^{206}Pb$ ratio and $^{207}Pb/^{206}Pb$ age, assuming concordance. Discordance (%) is the percent discordance for the given $^{207}Pb/^{206}Pb$ age. Uranium decay constants are from Jaffey et al. (1971).
*Fraction spiked with ET535 ^{205}Pb–^{233}U–^{235}U isotopic tracer; remaining fractions mixed with the JSGL ^{205}Pb–^{235}U tracer.

2016). λ_0 describes the abundance of REEs, with higher values indicative of greater REE abundances (e.g., 0.97 for primitive mantle versus 3.57 for ocean-island basalt [OIB]). λ_1 describes the slope of a REE pattern, where positive and negative values indicate positive and negative slopes, respectively, and the magnitude of the value is indicative of the magnitude of the slope (e.g., −2.68 for normal mid-ocean-ridge basalt [N-MORB], 3.39 for enriched [E]-MORB, and 14.7 for OIB). λ_2 describes the curvature of a REE pattern, where positive and negative values are indicative of concave-up and concave-down curves, respectively, and the magnitude of the value is indicative of the magnitude of the curvature (e.g., 24.5 for E-MORB and −13.3 for OIB). The peridotites and gabbros are characterized by positive and relatively invariable λ_1 values, but notably variable λ_0, with the gabbros having higher λ_0 than the peridotites (Fig. 5). In λ_1–λ_2 space, the majority of peridotite and gabbros are characterized by systematically positive and relatively invariable λ_1 values, and variable λ_2 values that extend toward values more negative than OIB, indicative of steep, variably concave-up REE profiles (Fig. 5B). The peridotites and gabbros have similar REE abundances (λ_0) among the intrusions (Fig. 5A). The slopes (λ_1) and curvature (λ_2) of the REE profiles of the mafic–ultramafic rocks in the different intrusions do, however, vary slightly (Fig. 5B). With respect to slope, there is a range of λ_1 values from ~13 to 18, with Current, Lone Island, and the East–West Corridor having higher, but often overlapping, values than Escape, 025, and Greenwich (Fig. 5). With respect to the curvature, the λ_2 values range from approximately −73 to −10, with the intrusions generally exhibiting significant overlap. The peridotite and gabbros are characterized by variably negative Nb anomalies, with Nb/La of 0.36–0.89 (one sample has Nb/La of 0.11), and no Th enrichment, with Th/La values of 0.05–0.12 (seven samples have Th/La >0.12) (Fig. 6; Table 1). The granitic and metasedimentary country rocks in the TBNIC are characterized by systematically elevated Th/La values of 0.17–1.147 (one sample has Th/La <0.12) and highly variable Nb/La of 0.06–88.14 (the majority of country rock samples have Nb/La <1) (Fig. 6; Table 1).

3.2.3. Sm–Nd and Rb–Sr Isotopes

The peridotites and gabbros from all of the intrusions have variably negative εNd_t values of −5.3 to −1.2, as well as variable $^{87}Sr/^{88}Sr_i$ of 0.70044–0.70628 (Fig. 7; Table 2). Although the εNd_t and $^{87}Sr/^{88}Sr_i$ values of the rocks are negatively correlated when all of the intrusions are considered together, no correlations seemingly exist among samples within a given intru-

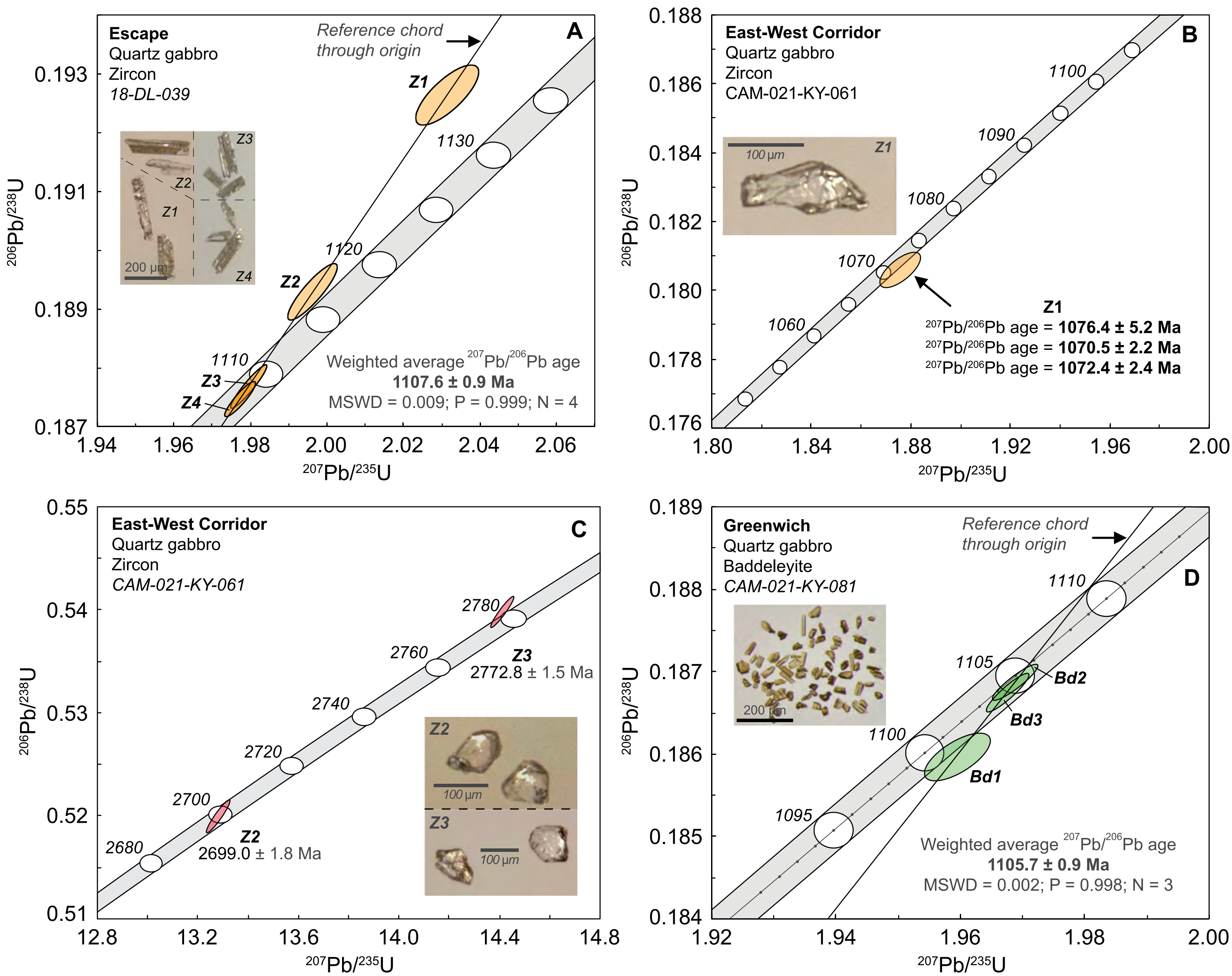

Figure 3. U–Pb concordia diagrams of zircon from (A) the Escape intrusion and (B, C) the East–West Corridor and baddeleyite from (D) the Greenwich intrusion of the Thunder Bay North Intrusive Complex, Canada. Inset figures illustrate representative zircon and baddeleyite fractions. MSWD—mean square of weighted deviates; P—probability of concordance; N—number of zircon/baddeleyite fractions.

sion, apart from Current (Fig. 7). Similarly, no correlations exist between εNd_t and $^{87}Sr/^{88}Sr_i$, and the Th/La values of the rocks (Fig. S3). A single sample of the metasedimentary country rock has εNd_t and $^{87}Sr/^{88}Sr_i$ values of −20.5 and 0.76374, respectively, and an elevated Th/La value of 0.41, which are distinct from plutonic rocks of the TBNIC (Fig. 7; Fig. S3).

4. DISCUSSION

4.1. Age of the Thunder Bay North Intrusive Complex

Robust magmatic U–Pb ages determined from zircon and baddeleyite from the Escape and Greenwich intrusions are similar, but statistically different (at the 2σ level) at 1107.6 ± 0.9 Ma and 1105.7 ± 0.9 Ma, respectively (Figs. 3A and 3D), indicating that the latter was emplaced immediately on the heels of the Escape intrusion. Although the mean ages determined for the Current (1106.6 ± 1.6 Ma, zircon; Bleeker et al., 2020) and Lone Island (1106.3 ± 2.1 Ma, baddeleyite; Metsaranta and Kamo, 2021) intrusions are slightly older and younger than for the Greenwich and Escape bodies, respectively, they are statistically indistinguishable from each other and the other intrusions within the errors of these determinations.

The zircon $^{207}Pb/^{206}Pb$ ages determined for the East–West Corridor sample range from 1076.4 ± 5.2 Ma for fraction Z1, to 2699 ± 1.8 Ma and 2772.8 ± 1.5 Ma for zircon fractions Z2 and Z3, respectively (Figs. 3B and 3C). The age results for the latter fractions, which each comprised two grains or grain fragments, clearly reflect inheritance of older Pb as indicated by their concordant Neoarchean ages (Fig. 3C; Table 1). These ages undoubtedly reflect the age of the underlying Archean Quetico Subprovince basement, which is locally characterized by a mixture of granitic gneiss and paragneiss. However, because fractions Z2 and Z3 each represent multigrain zircon digestions, they likely represent mixed ages of xenocrystic zircon, despite appearing to be effectively concordant. The ages determined for zircon fraction

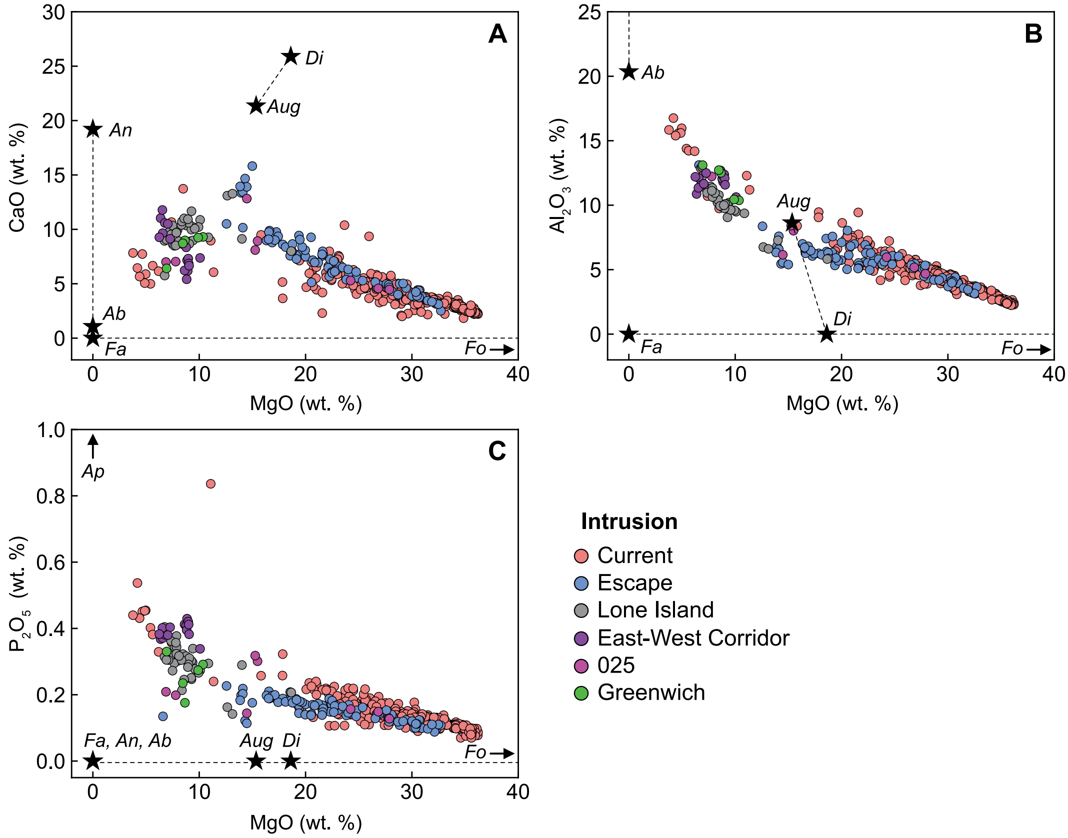

Figure 4. Binary diagrams illustrating the variations in (A) CaO, (B) Al_2O_3, and (C) P_2O_5 as a function of MgO (all in wt%) for the mafic–ultramafic rocks of the Thunder Bay North Intrusive Complex, Canada. The black stars are stoichiometric mineral compositions, with dashed lines connecting solid solutions. Ab—albite; An—anorthite; Ap—apatite; Aug—augite; Di—diopside; Fa—fayalite; Fo—forsterite.

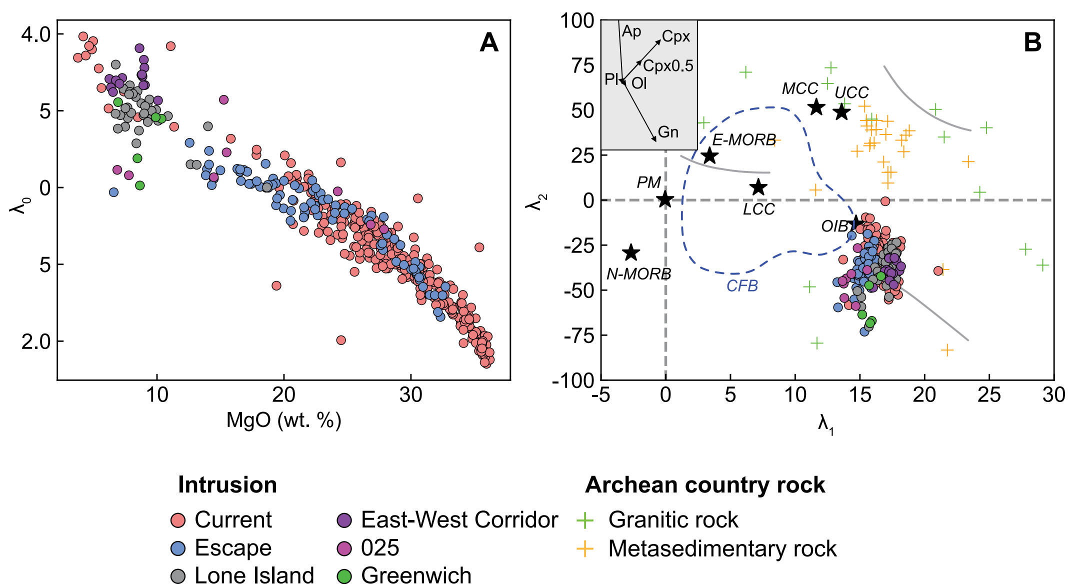

Figure 5. Binary diagrams illustrating the variations in (A) λ_0–MgO and (B) λ_1–λ_2 for mafic–ultramafic rocks of the Thunder Bay North Intrusive Complex, Canada, as well as the granitic and metasedimentary country rocks of the Quetico Subprovince (see text for a description of λ values; chondrite-normalized rare earth element [REE] profiles are provided in Fig. S2; see text footnote 1). The dashed gray lines represent primitive mantle compositions. The stars represent the compositions of primitive mantle (PM) from McDonough and Sun (1995), normal mid-ocean-ridge basalt (N-MORB), enriched (E)-MORB, and ocean-island basalt (OIB) from Sun and McDonough (1989), and lower (LCC), middle (MCC), and upper (UCC) continental crust from Rudnick and Gao (2003). The field for continental flood basalts (CFB) is from Barnes et al. (2021). The gray curves represent the shape of the REE profile at specific λ_1–λ_2 values. The vectors in the gray box illustrate the effects of Rayleigh fractionation of plagioclase (Pl), clinopyroxene (Cpx), olivine (Ol), apatite (Ap), and garnet (Gn) on the REE profile of a residual melt. Mineral–melt partition coefficients used to model mineral fractionation are from Bédard et al. (2009), except for majorite garnet, which are from Bobrov et al. (2014).

Z1 ($^{207}Pb/^{206}Pb$: 1076.4 ± 5.2 Ma, $^{206}Pb/^{238}U$: 1070.5 ± 2.2 Ma) are notably younger than the other intrusions in the TBNIC (Figs. 3A, 3B, and 3D) and most other rocks in the MRS (Bleeker et al., 2020). The determined age may, therefore, reflect secondary loss of radiogenic Pb from relict, metamict domains in the zircon crystal lattice. This interpretation is consistent with the fact that the East–West Corridor occurs along the

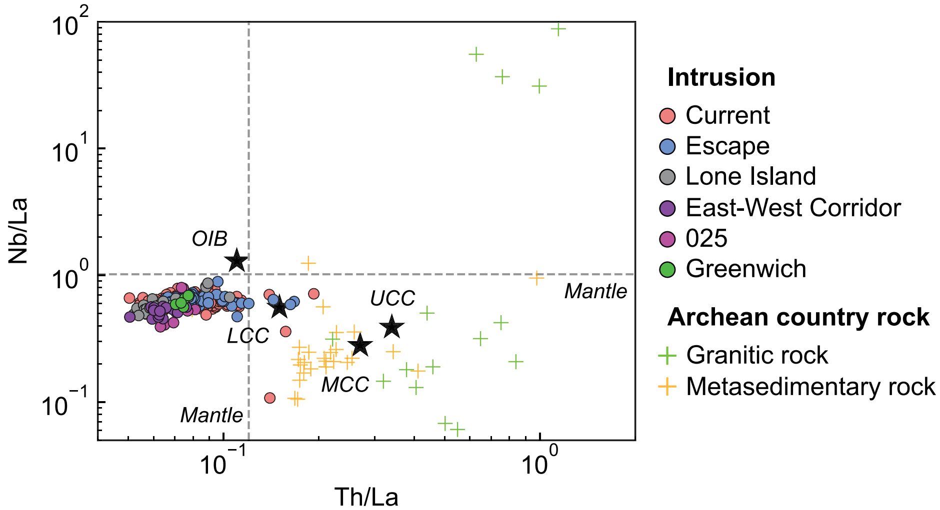

Figure 6. Binary diagram illustrating the variation in Nb/La (Nb anomaly) and Th/La (Th enrichment/depletion) of mafic–ultramafic rocks in the Thunder Bay North Intrusive Complex, Canada, as well as the granitic and metasedimentary country rocks of the Quetico Subprovince. The dashed gray lines represent primitive mantle compositions. The stars represent reservoir compositions as described in Figure 5. OIB—ocean-island basalt; LCC—lower continental crust; MCC—middle continental crust; UCC—upper continental crust.

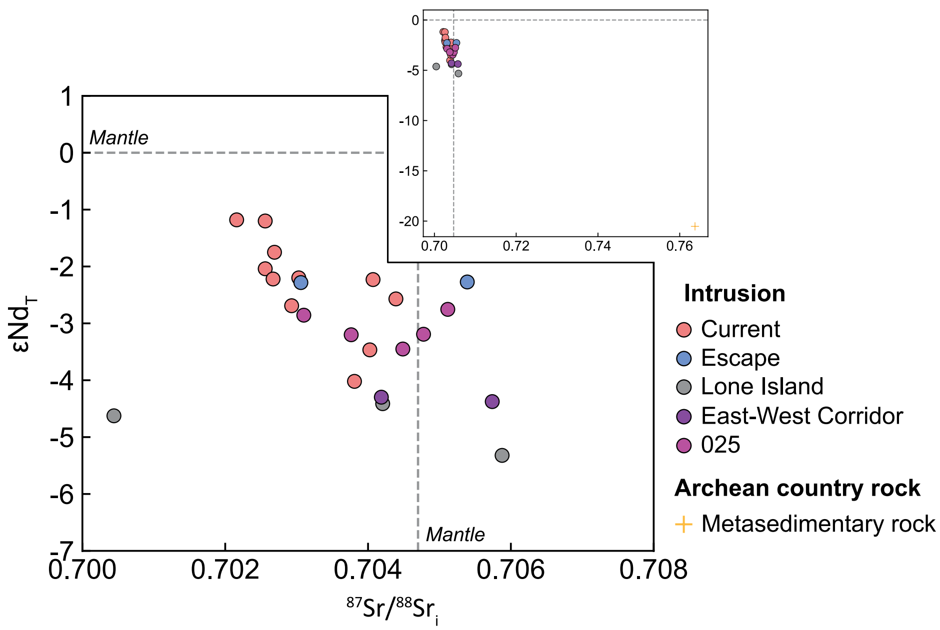

Figure 7. Binary diagram showing the variation in εNd_t and $^{87}Sr/^{86}Sr_i$ of the mafic–ultramafic rocks of the Thunder Bay North Intrusive Complex, Canada. The inset figure is the same graph, but with the scale expanded to show the composition of the metasedimentary rock sample. The dashed gray lines represent the mantle values for εNd_t (0) and $^{87}Sr/^{86}Sr_i$ (0.7047) from Caro and Bourdon (2010).

Escape Lake Fault (Fig. 2), which could have served as a pathway for fluids to have altered the zircon and caused minor Pb loss. Additional geochronological work is required to better understand the timing of emplacement of the East–West Corridor and its temporal relationship to the other intrusions of the TBNIC.

To summarize, the ages determined here for the Escape (1107.6 ± 0.9 Ma) and Greenwich (1105.7 ± 0.9 Ma) intrusions, combined with the 1106.6 ± 1.6 Ma (Bleeker et al., 2020) and 1106.3 ± 2.1 Ma (Metsaranta and Kamo, 2021) ages of the Current and Lone Island intrusions, respectively, demonstrate that the TBNIC was emplaced as part of the ca. 1.1 Ga Midcontinent Rift event. Although the ages of the intrusions generally overlap within error, the small errors on the Escape and Greenwich ages determined here demonstrate that the Escape intrusion was emplaced before the Greenwich intrusion, and that the Thunder Bay North intrusive event lasted for ~2 m.y. based on the best available ages.

4.2. Genetic Relationship between Intrusions of the TBNIC

Mineralogically, the rocks that comprise the TBNIC intrusions are similar, comprising variable accumulations of olivine > clinopyroxene (± limited orthopyroxene and apatite) and interstitial liquid (Fig. 4), with the higher overall REE abundances (λ_0) of the gabbros suggesting that they represent the fractionated counterpart of the peridotites (Fig. 5A). In terms of REE geochemistry, the intrusions are characterized by similar REE abundances (λ_0), but the slopes (λ_1) and curvatures (λ_2) of their REE profiles, although all light (L)REE-enriched and concave-down, are slightly variable (Fig. 5). In general, Escape, Greenwich, and 025 have marginally shallower REE profiles (i.e., lower λ_1) than Current, Lone Island, and the East–West Corridor, but there is significant overlap (Fig. 5). Although the curvature of the profiles (λ_2) exhibits some variability, there are no systematic differences among the intrusions (Fig. 5B). While the variations in λ_1–λ_2 may suggest that the intrusions crystallized from genetically distinct magmas derived from different mantle sources, few processes are capable of fractionating the REEs, and modifying the slope and curvature of REE profiles. These minor variations, therefore, need to be evaluated.

In terms of mantle processes, although higher degrees of mantle partial melting generate shallower REE profiles (i.e., lower λ_1), it does not affect their concavity (λ_2) unless minerals that preferentially retain the middle REEs (e.g., hornblende, Higuchi and Nagasawa, 1969) are retained in the source, which is more common in hydrous, subduction zone settings. The variations in λ_1–λ_2 observed among the TBNIC intrusions, therefore, cannot be a result of variable degrees of partial melting. Contamination can be ruled out because the granitic and sedimentary country rocks have highly variable λ_1–λ_2 (Fig. 5) that would have resulted in significant scatter in the λ_1–λ_2 values of the mafic–ultramafic rocks if assimilated. Mineral accumulation can also be ruled out as having had a significant impact on the λ_1–λ_2 values (and hence REE

TABLE 2. Rb–Sr AND Sm–Nd ISOTOPE COMPOSITIONS OF MAFIC–ULTRAMAFIC ROCKS OF THE THUNDER BAY NORTH INTRUSIVE COMPLEX AND SPATIALLY ASSOCIATED METASEDIMENTARY COUNTRY ROCKS, CANADA

Sample Name	Lithology	Age (Ma)	Nd (ppm)	Sm (ppm)	$^{143}Nd/^{144}Nd$	$^{147}Sm/^{144}Nd$	$^{143}Nd/^{144}Nd_{initial}$	εNd_T	Rb (ppm)	Sr (ppm)	$^{87}Sr/^{86}Sr$	$^{87}Rb/^{86}Sr$	$^{87}Sr/^{86}Sr_{initial}$
Current													
CAM-MB-21-09	Mafic–ultramafic	1106.6	17.8	3.7	0.51200	0.12385	0.51111	−2.0	8.4	272.0	0.70398	0.08964	0.70256
CAM-MB-21-62	Mafic–ultramafic	1106.6	14.7	3.1	0.51208	0.12889	0.51115	−1.2	5.4	241.0	0.70359	0.06505	0.70256
CAM-MB-21-85	Mafic–ultramafic	1106.6	17.2	3.5	0.51204	0.12312	0.51115	−1.2	21.8	140.0	0.70930	0.45062	0.70216
CAM-MB-21-127	Mafic–ultramafic	1106.6	16.1	3.3	0.51201	0.12314	0.51112	−1.8	5.8	245.0	0.70377	0.06800	0.70269
CAM-MB-21-136	Mafic–ultramafic	1106.6	9.3	1.9	0.51199	0.12380	0.51110	−2.2	4.1	183.0	0.70510	0.06513	0.70407
CAM-MB-21-144	Mafic–ultramafic	1106.6	11.0	2.3	0.51199	0.12348	0.51110	−2.2	4.2	172.0	0.70379	0.07079	0.70267
CAM-MB-21-163	Mafic–ultramafic	1106.6	18.4	3.8	0.51198	0.12476	0.51107	−2.7	12.1	352.0	0.70451	0.09943	0.70293
CAM-MB-21-177	Mafic–ultramafic	1106.6	26.5	5.3	0.51195	0.12003	0.51108	−2.6	14.3	75.4	0.71308	0.54904	0.70439
CAM-MB-21-184	Mafic–ultramafic	1106.6	22.0	4.5	0.51199	0.12322	0.51110	−2.2	13.2	355.0	0.70473	0.10756	0.70303
CAM-MB-21-91	Mafic–ultramafic	1106.6	20.4	4.2	0.51190	0.12308	0.51100	−4.0	13.2	155.0	0.70772	0.24641	0.70381
CAM-021-KY-018	Mafic–ultramafic	1106.6	52.7	10.0	0.51187	0.11533	0.51103	−3.5	19.8	748.0	0.70524	0.07657	0.70402
CAM-021-KY-017	Metasedimentary	1106.6	56.6	8.8	0.51084	0.09371	0.51016	−20.5	177.0	177.0	0.81000	2.92238	0.76371
Escape													
CAM-21-CC-038	Mafic–ultramafic	1106.6	23.4	5.5	0.51213	0.14233	0.51109	−2.3	2.6	89.6	0.70671	0.08365	0.70539
CAM-21-CC-039	Mafic–ultramafic	1106.6	10.6	2.2	0.51200	0.12460	0.51109	−2.3	5.4	192.3	0.70435	0.08168	0.70306
Lone Island													
CAM-021-KY-001	Mafic–ultramafic	1106.6	48.7	10.3	0.51187	0.12844	0.51094	−5.3	29.9	628.0	0.70806	0.13777	0.70588
CAM-021-KY-004	Mafic–ultramafic	1106.6	48.2	9.5	0.51185	0.11876	0.51098	−4.4	33.2	930.0	0.70584	0.10327	0.70420
CAM-021-KY-012	Mafic–ultramafic	1106.6	30.1	6.0	0.51185	0.12051	0.51097	−4.6	36.5	200.0	0.71455	0.52811	0.70044
East–West Corridor													
CAM-021-KY-029	Mafic–ultramafic	1106.6	53.2	10.5	0.51186	0.11972	0.51099	−4.4	31.1	380.0	0.70949	0.23685	0.70574
CAM-021-KY-036	Mafic–ultramafic	1106.6	54.3	10.5	0.51184	0.11699	0.51099	−4.3	20.4	811.0	0.70534	0.07276	0.70419
O25													
CAM-021-KY-065	Mafic–ultramafic	1106.6	27.0	6.1	0.51204	0.13658	0.51105	−3.2	64.7	521.0	0.71047	0.35942	0.70477
CAM-021-KY-066	Mafic–ultramafic	1106.6	23.9	5.0	0.51197	0.12776	0.51105	−3.2	24.4	346.0	0.70699	0.20403	0.70376
CAM-021-KY-093	Mafic–ultramafic	1106.6	30.2	6.7	0.51201	0.13502	0.51103	−3.4	36.4	436.0	0.70831	0.24158	0.70448
CAM-021-KY-094	Mafic–ultramafic	1106.6	24.8	5.7	0.51207	0.13847	0.51107	−2.7	17.7	118.0	0.71199	0.43420	0.70511
CAM-021-KY-095	Mafic–ultramafic	1106.6	18.0	3.7	0.51198	0.12560	0.51106	−2.9	22.3	240.0	0.70736	0.26884	0.70310

geochemistry) of the mafic–ultramafic rocks for two reasons (see the Supplemental Material for additional details). First, although λ_1–λ_2 values vary systematically with MgO (i.e., a proxy for mineral accumulation), the variation is minimal (Fig. S4A). Second, considering that λ_0 values exhibit minor variability throughout the dataset (Fig. S4B), it is evident that while silicates did accumulate in these intrusions, the rocks do not represent pure cumulates, but rather interstitial liquid > accumulated minerals. Again, although λ_1–λ_2 values do vary systematically with λ_0 (but opposite to MgO), the overall variability is small (Fig. S4B). This conclusion is consistent with the demonstrations by O'Neill (2016) and Barnes et al. (2021) that mineral accumulation does not affect λ_1–λ_2 values. For example, comparing ocean floor basalts that accumulated variable amounts of olivine to ocean floor glasses, O'Neill (2016) found that they had indistinguishable λ_1–λ_2 values and hence REE profiles. Using olivine-only and plagioclase–pyroxene mesocumulates from the Albany-Fraser Orogen (Australia), Barnes et al. (2021) demonstrated that accumulation of these minerals had minimal impact on λ_1–λ_2 values, with plagioclase–pyroxene cumulates having only slightly lower λ_1 values than the olivine-only mesocumulates (although there is significant overlap). Fractionation of olivine and plagioclase do not affect the shape of REE profiles and can, therefore, be ruled out as having had an effect on the λ_1–λ_2 variations (cf. inset in Fig. 5B). Given that the heavy REEs are more compatible into garnet than the LREEs, the systematically positive λ_1 and negative λ_2 values that characterize the TBNIC intrusions are indicative of garnet fractionation (O'Neill, 2016), implying that their magmas originated from within the garnet stability field, similar to many mafic–ultramafic intrusions (e.g., Eva Kitto, Seagull, Thunder, Shillabeer; Brzozowski et al., 2023b) and volcanic packages (Keays and Lightfoot, 2015) in the MRS. Unlike olivine and plagioclase, which do not affect REE profiles, clinopyroxene fractionation increases the λ_0, λ_1, and λ_2 values of residual melts (cf. insets in Fig. 5B). Considering the clinopyroxene fractionation trends in λ_1–λ_2 space, and the variable fractionation/accumulation of clinopyroxene in the TBNIC rocks demonstrated by variations in their major-element chemistry (Fig. 4), it is likely that the variations in REE profiles within and among the TBNIC intrusions are, in part, a result of variable amounts of clinopyroxene fractionation and accumulation (Fig. 5). The final possibility that can modify the shape of REE profiles is apatite fractionation/accumulation given the variably elevated apatite–melt partition coefficients for the REEs (Bédard et al., 2009). Small degrees of apatite fractionation/accumulation (<5%) causes significant increases in λ_2 (>50 λ values) and negligible decreases in λ_1 (cf. inset in Fig. 5B), as demonstrated by the Layered Series in the Eastern Gabbro of the Coldwell Complex (Good et al., 2021; Brzozowski et al., 2022). Given the presence of minor amounts of apatite in the mafic–ultramafic rocks of the TBNIC intrusions (Fig. 4C), the variations in λ_2 were likely generated, at least in part, as a result of accumulation of minor amounts of apatite (Fig. 5B).

We, therefore, consider that the different intrusions of the TBNIC likely crystallized from magmas that originated from the same deep mantle source where garnet was stable (i.e., they are co-genetic), with minor variations in their REE profiles reflecting variable amounts of clinopyroxene and apatite fractionation/accumulation. This genetic relationship is consistent with the generally indistinguishable ages of the Escape (1107.6 ± 0.9 Ma), Current (1106.6 ± 1.6 Ma; Bleeker et al., 2020), and Greenwich (1105.7 ± 0.9 Ma) intrusions (Fig. 3) because it is the ages that imply that most of the TBNIC magmatism was essentially synchronous in its emplacement and crystallization.

4.3. Crustal Contamination and Mantle Source Contributions

The mafic–ultramafic rocks in the intrusions of the TBNIC are characterized by consistently negative εNd_t values of −5.3 to −1.2 and negative Nb anomalies (Nb/La = 0.16–0.89; Figs. 6 and 7). These geochemical–isotopic features could have been generated by contamination of the magmas by crustal material during emplacement. However, the depleted Th contents (Th/La = 0.05–0.12, with few samples up to 0.17; Fig. 6) and mantle-like $^{87}Sr/^{88}Sr_i$ values (0.7004–0.7063; Fig. 7) of most of the mafic–ultramafic rocks, but elevated Th and $^{87}Sr/^{88}Sr_i$ compositions of the country rocks (Th/La = 0.08–1.27; $^{87}Sr/^{88}Sr_i$ = 0.7637; Figs. 6 and 7), argues against significant crustal input, as does the lack of negative correlations between Th/La–Nb/La–εNd_t (Fig. 6; Fig. S3). To further assess the importance of crustal contamination on the magmatic evolution of the intrusions in the TBNIC, variations in Th/La–Nb/La, εNd_t–Nb/La, and εNd_t–Th/La as a function of contamination of plume-derived magmas with TBNIC country rocks have been modeled. The end-member compositions of the initial silicate melt and country rocks are provided in Table 3, along with an explanation of why those values were chosen.

In Th/La–Nb/La space, apart from a limited subset of samples (~1% of the dataset) that have elevated Th/La, the majority of the peridotite and gabbro samples fall along a trend that is oblique to that expected for contamination of a plume-derived magma by Quetico country rocks (Fig. 8A). Likewise, the samples also fall along a trend perpendicular to the plume–Quetico mixing trends in εNd_t–Th/La space (Fig. 8B). In εNd_t–Nb/La space, although the data exhibit a similar slope to the plume–Quetico mixing trends, they are characterized by notably less enriched εNd_t values than expected based on Quetico assimilation (Fig. 8C). Simply contaminating a plume-derived magma with Quetico rocks cannot, therefore, explain the geochemical and isotopic variability observed in the TBNIC rocks. This interpretation is consistent with multiple S isotope and S/Se values of the Current deposit that are indicative of selective contamination of the magma by Archean rocks at depth rather than bulk assimilation (Brzozowski et al., 2023a).

Although formation of the MRS has been interpreted to be due to the impingement of the Keweenaw Plume beneath the crust (Hutchinson et al., 1990; Nicholson and Shirey, 1990; Nicholson et al., 1997), it has been well demonstrated that many of the volcanic and intrusive rocks do not represent crystallization of purely plume-derived magmas. Using trace-element geochemistry (e.g., Th/La, Ce/Yb) and Nd–Os isotopes, Shirey et al. (1994) and Shirey (1997) demonstrated that different formations within the Mamainse Point Volcanic Group crystallized from magmas formed by the interaction of the Keweenaw Plume with old SCLM (lower formation basalts with negative εNd_t and γOs_i) and MORB (upper formation basalts with positive εNd_t). Good and Lightfoot (2019) interpreted the decoupling of the large ion lithophile elements from the LREEs and HREEs, decoupling of REEs from the high field strength elements, and the enriched Nd isotope values of the metabasalts in the Coldwell Complex to indicate crystallization from partial melts derived from a metasomatized SCLM source. Similarly, Rooney et al. (2022) suggested that the alkaline magmas from which the Coldwell and Seabrook Lake complexes crystallized represent mixtures of enriched SCLM and some other depleted end member based on their positive εNd_{1100} and variably negative to positive εHf_{1100}. Recently, Brzozowski et al. (2023b) demonstrated, using Nd–Os isotopes, that several mafic–ultramafic intrusions (i.e., Eva Kitto, Seagull, Thunder, Shillabeer, Jackfish) on the north shore of Lake Superior, and proximal to the TBNIC, crystallized from melts that were largely derived from the SCLM and that assimilated limited material during transport through the crust, consistent with their generally depleted Th abundances.

Given the evidence for SCLM contributions to MRS magmatism, we modeled the variation of εNd_t, Th/La, and Nb/La as a function of mixing between plume, SCLM, and Quetico country rocks. Given that limited mantle xenoliths have been identified within the MRS, with only one reported occurrence east of the rift system (Legros et al., 2024), the Th, La, and Nd values of the SCLM end member were set to be similar to those reported by McDonough (1990) for cratonic peridotite xenoliths. Although Legros et al. (2024) documented Nb enrichment in the mantle xenoliths identified near Elliot Lake, Ontario, Canada, the enrich-

TABLE 3. END-MEMBER COMPOSITIONS FOR MIXING MODELS USED TO CHARACTERIZE CRUSTAL CONTAMINATION AND MAGMA SOURCE FOR THE THUNDER BAY NORTH INTRUSIVE COMPLEX, CANADA

Reservoir	Th (ppm)	La (ppm)	Nb (ppm)	Nd (ppm)	εNd_T	Reasoning	References
Initial silicate magma	4	37	48	55.0	0	Composition of ocean-island basalt from Sun and McDonough (1989) and utilized by Rooney et al. (2022) for the composition of the Keweenaw Plume.	Sun and McDonough (1989), Rooney et al. (2022)
Granite 1	45	90	6	77	−21	The trace-element compositions for granite 1 and metasedimentary rock are equivalent to samples CAM-021-KY-102 and CAM-21-CC-090, respectively, in Table S1 (see text footnote 1). The composition of granite 2 is equivalent to sample 04TRH250 from Cundari et al. (2021). The εNd_i values of the granitic and metasedimentary rocks were set to −21, which is equivalent to the value obtained for a metasedimentary rock sample in this study (CAM-021-KY-017 in Table S1; see text footnote 1) and similar to other rocks of the Quetico Subprovince reported by Hollings et al. (2007b).	Cundari et al. (2021), Hollings et al. (2007b)
Granite 2	33	157	4	90	−21		
Metasedimentary rock	7	32	7	34	−21		
Subcontinental lithospheric mantle (SCLM)	0.15	3	0.2	13.5	−9	The trace-element concentrations are within the range of values reported by McDonough (1990) for spinel peridotite xenoliths from continental regions. A lower value was used for Nb to be more representative of the depleted nature of old SCLM. The εNd_i value is equivalent to that utilized by Shirey et al. (1994), Shirey (1997), and Brzozowski et al. (2023b) for the SCLM beneath the Midcontinent Rift.	McDonough (1990), Shirey et al. (1994), Shirey (1997), Brzozowski et al. (2023b)

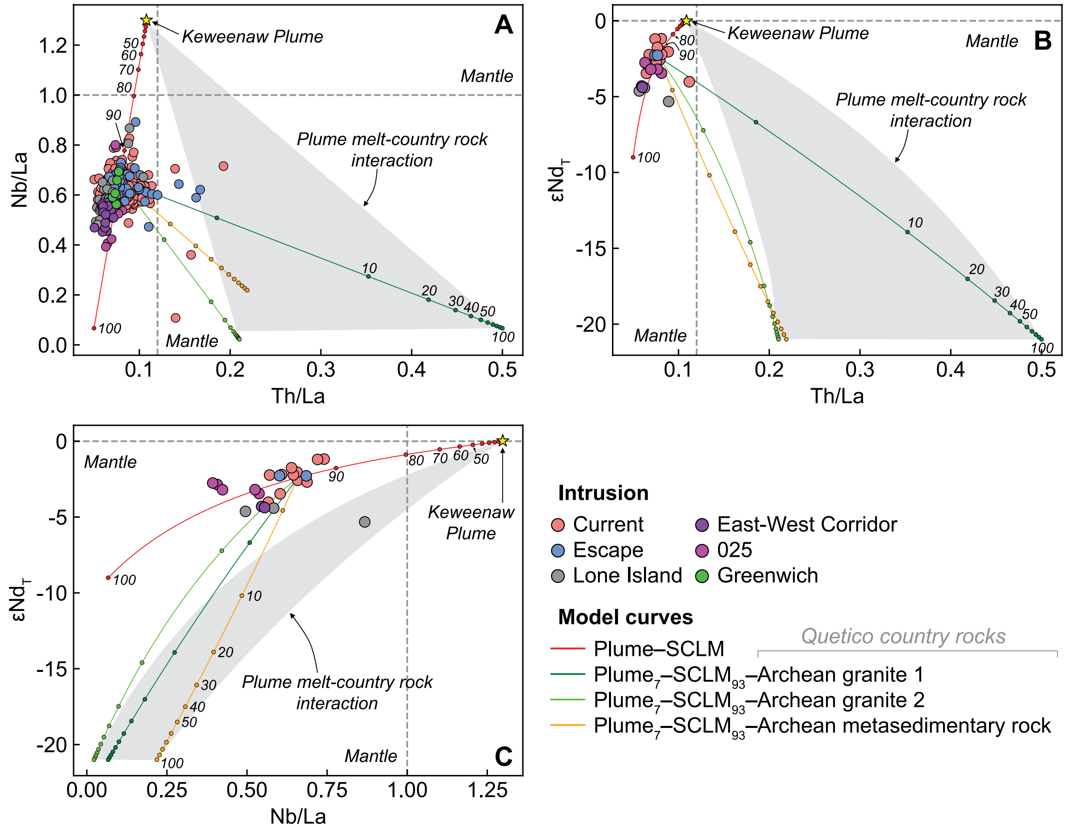

Figure 8. Binary diagrams illustrating the modeled variations in (A) Nb/La–Th/La, (B) εNd_t–Th/La, and (C) εNd_t–Nb/La as a function of mixing between Keweenaw Plume melt and Quetico country rocks (gray field), Keweenaw Plume–subcontinental lithospheric mantle (SCLM) (red curve), and a Keweenaw Plume (7%)–SCLM (93%) hybrid melt and Quetico country rocks (green and orange curves), Canada. The compositions of the mafic–ultramafic rocks of the Thunder Bay North Intrusive Complex are overlain. The end-member compositions used in the modeling are provided in Table 3.

ment was interpreted to be a result of carbonated silicate metasomatism. Brzozowski et al. (2022), however, demonstrated that the Eastern Gabbro of the Coldwell Complex (and likely other rocks in the north–northeast portion of the MRS) crystallized from melts derived from a mantle source that was metasomatized by slab-derived fluids, which would not have introduced Nb to the source given its relative immobility. Accordingly, the Nb abundances of the SCLM end member were set to a lower value to account for the effects of long-term depletion and metasomatic re-enrichment of the SCLM (Good and Lightfoot, 2019). Such Nb depletion is a characteristic feature of many within-plate basalt packages that crystallized from melts with a significant SCLM component, such as the Tuklonsky basalts in Russia, which exhibit a range of Nb/La ratios from near primitive mantle to notably lower than mantle (i.e., negative Nb anomaly) (Lightfoot et al., 1993).

The peridotite and gabbros of the TBNIC have compositions that generally follow the plume–SCLM mixing trends, with most of the samples having compositions indicative of greater than 90% mixing (Fig. 8). This suggests that the magmas from which the TBNIC rocks crystallized were largely derived from melting of the SCLM, with limited (<10%) input of material from the Keweenaw Plume. Such large contributions from the SCLM are similar to those suggested for the Eva Kitto, Seagull, and Shillabeer intrusions, which are located several kilometers northeast of the TBNIC within the Nipigon Embayment (Fig. 1), and greater than those suggested for the Thunder, Jackfish, and Mamainse Point Volcanic Group (Shirey et al., 1994; Shirey, 1997; Brzozowski et al., 2023b). Plume–SCLM mixing cannot, however, fully explain the geochemical and isotopic variability observed in the TBNIC as a subset of samples pull toward elevated Th/La (Figs. 8A and 8B) and fall below the plume–SCLM mixing curve in εNd_t–Nb/La space (Fig. 8C). These comparatively Th-enriched samples can be explained by assimilation of <5% (typically <2%) Quetico country rock by predominantly SCLM-derived magmas (93% SCLM, 7% plume; Fig. 8). It is interesting to note that only peridotite and gabbros at Escape and Current (± Lone Island) exhibit evidence for contamination, with rocks in the other intrusions generally falling tightly along the plume–SCLM mixing line and exhibiting limited geochemical evidence for bulk assimilation of Quetico country rock (Fig. 8A). The overall limited degrees of contamination of the peridotite and gabbros are consistent with the absence of country rock xenoliths in these rocks and the lack of significant variability in their trace-element compositions, which may be expected given the geochemical variability of the granitic and metasedimentary country rocks (Fig. 5). The limited variations that are present in the abundance (λ_0) and degree of fractionation (λ_1) of the REEs of the gabbros can largely be attributed to fractionation of clinopyroxene (Fig. 5).

Two key points can be taken away from this discussion. First, the magmas that fed the TBNIC were largely derived from partial melting of the SCLM (>90%), with the Keweenaw Plume contributing only limited (<10%) amounts of material. Second, the SCLM-derived magmas represented now by the spatially associated intrusions in the TBNIC assimilated limited crustal material during emplacement. This contamination appears to be largely restricted to the Current and Escape (± Lone Island) intrusions. The greater degrees of contamination at Current and Escape (± Lone Island) may simply be the result of having a larger dataset for these intrusive systems or may reflect the fact that they were emplaced along fault zones where the country rocks were more altered (physically and chemically) and fusible (Fig. 2).

4.4. Cause of Variable Metal Fertility

To date, only the Current and Escape intrusions have been demonstrated to contain economic concentrations of base and precious metals (Ciuculescu et al., 2023). Given that the TBNIC intrusions all crystallized from magmas that originated from the same mantle source, as demonstrated by the similarity in their trace-element geochemistry (Fig. 5), their variable prospectivity is unlikely to be related to processes that occurred in their mantle source. A critical factor in the genesis of magmatic Ni–Cu–PGE sulfide deposits is achieving sulfide saturation, which can be attained via several mechanisms, including addition of SiO_2, Fe_2O_3, and S, and changes in magma oxygen fugacity (fO_2; Jugo, 2009; Ripley and Li, 2013; Cottrell et al., 2021).

Addition of Si and Fe to a magma cause its sulfide solubility to decrease and increase, respectively (Robb, 2004; Ripley and Li, 2013). If the observation that Current and Escape are the only intrusions in the TBNIC that assimilated limited amounts of crustal material is true and not just a function of sample population size, then an increase SiO_2 and/or decrease in Fe_2O_3 via contamination of the Current and Escape magmas, and the lack thereof in the other intrusions, may be the cause of the variable prospectivity, with the barren intrusions (Lone Island, East–West Corridor, 025, and Greenwich) simply not becoming saturated in sulfide liquid. This seems unlikely, however, for two reasons. First, the degree of contamination of the Current and Escape magmas is exceedingly small, typically less than 2% assuming a granitic contaminant (Fig. 8), which would not have added sufficient SiO_2 (~0.4 wt% SiO_2 based on a mafic rock with 51 wt% SiO_2 and a granite with 72 wt% SiO_2) or decreased Fe_2O_3 sufficiently (~0.26 wt% based on a mafic rock with 15 wt% Fe_2O_3 and a granite with 2 wt% Fe_2O_3) to significantly lower the sulfur content at sulfide saturation (Ripley and Li, 2013). Second, the upper gabbros and quartz gabbros contain xenoliths of granite and quartz (Fig. S1), but are barren. Brzozowski et al. (2023a) also demonstrated that, at Current, the dominant source of external S that generated the sulfides in the majority of the intrusion was not the local country rocks, but rather Archean rocks at depth, with the former only contributing sulfur to the magma that crystallized to form the Southeast Anomaly (i.e., the final portion of the intrusion to have crystallized). Given the lack of contribution of the local country rocks to the formation of mineralization at Current, and the overall low degrees of bulk assimilation recorded by Current and Escape, it seems unlikely that contamination by local country rocks was the primary control on the mineralization.

Although a decrease in magma fO_2 can cause it to become saturated in sulfide liquid via the conversion of SO_4^{2+} to S^{2-}, plume-related environments are characterized by fO_2 values of FMQ + 0.1, in which all S is present as S^{2-} (Jugo, 2009; Jugo et al., 2010; Cottrell et al., 2021). Additionally, because the TBNIC intrusions are cogenetic, were emplaced into the same country rocks, and did not assimilate significant amounts of country rock material, variations in fO_2 amongst the intrusions caused by variable assimilation seems unlikely. Similarly, because the intrusions fractionated similar minerals (Fig. 4), variations in fO_2 amongst the intrusions caused by melt differentiation also seems unlikely. Taken together, it is unlikely that changes in S speciation related to redox changes contributed to the variable fertility of the TBNIC intrusions.

Another possibility that may account for the variable fertility throughout the TBNIC is the degree of sulfide segregation, with the barren intrusions having crystallized from magmas that lost sulfide liquid en route to the surface, and the mineralized intrusions having crystallized from magmas that effectively transported sulfide liquid to the site of emplacement. To assess this, we use the Cu, Zr, and Pd contents of peridotites and gabbros from the different intrusions (where data is available) as ratios of these elements (i.e., Cu/Zr, Cu/Pd) serve as robust proxies of sulfide segregation and accumulation given their highly variable sulfide liquid–silicate melt partition coefficients (Barnes et al., 1993; Barnes and Ripley, 2016; Brzozowski et al., 2020). For example, given that sulfide liquid–silicate melt partition coefficients decrease from Pd >> Cu >> Zr, loss of sulfide liquid would generate a residual magma with high Cu/Pd ratios (>10,000; Barnes et al., 1993), low Cu/Zr ratios (<2.86; McDonough and Sun, 1995), and low Pd contents, whereas sulfide accumulation will generate the reverse trends.

Samples from the economically mineralized Current and Escape intrusions are characterized by highly variable Cu/Pd and Cu/Zr ratios, with Cu/Pd ratios ranging from mantle to greater than mantle values of 1000–10,000 (Barnes et al., 1993, 2015) and Cu/Zr ratios ranging from less than to greater than the mantle value of ~2.86 (McDonough and Sun, 1995) (Figs. 9A and 9B). In contrast, samples from the Lone Island, East–West Corridor, 025, and Greenwich intrusions all have high Cu/Pd and low Cu/Zr values (Figs. 9A and 9B). In general, the high Cu/Pd and low Cu/Zr values occur in the gabbros (MgO <15 wt%), whereas the low Cu/Pd and high Cu/Zr values occur in the peridotites (MgO >15 wt%) (Figs. 9A and 9B). The high Cu/Pd and low Cu/Zr values could not have been the result of Cu mobility because this process would have generated vertical trends in Cu/Pd versus Pd space (i.e., significant variability in Cu/Pd, with limited variability in Pd), but this is not observed (Fig. 9C). Hollings et al. (2023) identified melt inclusions in mafic and felsic rocks of the St. Ignace Island Complex on the north shore of Lake Superior with Cu contents of 176 ± 131 ppm (average ± 1σ) and 104 ± 66 ppm, respectively, which are higher than typical mantle-derived melts (<50 ppm; Barnes et al., 2015). If the elevated Cu/Zr and Cu/Pd ratios of the intrusions resulted from their melts being sourced from anomalously Cu-enriched mantle sources, this would have elevated their initial metal ratios, but would have had no affected on the trends in Cu/Zr–Cu/Pd–Pd–MgO space, which are largely controlled by sulfide liquid–silicate melt partitioning and magma fractionation (Fig. 9). This scenario would also not be able to explain the variability in these ratios in cogenetic rocks within a given intrusion (e.g., Current and Escape) (Fig. 9).

The Cu/Pd–Pd diagram is commonly used to assess enrichment of sulfide liquids in metals, and accumulation and segregation of sulfide liquids from silicate magmas (Fig. 9C) (e.g., Barnes et al., 1993; Good et al., 2017). In this diagram, sulfide segregation generates elevated Cu/Pd values, lower Pd contents, and a negative correlation between Cu/Pd–Pd, whereas sulfide enrichment (i.e., R factor or silicate melt/sulfide liquid mass ratio; Campbell and Naldrett, 1979; Mungall et al., 2020) and accumulation generates mantle-like to lower-than-mantle Cu/Pd values and elevated Pd contents (Fig. 9C). These trends are based solely on the difference in magnitude of the sulfide liquid–silicate melt partition coefficients of Cu ($D^{Cu}_{sul-sil} = 2130$) and Pd ($D^{Pd}_{sul-sil} = 536{,}000$) (Barnes and Ripley, 2016) that cause these metals to fractionate during sulfide segregation and enrichment. Data for the Current and Escape intrusions exhibit two distinct trends in Cu/Pd versus Pd space—one that follows the R factor model curves at Cu/Pd <10,000, indicative of sulfide liquid enrichment and accumulation, and another that falls along the sulfide segregation curve at Cu/Pd >10,000, indicative of sulfide removal from the magma (Fig. 9C). Data for Lone Island, East–West Corridor, and 025, however, only exhibit one of these trends, plotting along the sulfide segregation curve, with Lone Island crystallizing from magmas that segregated a smaller proportion of sulfide liquid than the magmas from which the 025 and East–West Corridor crystallized (Fig. 9C). Considering that the Cu and Pd budgets of sulfide-saturated magmas are strongly controlled by the segregation of sulfide liquids, these geochemical characteristics have two implications.

First, given the higher sulfide liquid–silicate melt partition coefficient of Pd relative to Cu, the presence of depleted Cu/Pd values at low Pd contents in all of the intrusions demon-

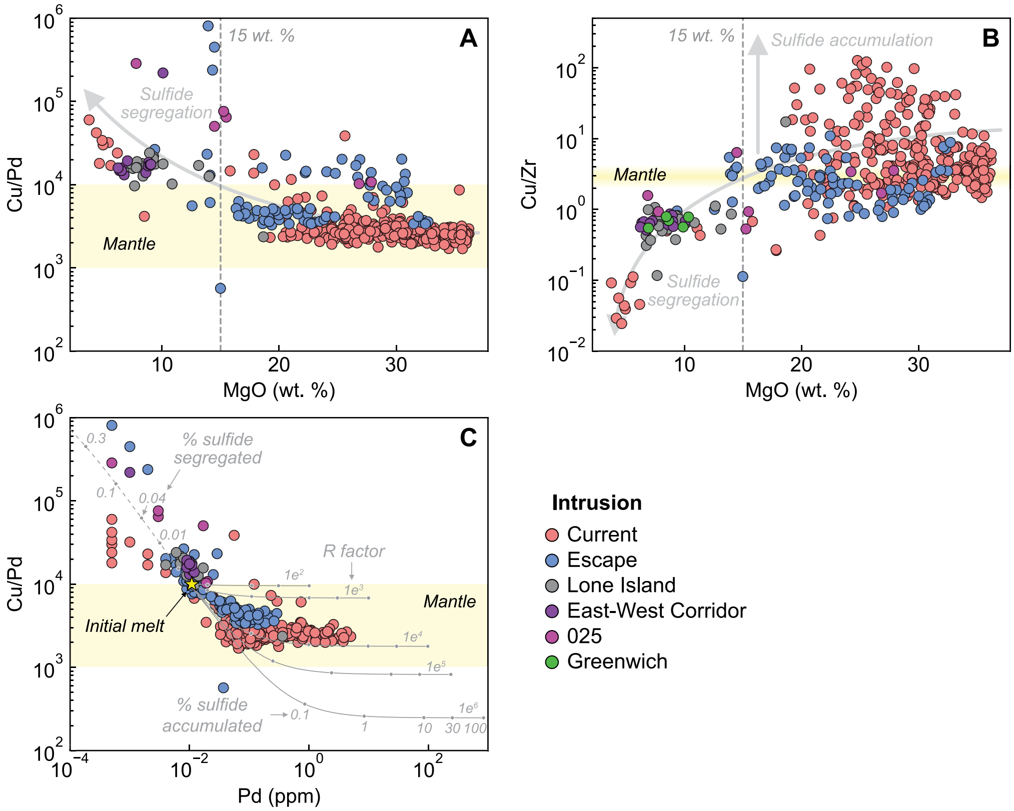

Figure 9. Binary diagrams illustrating the variations in (A) Cu/Pd–MgO, (B) Cu/Zr–MgO, and (C) Cu/Pd–Pd for the mafic–ultramafic rocks of the Thunder Bay North Intrusive Complex, Canada. The R factor and sulfide segregation model curves are based on equations from Campbell and Naldrett (1979) and Barnes et al. (1993), respectively. Initial Cu and Pd contents of the parent magma were set to 100 ppm and 0.01 ppm, respectively, which are similar to the values of the theoretical parental melt to the Current deposit calculated by Heggie (2012) and utilized by Brzozowski et al. (2023a). The same starting values are utilized for all of the intrusions as they are demonstrated to be cogenetic. Although variations in initial Cu and Pd concentrations will shift the model curves, the main purpose of this diagram is to demonstrate that some of the intrusions have elevated Cu/Pd values that are negatively correlated with Pd, a feature diagnostic of sulfide segregation.

strates that they all crystallized from magmas that segregated sulfide liquid at some stage during their magmatic evolution. In the case of the Current intrusion, Brzozowski et al. (2023a) demonstrated that the magmas lost sulfide liquid in the waning stages of magmatic activity when the Southeast Anomaly was crystallizing. The restriction of mantle-like Cu/Pd values and elevated Pd contents to Current and Escape (± Lone Island), however, implies that sulfide accumulation only occurred in these intrusions, at least at the site of emplacement. Second, sulfide accumulation is restricted to the peridotites, whereas gabbros systematically record loss of sulfide liquid. Taken together, this suggests that the apparent infertility of Lone Island, East–West Corridor, 025, and Greenwich may simply be a function of not yet "seeing" the ultramafic cumulates at depth that contain accumulations of sulfide liquid, similar to Current and Escape.

The cause of this variability in sulfide segregation is likely related to the presence of crustal-scale weaknesses, the architecture of the intrusive system, and/or the volatile content of the magmas. Silicate melts (2.7–2.9 g/cm3; Williams et al., 1998) are significantly less dense than sulfide liquids (4–5 g/cm3; Mungall and Su, 2005), hindering the efficiency with which sulfide liquids can be transported upward. This can be mitigated, however, if crustal-scale weaknesses are present that can promote rapid transport of magma through the crust. Both the Current and Escape intrusions occur along the Escape Lake and Quetico faults (Fig. 2), which may have enabled the efficient transport and accumulation of sulfide liquid to the location of emplacement, generating the sulfide enrichment now represented by the Current and Escape deposits. Although the sulfide-poor Greenwich and 025 intrusions do not occur along the Escape Lake and Quetico faults, Lone Island and the East–West Corridor do (Fig. 2), indicating that intrusion along these crustal weaknesses was likely not the defining factor controlling the efficiency of sulfide transport.

The challenge in transporting sulfide liquid vertically can be amplified by variations in the morphology of the conduit systems that fed intrusions. For example, where conduit systems widen and magma flow rate decreases, the capacity of the magma to carry sulfide would also decrease, leading to the settling and accumulation of sulfide liquid under the force of gravity (Evans-Lamswood et al., 2000; Barnes et al., 2016). The morphologies of the Current and Escape intrusions have been well characterized, occurring as shallow-dipping, wide to narrow chonoliths near the present surface (Figs. 2B and 2C) (Brzozowski et al., 2023a; Caglioti, 2023). Although the morphologies of the other intrusions have not been well characterized, it is possible that the shallow-dipping and variably wide nature of the Current and Escape intrusions promoted sulfide accumulation at shallow levels by decreasing magma flow rate, whereas the morphologies of the other intrusions promoted sulfide accumulation at depth. This concept is supported by the fact that, at Current, the morphology of the southern portion of the conduit promoted sulfide loss, potentially by gravity drainage, causing the Southeast Anomaly to be unmineralized relative to the other portions of the conduit where sulfide liquid accumulated (Brzozowski et al., 2023a).

Experimental (Mungall et al., 2015; Iacono-Marziano et al., 2022) and natural observations (Barnes et al., 2019, 2023), as well as theoretical calculations (Yao and Mungall, 2020) have demonstrated that upward transport of sulfide liquid can be assisted by the attachment of vapor bubbles onto sulfide liquid droplets. Formation of these compound droplets is largely restricted to intrusions emplaced at relatively shallow crustal depths and low confining pressures that would permit vapor exsolution (Barnes et al., 2019, 2023). This criteria appears to have been met for the Current deposit as it contains evidence of compound vapor–sulfide droplets (Brzozowski et al., 2023a), indicating that some amount of sulfide liquid was likely transported upward with the assistance of vapor bubbles. Compound vapor–sulfide droplets have not, as of yet, been identified in the other intrusions. Although no definitive statement can be made, it is possible that the variable prospectivity of the TBNIC intrusions is a result of variations in conduit morphology and/or degree of vapor exsolution, which would have controlled the extent to which sulfide liquid was transported to shallow crustal levels and permitted to accumulate in the intrusions.

5. CONCLUSIONS

The Thunder Bay North Intrusive Complex (TBNIC) comprises six mafic–ultramafic intrusions that intruded Archean rocks of the Quetico Subprovince. These intrusions are variably mineralized with Ni, Cu, and PGE, with only the Current and Escape intrusions hosting economic accumulations of sulfide mineralization. Despite the economic importance of the TBNIC, the petrogenetic relationship of the intrusions that comprise the complex and the cause of the apparent variable fertility remains ambiguous. Here, we integrated newly acquired zircon/baddeleyite U–Pb geochronological, bulk-rock geochemical, and bulk-rock Rb–Sr and Sm–Nd isotopic data with previously collected data to assess (1) the age of the TBNIC, (2) the genetic relationships of the different intrusions, (3) the contributions of mantle and crustal sources to the magmatic evolution of the intrusive complex, and (4) the cause of the apparent variable fertility across the intrusive complex.

(1) The intrusions that comprise the TBNIC were emplaced at ca. 1106 Ma (Escape = 1107.6 ± 0.9 Ma; Current = 1106.6 ± 1.6 Ma, Bleeker et al., 2020; Lone Island = 1106.3 ± 2.1 Ma, Metsaranta and Kamo, 2021; Greenwich = 1105.7 ± 0.9 Ma), with the Escape intrusion being the oldest and Greenwich the youngest intrusive phases of the system. This places the TBNIC within the Early Stage of the Midcontinent Rift System (Miller and Nicholson, 2013).

(2) The six intrusions that comprise the TBNIC are genetically related and crystallized from magmas that originated from the same source, with small geochemical variations observed within and among the intrusions being related to fractionation and accumulation of variable amounts of clinopyroxene $\pm$ apatite.

(3) The magmas from which the intrusions crystallized were sourced primarily ($>90\%$) from depleted subcontinental lithospheric mantle beneath the Midcontinent Rift, with the Keweenaw Plume only contributing limited ($<10\%$) material. These melts assimilated limited ($<5\%$) crustal material during transport through the crust, with geochemical evidence of this limited contamination (e.g., elevated Th/La) being restricted to the mafic–ultramafic rocks of the Current, Escape, and Lone Island intrusions.

(4) The apparent variable fertility of the TBNIC intrusions is unrelated to processes that operated in the mantle source that fed the intrusions as their magmas originated from the same source. Rather, it is likely a reflection of the timing and location of sulfide segregation and accumulation, with the barren gabbros of the Lone Island, East–West Corridor, 025, and Greenwich intrusions recording the magmas that lost sulfide liquid during transport to shallow crustal levels. The peridotites of the Current and Escape intrusions, however, record the accumulation of sulfide liquid that was efficiently transported to their location of emplacement.

(5) This work has important implications for exploration for magmatic sulfide deposits in variably mineralized intrusive complexes as it demonstrates that seemingly barren intrusions may host sulfide mineralization at depth, providing a pathway to explore for additional mineralization.

ACKNOWLEDGMENTS

The authors would like to sincerely thank the science editor, Wenjiao Xiao, and the associate editor, Reimar Seltmann, for their efficient handling of the manuscript, and Chris Jenkins and an anonymous reviewer for their thorough and constructive reviews that invariably helped to improve the quality of this manuscript. The authors would also like to thank Clean Air Metals Inc. (Thunder Bay, Canada) for providing access to their geochemical database and their core facility for sampling. The quartz gabbro sample from the Escape intrusion used for U–Pb data was collected by Dustin Liikane. This work was funded by a Natural Sciences and Engineering Research Council of Canada (NSERC) Alliance grant (ALLRP 551989-20) to P. Hollings and includes contributions from the M.S. theses of C. Caglioti, K. Yahia, and A.C. Bravo.

REFERENCES CITED

Barnes, S.-J., and Ripley, E.M., 2016, Highly siderophile and strongly chalcophile elements in magmatic ore deposits: Reviews in Mineralogy and Geochemistry, v. 81, p. 725–774, https://doi.org/10.2138/rmg.2016.81.12.

Barnes, S.-J., Couture, J.-F., Sawyer, E.W., and Bouchaib, C., 1993, Nickel-copper occurrences in the Belleterre-Angliers Belt of the Pontiac Subprovince and the use of Cu-Pd ratios in interpreting platinum-group element distributions: Economic Geology, v. 88, p. 1402–1418, https://doi.org/10.2113/gsecongeo.88.6.1402.

Barnes, S.J., Mungall, J.E., and Maier, W.D., 2015, Platinum group elements in mantle melts and mantle samples: Lithos, v. 232, p. 395–417, https://doi.org/10.1016/j.lithos.2015.07.007.

Barnes, S.J., Cruden, A.R., Arndt, N., and Saumur, B.M., 2016, The mineral system approach applied to magmatic Ni-Cu-PGE sulphide deposits: Ore Geology Reviews, v. 76, p. 296–316, https://doi.org/10.1016/j.oregeorev.2015.06.012.

Barnes, S.J., Le Vaillant, M., Godel, B., and Lesher, C.M., 2019, Droplets and bubbles: Solidification of sulphide-rich vapour-saturated orthocumulates in the Norilsk-Talnakh Ni-Cu-PGE ore-bearing intrusions: Journal of Petrology, v. 60, p. 269–300, https://doi.org/10.1093/petrology/egy114.

Barnes, S.J., Williams, M., Smithies, R.H., Hanski, E., and Lowrey, J.R., 2021, Trace element contents of mantle-derived magmas through time: Journal of Petrology, v. 62, https://doi.org/10.1093/petrology/egab024.

Barnes, S.J., Yudovskaya, M.A., Iacono-Marziano, G., Vaillant, M.L., Schoneveld, L.E., and Cruden, A.R., 2023, Role of volatiles in intrusion emplacement and sulfide deposition in the supergiant Norilsk-Talnakh Ni-Cu-PGE ore deposits: Geology, v. 51, p. 1027–1032, https://doi.org/10.1130/G51359.1.

Bédard, J.H., Leclerc, F., Harris, L.B., and Goulet, N., 2009, Intra-sill magmatic evolution in the Cummings Complex, Abitibi greenstone belt: Tholeiitic to calc-alkaline magmatism recorded in an Archaean subvolcanic conduit system: Lithos, v. 111, p. 47–71, https://doi.org/10.1016/j.lithos.2009.03.013.

Bleeker, W., Smith, J., Hamilton, M., Kamo, S., Liikane, D., Hollings, P., Cundari, R., Easton, M., and Davis, D., 2020, The Midcontinent Rift and its mineral systems: Overview and temporal constraints of Ni-Cu-PGE mineralized intrusions, *in* Bleeker, W., and Houlé, M.G., eds., Targeted Geoscience Initiative 5: Advances in the Understanding of Canadian Ni-Cu-PGE and Cr Ore Systems—Examples from the Midcontinent Rift, the Circum-Superior Belt, the Archean Superior Province, and Cordilleran Alaskan-Type Intrusions: Geological Survey of Canada, Open File 8722, p. 7–35, https://doi.org/10.4095/326880.

Bobrov, A.V., Litvin, Y.A., Kuzyura, A.V., Dymshits, A.M., Jeffries, T., and Bindi, L., 2014, Partitioning of trace elements between Na-bearing majoritic garnet and melt at 8.5 GPa and 1500–1900°C: Lithos, v. 189, p. 159–166, https://doi.org/10.1016/j.lithos.2013.11.003.

Bradfield, A., Barry, J., Brown, F., Burga, D., Feasby, D.G., Kuchling, K., Mackie, B., Pitman, P., and Puritch, E., 2020, Technical report, updated mineral resource estimate and preliminary economic assessment of the Marathon deposit, Thunder Bay mining district, northwestern Ontario, Canada 48°45′ N Latitude, 86°19′ W Longitude: P&E Mining Consultants Inc., NI 43-101 & 43-101F1.

Brzozowski, M.J., Samson, I.M., Gagnon, J.E., Good, D.J., and Linnen, R.L., 2020, On the mechanisms for low-sulfide, high-platinum group element and high-sulfide, low-platinum group element mineralization in the Eastern Gabbro, Coldwell Complex, Canada: Evidence from textural associations, S/Se values, and platinum group element concentrations of base metal sulfides: Economic Geology, v. 115, p. 355–384, https://doi.org/10.5382/econgeo.4708.

Brzozowski, M.J., Good, D.J., Yan, W., Wu, C., An, S., and Li, W., 2022, Mg-Fe isotopes link the geochemical complexity of the Coldwell Complex, Midcontinent Rift to metasomatic processes in the mantle: Journal of Petrology, v. 63, https://doi.org/10.1093/petrology/egac081.

Brzozowski, M.J., Hollings, P., Heggie, G., MacTavish, A., Wilton, D., and Evans-Lamswood, D., 2023a, Characterizing the supra- and subsolidus processes that generated the Current PGE-Cu-Ni deposit, Thunder Bay North Intrusive Complex, Canada: Insights from trace elements and multiple S isotopes of sulfides: Mineralium Deposita, v. 58, p. 1559–1581, https://doi.org/10.1007/s00126-023-01193-9.

Brzozowski, M.J., Hollings, P., Zhu, J.-J., and Creaser, R.A., 2023b, Osmium isotopes record a complex magmatic history during the early stages of formation of the North American Midcontinent Rift: Implications for rift initiation: Lithos, v. 436–437, https://doi.org/10.1016/j.lithos.2022.106966.

Caglioti, C., 2023, PGE-Cu-Ni Sulfide mineralization of the Mesoproterozoic Escape intrusion, northwestern Ontario [M.S. thesis]: Thunder Bay, Canada, Lakehead University, 221 p.

Campbell, I.H., and Naldrett, A.J., 1979, The influence of silicate: Sulfide ratios on the geochemistry of magnetic sulfides: Economic Geology, v. 74, p. 1503–1506, https://doi.org/10.2113/gsecongeo.74.6.1503.

Cannon, W.F., 1992, The Midcontinent rift in the Lake Superior region with emphasis on its geodynamic evolution: Tectonophysics, v. 213, p. 41–48, https://doi.org/10.1016/0040-1951(92)90250-A.

Caro, G., and Bourdon, B., 2010, Non-chondritic Sm/Nd ratio in the terrestrial planets: Consequences for the geochemical evolution of the mantle-crust system: Geochimica et Cosmochimica Acta, v. 74, p. 3333–3349, https://doi.org/10.1016/j.gca.2010.02.025.

Chaffee, M.R., 2015, Petrographic and geochemical study of the hybrid rock unit associated with the Current Lake Intrusive Complex [M.S. thesis]: Minneapolis, USA, University of Minnesota, 139 p.

Ciuculescu, T., Horan, S., and Jones, L., 2023, Technical Report on the Thunder Bay North Project, Ontario, Canada: NI 43-101, 232 p.

Cottrell, E., Birner, S.K., Brounce, M., Davis, F.A., Waters, L.E., and Kelley, K.A., 2021, Oxygen fugacity across tectonic settings, *in* Moretti, R., and Neuville, D.R., eds., Magma Redox Geochemistry: American Geophysical Union Geophysical Monograph Series 266, p. 33–61, https://doi.org/10.1002/9781119473206.ch3.

Cundari, R.M., Puumala, M.A., Smyk, M.C., and Hollings, P., 2021, New and compiled whole-rock geochemical and isotope data of Midcontinent Rift-related rocks, Thunder Bay area: Ontario Geological Survey Miscellaneous Release Data 308.

Davis, D.W., and Green, J.C., 1997, Geochronology of the North American Midcontinent rift in western Lake Superior and implications for its geodynamic evolution: Canadian Journal of Earth Sciences, v. 34, p. 476–488, https://doi.org/10.1139/e17-039.

Dumas, J., and Heggie, G., 2012, 2012 Greenwich Lake Joint Venture Report, Thunder Bay Mining Division, Northwestern Ontario: Ministry of Energy, Northern Development and Mines, 154 p.

Evans-Lamswood, D.M., Butt, D.P., Jackson, R.S., Lee, D.V., Muggridge, M.G., and Wheeler, R.I., 2000, Physical controls associated with the distribution of sulfides in the Voisey's Bay Ni-Cu-Co deposit, Labrador: Economic Geology, v. 95, p. 749–769, https://doi.org/10.2113/gsecongeo.95.4.749.

Ezad, I.S., Blanks, D.E., Foley, S.F., Holwell, D.A., Bennett, J., and Fiorentini, M.L., 2024a, Lithospheric hydrous pyroxenites control localisation and Ni endowment of magmatic sulfide deposits: Mineralium Deposita, v. 59, p. 227–236, https://doi.org/10.1007/s00126-023-01238-z.

Ezad, I.S., Saunders, M., Shcheka, S.S., Fiorentini, M.L., Gorojovsky, L.R., Förster, M.W., and Foley, S.F., 2024b, Incipient carbonate melting drives metal and sulfur mobilization in the mantle: Science Advances, v. 10, no.12, https://doi.org/10.1126/sciadv.adk5979.

Good, D.J., and Lightfoot, P.C., 2019, Significance of the metasomatized lithospheric mantle in the formation of early basalts and Cu-platinum group element sulfide mineralization in the Coldwell Complex, Midcontinent Rift, Canada: Canadian Journal of Earth Sciences, v. 56, p. 693–714, https://doi.org/10.1139/cjes-2018-0042.

Good, D.J., Epstein, R., McLean, K., Linnen, R., and Samson, I., 2015, Evolution of the Main Zone at the Marathon Cu-PGE sulfide deposit, Midcontinent Rift, Canada: Spatial relationships in a magma conduit setting: Economic Geology, v. 110, p. 983–1008, https://doi.org/10.2113/econgeo.110.4.983.

Good, D.J., Cabri, L.J., and Ames, D.E., 2017, PGM Facies variations for Cu-PGE deposits in the Coldwell Alkaline Complex, Ontario, Canada: Ore Geology Reviews, v. 90, p. 748–771, https://doi.org/10.1016/j.oregeorev.2017.04.028.

Good, D.J., Hollings, P., Dunning, G., Epstein, R., McBride, J., Jedemann, A., Magnus, S., Bohay, T., and Shore, G., 2021, A new model for the Coldwell Complex and associated dykes of the Midcontinent Rift, Canada: Journal of Petrology, v. 62, no. 7, https://doi.org/10.1093/petrology/egab036.

Heggie, G., 2010, Interpretation of the LIL and EWC drilling: Part 2. Geochemistry and petrology, Lone Island Lake, and East-West connector projects: Thunder Bay Mining Division, Northwestern Ontario, Canada: Internal report to Magma Metals (Canada) Ltd., p. 1–20.

Heggie, G., 2012, 2012 Drill results and interpretations: Part 2. Lone Island Lake area geochemistry: Internal report to Magma Metals (Canada) Ltd., 9 p.

Heggie, G., Johnson, J., and MacTavish, A., 2015, Thunder Bay North Current Chonolith Field Trip: Panoramic PGM Field Trip, 28 p.

Higuchi, H., and Nagasawa, H., 1969, Partition of trace elements between rock-forming minerals and the host volcanic rocks: Earth and Planetary Science Letters, v. 7, p. 281–287, https://doi.org/10.1016/0012-821X(69)90066-1.

Hollings, P., Hart, T., Richardson, A., and MacDonald, C.A., 2007a, Geochemistry of the Mesoproterozoic intrusive rocks of the Nipigon Embayment, northwestern Ontario: Evaluating the earliest phases of rift development: Canadian Journal of Earth Sciences, v. 44, p. 1087–1110, https://doi.org/10.1139/e06-127.

Hollings, P., Richardson, A., Creaser, R.A., and Franklin, J.M., 2007b, Radiogenic isotope characteristics of the Mesoproterozoic intrusive rocks of the Nipigon Embayment, northwestern Ontario: Canadian Journal of Earth Sciences, v. 44, p. 1111–1129, https://doi.org/10.1139/e06-128.

Hollings, P., Hanley, J., Smyk, M., Heaman, L., Cousens, B., and Zajacz, Z., 2023, The ~1.1 Ga St. Ignace Island Complex, Northern Ontario, Canada: Evidence for magma mixing and crustal melting in the generation of Midcontinent Rift-related bimodal magmas and implications for regional metallogeny: Journal of Petrology, v. 64, no. 6, https://doi.org/10.1093/petrology/egad032.

Hutchinson, D.R., White, R.S., Cannon, W.F., and Schulz, K.J., 1990, Keweenaw hot spot: Geophysical evidence for a 1.1 Ga mantle plume beneath the Midcontinent Rift System: Journal of Geophysical Research: Solid Earth, v. 95, p. 10,869–10,884, https://doi.org/10.1029/JB095iB07p10869.

Iacono-Marziano, G., Le Vaillant, M., Godel, B.M., Barnes, S.J., and Arbaret, L., 2022, The critical role of magma degassing in sulphide melt mobility and metal enrichment: Nature Communications, v. 13, no. 2359, https://doi.org/10.1038/s41467-022-30107-y.

Jaffey, A.H., Flynn, K.F., Glendenin, L.E., Bentley, W.C., and Essling, A.M., 1971, Precision measurement of half-lives and specific activities of U 235 and U 238: Physical Review, v. 4, p. 1889–1906.

Jugo, P.J., 2009, Sulfur content at sulfide saturation in oxidized magmas: Geology, v. 37, p. 415–418, https://doi.org/10.1130/G25527A.1.

Jugo, P.J., Wilke, M., and Botcharnikov, R.E., 2010, Sulfur K-edge XANES analysis of natural and synthetic basaltic glasses: Implications for S speciation and S content as function of oxygen fugacity: Geochimica et Cosmochimica Acta, v. 74, p. 5926–5938, https://doi.org/10.1016/j.gca.2010.07.022.

Keays, R.R., and Lightfoot, P.C., 2015, Geochemical stratigraphy of the Keweenawan Midcontinent Rift volcanic rocks with regional implications for the genesis of associated Ni, Cu, Co, and platinum group element sulfide mineralization: Economic Geology, v. 110, p. 1235–1267, https://doi.org/10.2113/econgeo.110.5.1235.

Klewin, K.W., and Shirey, S.B., 1992, The igneous petrology and magmatic evolution of the Midcontinent rift system: Tectonophysics, v. 213, p. 33–40, https://doi.org/10.1016/0040-1951(92)90249-6.

Legros, H., Czas, J., Luo, Y., Woodland, S., Sarkar, C., Shirey, S.B., Schulze, D., and Pearson, D.G., 2024, Post-Archean Nb-REE-U enrichment in the Superior craton recorded in metasomatised mantle rocks erupted in the 1.1 Ga Midcontinental Rift event: Mineralium Deposita, v. 59, p. 373–396, https://doi.org/10.1007/s00126-023-01214-7.

Lightfoot, P.C., Hawkesworth, C.J., Hergt, J., Naldrett, A.J., Gorbachev, N.S., Fedorenko, V.A., and Doherty, W., 1993, Remobilisation of the continental lithosphere by a mantle plume: Major-, trace-element, and Sr-, Nd-, and Pb-isotope evidence from picritic and tholeiitic lavas of the Noril'sk District, Siberian Trap, Russia: Contributions to Mineralogy and Petrology, v. 114, p. 171–188, https://doi.org/10.1007/BF00307754.

Maier, W.D., and Groves, D.I., 2011, Temporal and spatial controls on the formation of magmatic PGE and Ni-Cu deposits: Mineralium Deposita, v. 46, p. 841–857, https://doi.org/10.1007/s00126-011-0339-6.

McDonough, W.F., 1990, Constraints on the composition of the continental lithospheric mantle: Earth and Planetary Science Letters, v. 101, p. 1–18, https://doi.org/10.1016/0012-821X(90)90119-I.

McDonough, W.F., and Sun, S.-s., 1995, The composition of the Earth: Chemical Geology, v. 120, p. 223–253, https://doi.org/10.1016/0009-2541(94)00140-4.

Metsaranta, R.T., and Kamo, S.L., 2021, Project NW-19-001: A uranium-lead baddeleyite age for the Midcontinent Rift-related Lone Island Lake intrusion, Northwestern Ontario, *in* Easton, R.M., Préfontaine, S., Hamilton, S.M., Burnham, O.M., Duguet, M., Burt, A.K., and Priebe, E.H., eds., Summary of Field Work and Other Activities, 2021: Ontario Geological Survey, Open File Report 6380, p. 12-1–12-8.

Miller, J.D., and Nicholson, S.W., 2013, Geology and mineral deposits of the 1.1 Ga Midcontinent Rift in the Lake Superior region: An overview, *in* Miller, J.D., ed., Field Guide to Copper-Nickel-Platinum Group Element Deposits of the Lake Superior Region: Precambrian Research Center Guidebook 13-1, p. 1–49.

Mungall, J., and Su, S., 2005, Interfacial tension between magmatic sulfide and silicate liquids: Constraints on kinetics of sulfide liquation and sulfide migration through silicate rocks: Earth and Planetary Science Letters, v. 234, p. 135–149, https://doi.org/10.1016/j.epsl.2005.02.035.

Mungall, J.E., Brenan, J.M., Godel, B., Barnes, S.J., and Gaillard, F., 2015, Transport of metals and sulphur in magmas by flotation of sulphide melt on vapour bubbles: Nature Geoscience, v. 8, p. 216–219, https://doi.org/10.1038/ngeo2373.

Mungall, J.E., Christopher Jenkins, M., Robb, S.J., Yao, Z., and Brenan, J.M., 2020, Upgrading of magmatic sulfides, revisited: Economic Geology, v. 115, p. 1827–1833, https://doi.org/10.5382/econgeo.4775.

Nicholson, S.W., and Shirey, S.B., 1990, Midcontinent rift volcanism in the Lake Superior Region: Sr, Nd, and Pb isotopic evidence for a mantle plume origin: Journal of Geophysical Research: Solid Earth, v. 95, p. 10,851–10,868, https://doi.org/10.1029/JB095iB07p10851.

Nicholson, S.W., Schulz, K.J., Shirey, S.B., and Green, J.C., 1997, Rift-wide correlation of 1.1 Ga Midcontinent rift system basalts: Implications for multiple mantle sources during rift development: Canadian Journal of Earth Sciences, v. 34, p. 504–520, https://doi.org/10.1139/e17-041.

O'Neill, H.St.C., 2016, The Smoothness and shapes of chondrite-normalized rare earth element patterns in basalts: Journal of Petrology, v. 57, p. 1463–1508, https://doi.org/10.1093/petrology/egw047.

Richardson, S.H., and Shirey, S.B., 2008, Continental mantle signature of Bushveld magmas and coeval diamonds: Nature, v. 453, p. 910–913, https://doi.org/10.1038/nature07073.

Ripley, E.M., and Li, C., 2013, Sulfide saturation in mafic magmas: Is external sulfur required for magmatic Ni-Cu-(PGE) ore genesis?: Economic Geology, v. 108, p. 45–58, https://doi.org/10.2113/econgeo.108.1.45.

Robb, L., 2004, Introduction to Ore-Forming Processes: Wiley-Blackwell, 382 p.

Rooney, T.O., Konter, J.G., Finlayson, V.A., LaVigne, A., Brown, E.L., Stein, C.A., Stein, S., and Moucha, R., 2022, Constraining the isotopic endmembers contributing to 1.1 Ga Keweenawan large igneous province magmatism: Contributions to Mineralogy and Petrology, v. 177, no. 49, https://doi.org/10.1007/s00410-022-01907-8.

Rudnick, R.L., and Gao, S., 2003, Composition of the continental crust, *in* Holland, H.D., and Turekian, K.K., eds., The Crust: Treatise on Geochemistry: Amsterdam, Elsevier, v. 3, p. 1–64, https://doi.org/10.1016/B0-08-043751-6/03016-4.

Shirey, S.B., 1997, Re-Os isotopic compositions of Midcontinent rift system picrites: Implications for plume-lithosphere interaction and enriched mantle sources: Canadian Journal of Earth Sciences, v. 34, p. 489–503, https://doi.org/10.1139/e17-040.

Shirey, S.B., Klewin, K.W., Berg, J.H., and Carlson, R.W., 1994, Temporal changes in the sources of flood basalts: Isotopic and trace element evidence from the 1100 Ma old Keweenawan Mamainse Point Formation, Ontario, Canada: Geochimica et Cosmochimica Acta, v. 58, p. 4475–4490, https://doi.org/10.1016/0016-7037(94)90349-2.

Sun, S.-s., and McDonough, W.F., 1989, Chemical and isotopic systematics of oceanic basalts: Implications for mantle composition and processes, *in* Saunders, A.D., and Norry, M.J., eds., Magmatism in the Ocean Basins: Geological Society, London, Special Publication 42, p. 313–345, https://doi.org/10.1144/GSL.SP.1989.042.01.19.

Thomas, D.G., Melnyk, J., Gormely, L., Searston, S., and Kulla, G., 2011, Technical report on preliminary assessment of the Thunder Bay North Polymetallic Project, Ontario, Canada: Magma Metals Limited Thunder Bay North Polymetallic Project Ontario, Canada, NI 43-101.

Williams, D.A., Kerr, R.C., and Lesher, C.M., 1998, Emplacement and erosion by Archean komatiite lava flows at Kambalda: Revisited: Journal of Geophysical Research: Solid Earth, v. 103, p. 27,533–27,549, https://doi.org/10.1029/97JB03538.

Woodruff, L.G., Schulz, K.J., Nicholson, S.W., and Dicken, C.L., 2020, Mineral deposits of the Mesoproterozoic Midcontinent Rift system in the Lake Superior region: A space and time classification: Ore Geology Reviews, v. 126, https://doi.org/10.1016/j.oregeorev.2020.103716.

Yahia, K., 2024, Geochemistry, petrography, geochronology, and radiogenic isotopes of the weakly mineralized intrusions in Thunder Bay North Igneous Complex [M.S. thesis]: Thunder Bay, Canada, Lakehead University, 140 p.

Yao, Z., and Mungall, J.E., 2020, Flotation mechanism of sulphide melt on vapour bubbles in partially molten magmatic systems: Earth and Planetary Science Letters, v. 542, https://doi.org/10.1016/j.epsl.2020.116298.

Zhang, M., O'Reilly, S.Y., Wang, K.-L., Hronsky, J., and Griffin, W.L., 2008, Flood basalts and metallogeny: The lithospheric mantle connection: Earth-Science Reviews, v. 86, p. 145–174, https://doi.org/10.1016/j.earscirev.2007.08.007.

Zhao, Y., Liu, S., Xue, C., Brzozowski, M.J., and Chen, J., 2024, Metasomatized mantle facilitates the genesis of magmatic nickel-copper sulfide deposits in orogenic belts: A copper isotope perspective: Geochimica et Cosmochimica Acta, v. 366, p. 128–140, https://doi.org/10.1016/j.gca.2023.11.028.

Science Editor: Wenjiao Xiao
Associate Editor: Reimar Seltmann

Manuscript Received 19 April 2024
Revised Manuscript Received 30 August 2024
Manuscript Accepted 3 October 2024